The Paton Welding Journal

11
2024

CONTENTS

ORIGINAL ARTICLES

INFORMATION

MECHANICAL AND THERMAL BEHAVIOR OF ADDITIVELY MANUFACTURED Invar 36 USING A LASER HOT WIRE HYBRID DED PROCESS

Bharat Yelamanchi[1], **Andrew Prokop**[1], **Coleman Buchanan**[1], **Aayush Alok**[1], **Mario Rodriguez**[2], **Jimena Morales**[2], **Holly Martin**[1], **Brian Vuksanovich**[1], **Virgil Solomon**[1], **Eric MacDonald**[2], **Yousub Lee**[3], **Thomas Feldhausen**[2,4], **Pedro Cortes**[2]

[1]Youngstown State University, OH USA 44555
[2]College of Engineering, The University of Texas at El Paso, TX USA 79968
[3]Computational Sciences & Engineering Division, Oak Ridge National Laboratory, TN, USA
[4]Manufacturing Science Division, Oak Ridge National Laboratory, TN, USA

ABSTRACT

Invar 36 alloy is a material of high interest in the composite tooling sector due to its low coefficient of thermal expansion. Current production of Invar 36 tooling using traditional manufacturing such as casting and forging is associated with long lead times due to a multitude of factors such as labor and component shortages, high material costs, foreign competition, and supply chain issues. An attractive alternate process is the use of an integrated 5-axis CNC hybrid Laser Hot Wire Deposition System (LHWD) for manufacturing invar molds. The hybrid process provides a combination of the additive and subtractive technologies resulting in a synergistic platform for producing and repairing structures and molds. The main novelty and goal of this work is to study the properties of Invar deposited by a LHWD and to provide guidelines for the manufacture of parts using this process. In this study, the thermal expansion behavior of the manufactured specimens has been analyzed and related to its printing parameters and direction. Multiple specimens were extracted for mechanical, dilatometry and metallographic testing. A thermal IR recording of the printing process was also carried out to observe the thermal history of the produced parts to establish thermal influence on performance-property-processing relationship. The results of these tests show the advantage of LHWD technology for the manufacture of Invar alloy parts, as it presents similar thermal expansion behavior as those commercially available with minimal presence of precipitates and no macrostructural failures such as pores, cracks and lacks of fusion.

KEYWORDS: hybrid directed energy deposition, Invar, hybrid manufacturing, additive manufacturing, subtractive manufacturing, wire and laser additive manufacturing (WLAM), directed energy deposition (DED), laser hot-wire deposition (LHWD)

INTRODUCTION

Invar alloys, since their discovery have been a widely used material in precision measurement applications and other applications such as pendulums for clocks and thermostats because of their unusual physical behavior of no thermal expansion with temperature change. This phenomenon has been observed in Fe–Ni alloys with Ni concentrations within a range of 30–45 % [1]. Nowadays, the applications of Invar alloys are very diverse including satellite, metrology, LNG carrier, precision instruments, dies, TV kinescopes, liquid natural gas and cryogenic tanks, as well as orbiting satellites, and aerospace tooling [2–6]. Invar stands out because of its low Coefficient of Thermal Expansion (CTE), or its lack of expansion or contraction with changes in temperature [7, 8]. The material of choice in this study, Invar 36, is within this range with a composition in weight of 64 % Fe and 36 % Ni, and a CTE value below $2 \cdot 10^{-6}$ K^{-1} at room temperature [9].

With Fe having a BCC structure, Fe–Ni alloy combined with a concentration higher than 30 % of Ni with FCC structure, the alloy tends to be weldable with an austenitic FCC structure, where Ni is the γ stabilizer of iron.

The Curie temperature (T_c) of wrought Invar 36 is 279 °C and so it shows a very low CTE and ferromagnetic properties below this temperature [10]. Above T_c, the material is paramagnetic with the thermal expansion behavior similar to other metals such as Fe. T_c peaks at a Ni concentration of approximately 66 % and decreases when the Ni concentration drops lower than 40 % due to a reduction in permeability [11]. On the other hand, Invar with its austenitic structure is also hard to machine because of its high ductility, work hardening and low conductivity [12, 13]. Nevertheless, they are adequate for welding [14, 15]. Therefore, hybrid manufacturing, a combination of additive and subtractive processes within the same machine is a good alternative to traditional techniques for the manufacturing of Invar parts, because these technologies are able to manufacture near net shape geometry without large amounts of machining needed.

In the previous works, mostly Laser Powder Bed Fusion (LPBF) technique was employed to exhaustively analyze the evaluation of the CTE value and Curie temperature in materials processed by additive techniques [16–20]. Asgari et al [21] in their study manufactured Invar samples with Fe–Ni (36 %) with SLM technology utilizing different process parameters with significance to laser power. After performing X-ray computed

tomography (CT) to look at the microstructure, density, structural integrity (determining pore size, morphology and inter-alignment of pores), chemical composition and thermal expansion behavior of the manufactured samples, it was concluded that sample densities were higher than 99.8 % in all cases, and the porosity level decreased at higher laser powers.

Yakout et al. [22] reported that the CTE value is related to the volumetric energy density of SLM technology. In the SLM process, the volumetric energy density (J/mm^3) is calculated as the ratio between laser power (W) and the multiplication between the average scanning speed (mm/s), hatch spacing (mm) and layer thickness (mm). It was found that there is a critical laser energy density (identified as 86.8 J/mm^3), for which the SLM process is optimal in terms of material properties. This critical energy density achieves stable melting with a homogeneous composition and microstructure, magnetic properties and similar CTE to those obtained in the commercially available material.

Below the critical energy, the manufactured samples exhibited no significant changes in composition, although voids (gas pores or lack of fusion) formed, and the CTE decreased. In contrast, above this critical energy, the number of voids decreased, but the composition of the samples changed: nickel and manganese levels decreased, while iron, molybdenum, and silicon levels increased. This rise in silicon and molybdenum resulted in a further reduction in CTE and an increase in the magnetic moment of the part [23]. Wegener et al [9] manufactured samples using the SLM process with CTE values of $1.8 \cdot 10^{-6}$ K^{-1} between 0 and 100 °C that were similar to the values of conventionally processed materials. Moreover, adjusting the processing parameters of the LMD process, which employs a 4 kW CO_2 laser and a four-tip coaxial nozzle, resulted in CTE values comparable to those obtained with conventional processing methods [24]. Huang et al [16] fabricated test specimens in multiple orientations and observed that there is significant anisotropy in the microstructure of Invar 36 and hence the mechanical properties. In the same study, they observed that the CTE of Invar 36 alloy in 0°, 45°, and 90° orientation at 30 ~ 200 °C are $1.78 \cdot 10^{-6}$ $°C^{-1}$, $1.62 \cdot 10^{-6}$ $°C^{-1}$ and $1.77 \cdot 10^{-6}$ $°C^{-1}$, respectively, meeting ASTM F1686 standards. Huang et al [25] in another study on additive manufacturing of Invar alloy have identified that even though acceptable mechanical properties and CTE were achieved using the LPBF technology, further optimization is required to understand and resolve the anisotropy based on build orientation. Finally, as was mentioned above, in the previous literature, even though many studies were conducted on additive manufacturing Invar36 alloy using LPBF, few studies have been carried out analyzing the microstructures and the mechanical properties of Invar parts manufactured using WAAM technology and, therefore there is a lack of study on its resulting mechanical and thermal properties.

In this paper, mechanical and thermal expansion properties displayed by Invar specimens manufactured using the LHWD system were analyzed and compared with commercially available Invar 36. This study was implemented with the aim of validating the LHWD technology as a reliable method for manufacturing Invar 36 parts for tooling applications in the aerospace and automotive sectors.

EXPERIMENTAL METHODS AND METHODOLOGY

Fabrication of the test specimen was performed using a Mazak VC500A/5X AM hot wire deposition (HWD) system. A bead analysis was conducted in order to establish a baseline process parameter set for printing the parts. Two different bulk geometries, cube and cuboid were printed using the laser hot wire deposition system in the Bidirectional 0° (Bi0), Bidirectional rotation positive 45° (BRP45) and Bidirectional rotation positive 90° (BRP90) orientation as shown in Figure 1. Following the printing process, the bulk geometries were machined to a net shape in *X* and *Y* dimensions of the tensile, CTE, and hardness samples as shown in Figure 2.

These were then detached from the base and cut to the required *XYZ* dimensions using a wire Electrical Discharge Machining (EDM). Samples were taken from the top, middle and bottom zones of the multilayered print also shown in Figure 1, *a* 1.14 mm (0.045″) diameter Invar 36 wire from Arcos Industries, LLC, was used to fabricate the component. Argon was used as a local shielding gas with a volumetric flow rate of 30 L per minute. The produced dog-bone tensile samples conform to the ASTM E8/E8M-16a standard for tension testing of metallic materials. The cylindrical hardness samples conform to ASTM E18-15 standard for performing rockwell hardness testing. CTE samples conform to ASTM E831-19. A control was also tested with the aforementioned tests on the stock materials ordered from Mcmaster Carr.

This study employed two machining sequences. The first sequence involved a subtractive process that utilized the hybrid manufacturing capabilities of the unit to machine the rough edges created by excess deposition during the printing stage. Here, the subtracting process was performed on the samples once they have reached room temperature. The second sequence consisted of using an EDM to cut the parts off the build platform and to the final dimensions in line with the ASTM's corresponding to the respective test methods. Because of the smaller sizes of the final parts compared to what can be achieved with the mounted tools on the Hybrid system, the EDM method was employed to have better control on the subtractive process. Hyper-
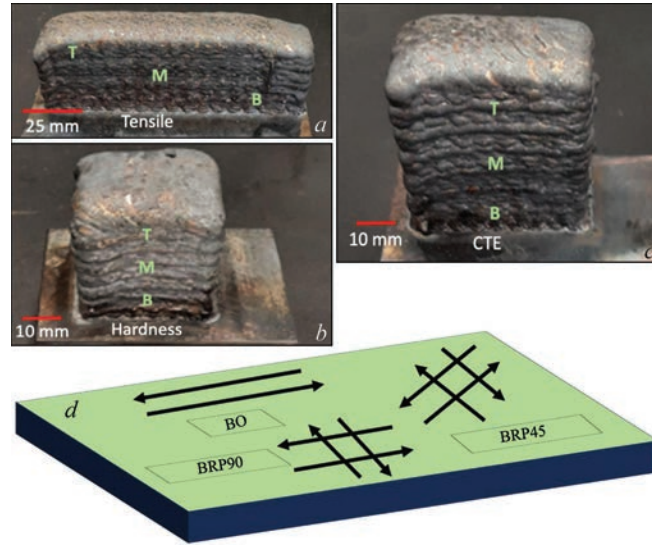
Figure 1. Bulk specimens as printed: *a* — tensile; *b* — hardness; *c* — CTE, and *d* — schematic of the B0, BRP45 and BRP90 print orientations of the manufactured bulk specimens. Positive rotation indicates a clockwise direction

Mill, a computer aided manufacturing (CAM) software from Open mind technologies was used to program the toolpath trajectory for the deposition and first machining sequence. This program accepts the nominal CAD geometry and creates g-code for the developed toolpath trajectories. Builds with three different orientations namely unidirectional, bidirectional, and 90° angle were fabricated and tested in this study.

MECHANICAL AND DILATOMETRY TESTING

To identify the mechanical performance of the parts printed using the VC500A/5X, tensile and hardness tests were conducted. The tensile tests were performed on an Instron in compliance with ASTM E8 subsize specimen. A 150 kN load cell was used to gather the load information and an extensometer was used to gather reliable strain information. Ultimate tensile strength, young's modulus and strain at failure were calculated from the load-extension and strain data obtained from the testing. The Rockwell hardness tests were conducted using a type B spherical indenter in compliance with ASTM E18. The CTE tests were conducted on TA Instruments (Delaware) TMA-Q400 based on ASTM E831-19. In this test, the linear deflection of the sample was measured, and the CTE (10^{-6} um/m·°C^{-1}) was calculated following Eq. (1):

$$CTE = \alpha = \Delta L / \left(L_0 \Delta T \right), \tag{1}$$

where ΔL is the linear deflection; L_0 is the initial length of the samples and ΔT the temperature difference for which ΔL is measured.

MICROSTRUCTURE ANALYSIS

As-printed samples have been prepared for microstructural, chemical, and crystallographic investigations using metallographic techniques. The crystallographic investigations were performed by X-ray diffraction (XRD) using a Rigaku Miniflex II XRD equipped with a Cu X-ray source. The microstructural investigations were performed using light and electron microscopy techniques. The Optical microscopy investigation was carried out using a Keyence VHX-7000 Digital Microscope. The electron microscopy investigations were performed using a JEOL JSM-7600F scanning electron microscope (SEM) equipped with an EDAX Apollo XV X-ray energy dispersive spectrometer (EDS) for chemical analysis.

Figure 2. Machined part geometries for: *a* — hardness; *b* — tensile, and *c* — CTE tests
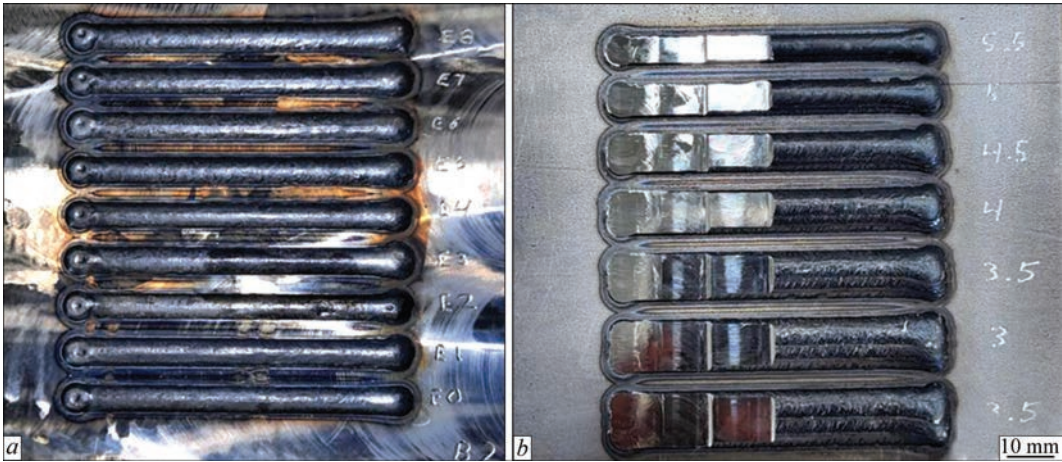
Figure 3. Beads deposited with the process parameter sets E0–E8 (*a*) and overstep analysis (*b*)

THERMAL ANALYSIS

Thermal imaging was employed to monitor the process dynamics of the Laser Hot Wire Deposition of the Invar 36 samples. A FLIR A655sc LWIR camera with f/1.0 and a field of view of 15°×11° (19° diagonal) capable of detecting and converting the emitted InfraRed radiation to temperatures range of –15 to 2000 °C was used. Images were acquired at a resolution of 640×480 pixels at 6 fps. The raw 32-bit data was converted to 16-bit arrays for computational efficiency. Custom Python scripts were developed utilizing the FLIR SDK library for image analysis and video processing. This enabled specialized cropping and data extraction. To extract temperature data, a 10×10-pixel averaging approach was applied to calculate mean temperatures at different heights (lower, middle, upper) of the build. This method was selected since it provides representative data from the desired layer within the printed part.

Table 1. Build process parameter development

Parameter set	Feed rate during deposition, mm/min	Laser power, W	Shielding gas, L/min	Wire feed speed, mm/min	Hot wire power, W
E0 (control)	792	3510	10	4191	480
E1	500	3510	10	4191	480
E2	1200	3510	10	4191	480
E3	792	4000	10	4191	480
E4	792	3200	10	4191	480
E5	792	3510	10	5207	480
E6	792	3510	10	3175	480
E7	792	3510	10	4191	600
E8	792	3510	10	4191	360
Final printing	792	3510	30	4191	600

RESULTS AND DISCUSSION

PRINTING PARAMETER DEVELOPMENT

A comprehensive bead analysis was initially carried out in the 0° orientation before fabricating the parts to understand the influence of process parameters and printing direction on the quality. It was observed that five process parameters dictate the printability. These being the traverse feed rate during deposition, laser power, shielding gas, wire feed speed and hot wire power. In addition to these parameters, there were two toolpath parameters namely Step over and Layer height, specified in Hypermill software, that define the quality of the build when combined with the other five aforementioned process parameters. With a target bead height of around 2.1 mm, and a bead width of 6.5 mm, a total of eight different process parameter sets were investigated in the bead analysis to define the printability based on the initial feedback from the manufacturer of the machine. These parameters are as shown in Table 1.

The beads deposited using the printing parameter sets mentioned in Table 1 are as shown in Figure 3, *a*. It was observed that all parameter sets resulted in a weld bead with consistent thickness, width and height except for E2. Signs of starvation were observed in the weld bead deposited with the parameter set E2. This is because the feed rate of deposition, which is the rate at which the printing head moves, is increased to 1200 from 500 mm/min without making any changes in the wire feed speed.

Upon closer observation of the other beads, it was observed that the parameter set E0 produced a good quality bead with the required height but not the width. E1 resulted in a bead that is too tall because of slowing down the Feed rate of deposition from 792 to 500 mm/min while the wire is being fed to the system at 4191 mm/min. E3, E5, E6 and E8 resulted in flatter and wider beads due to the higher laser power which results in the larger heat affected zone of the substrate, higher wire feed speed which results in expansion of the weld pool region and insufficient preheating of the

wire which would result in a condition similar to starvation if a proper wire feed rate is not maintained. The dimensions of the individual beads are as specified in Table 2. E4 and E7 resulted in the beads closest to the requirement. A quick overlap analysis was also conducted as shown in Figure 3, *b* in order to obtain the ideal stepover during deposition which will preserve the required build conditions. Upon dimension analysis, a stepover of 2.5 mm was decided to be ideal as it produces a layer height of 2.1 mm during print with the final printing parameter set mentioned in Table 1. All the other overlap conditions resulted in taller beads which would result in taller layer height.

THERMAL ANALYSIS

The heat input and the temperature gradients during the deposition and the waiting time of a single bead manufactured using LHWD observed using a IR camera can be observed in Figure 4. Top, middle, and bottom zones were selected for the IR analysis in order to obtain a complete understanding of the thermal history involved in the manufacturing of the part. The heat input is a critical condition that affects the CTE of the material.

By capturing and graphing the temperature profiles of the three layers, a general trend in thermal histories related to the build height was identified. The bottom section, connected to a large thermally conductive build plate, released heat rapidly, resulting in minimal heat accumulation. Figure 4 displays the cooling process on the initial layers, where the temperature drop can be observed. This process can lead to relatively small crystal grains, resulting in enhanced mechanical performance. As additional layers are added, heat is conducted downward through the structure to the build plate. Consequently, the bottom layer (layer 2) is subjected to prolonged exposure to high temperatures, although these temperatures are lower than those experienced by the upper layers (layers 7 and 12). In contrast, the top section of the part (layer12) is subjected to high melting temperatures (above 1000 °C in average as seen in Figure 4) as heat accumulates with

Table 2. Bead analysis parameters and their corresponding bead dimensions

Parameter set	Bead width, mm	Bead height, mm
E0	6.21 ± 0.40	1.54 ± 0.30
E1	6.53 ± 0.40	2.24 ± 0.20
E2	6.26 ± 0.80	1.04 ± 0.19
E3	6.75 ± 1.10	1.27 ± 0.01
E4	6.32 ± 0.60	1.49 ± 0.07
E5	6.66 ± 0.60	1.03 ± 0.14
E6	6.56 ± 0.50	1.22 ± 0.11
E7	6.66 ± 1.00	1.45 ± 0.14
E8	6.66 ± 0.60	1.38 ± 0.08

a longer resistive path to the build plate trajectory. The effects of these two distinct thermal history extremes — (*a*) prolonged low temperature duration and high thermal gradients from the cooling of the build plate, and (*b*) brief high temperature duration with lower thermal gradients — significantly influence both the microstructure and strength of the fabricated part.

CTE

Invar 36 samples obtained by EDM of cuboids manufactured using the LHWD were subjected to a CTE test. A total of 7 groups of coupons, these being a baseline (which was obtained from commercially available invar rod) and B0, BRP45, and BRP90 specimens in both the *XY* and *Z* orientations were subjected to a dilatometry analytical test. From these coupons, three samples were evaluated from both the vertical and horizontal direction. Additionally, three samples from the commercially stock material were EDM and tested as the baseline.

Figure 5 shows the averaged CTE of the test specimens. The figure displays that the printed samples have a similar CTE (1.5 to 3 um/m·°C range), and does not seem to depend on the printing orientation. In this work, CTE shows minor changes regardless of tool path orientations. Similar observations were made in LPBF printing in which the CTE is isotropic in 0, 45, and 90 build orientations [16]. The analysis
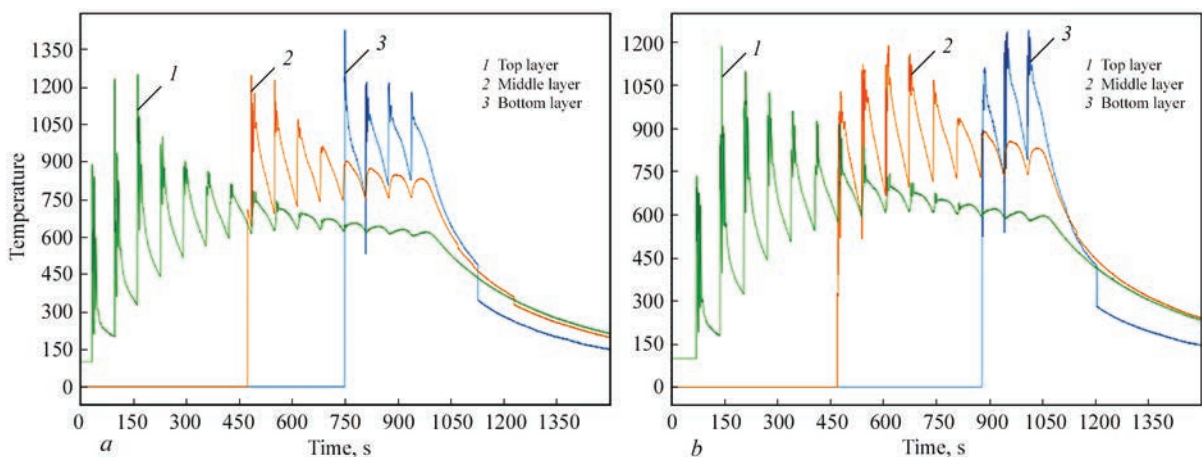
Figure 4. Temperature-time plot to identify the thermal behavior during the deposition and cool down of cuboids printed in *XY* (*a*), and *Z* orientations (*b*)
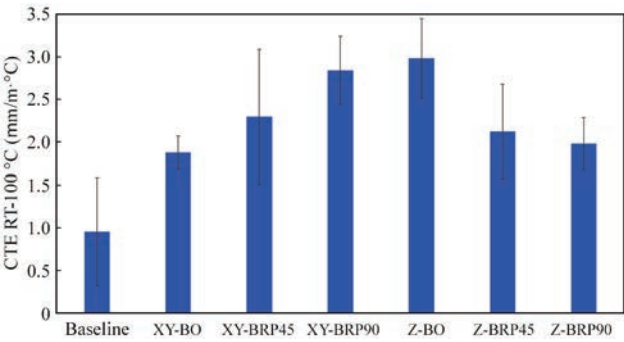
Figure 5. Average CTE results (0–100 °C) of the baseline and manufactured parts in *XY* and *Z* with B0, BRP45, and BRP90 orientations

Figure 6. Tensile performance of the baseline and manufactured test specimen printed in *XY* and *Z* direction based on the B0, BRP45 and BRP90 orientations

of nickel on the printed samples at different locations is shown in Table 1. From the table, it is observed that the printed samples have a similar nickel content (about 35–36 %), a feature that governs their CTE. Additionally, the Curie temperature (T_c) values were also calculated from the results of the dilatometry test. It was here observed that the average T_c of the baseline samples was 280 ± 5 °C while the average T_c of the printed samples in the *XY* and *Z* orientation resulted in 236.67 ± 18.86 and 225 ± 20.41 °C, respectively. This indicates that the printed samples will exhibit higher CTE values at elevated temperatures, since they will reach out the curie temperature sooner. This performance can be associated with Figure 5, where the CTE of the baseline sample is lower compared to

the printed samples. Since the acceptable CTE range for practical applications using wrought Invar 36 is below 2·10⁻⁶ °C [26], from Figure 5 we can conclude that XY-B0, Z-BRP45, and Z-BRP90 are reasonable choices in terms of CTE.

MECHANICAL PROPERTIES

Tensile tests were conducted on specimens obtained from two orientations i.e. *XY* and *Z*, and from three different locations; top, middle, and bottom (for the *XY* printing) and front, middle, and back (for the *Z* printing) as shown in Figure 6. These samples were taken from multi-layered build structures manufactured in B0, BRP45, and BRP90 directions for both orientations. The average UTS, YS, and % elongation of the Baseline and all printed samples are summarized in Table 3.

From Table 3, it is observed that the specimens built in the *Z* orientation have both lower UTS and YS values than those built in the *XY* orientation (by roughly 10 and 5 % respectively) but have similar elongation between the two printing orientations. Here, the averaged tensile strength of the *Z* and *XY* builds yielded a value of about 370 and 383 MPa, respectively. This difference could be associated with the anisotropic property-performance typically observed when printing on the Z-direction [27–31]. In the *XY* orientation builds, it is observed that the bottom samples showed a slightly superior strength than the samples from the middle and top. A mechanism associated with the smaller grain structure due to the thermal sink provided by the building plate. In contrast, the samples from the Z-build does not seem to show a clear trend. Table 3 shows that both printed builds resulted in inferior mechanical properties than the wrought Invar 36 material, similar to what other researchers have observed [32]. Fracture analysis was conducted on the surfaces of the tested tensile specimens using SEM, EDS, and digital microscopy. All the specimens in both orientations and all directional

Table 3. Summarized mechanical properties of baseline and 3D printed Invar 36 specimens

Sample name	Location	Averaged values		
		UTS, MPa	Yield strength, MPa	Elongation, %
Baseline	–	441.57	263.43	48.15
XY-B0	Top	374.49	209.19	30.92
	Middle	368.73	184.79	37.22
	Bottom	397.45	206.84	36.03
XY-BRP45	Top	361.25	175.36	45.77
	Middle	384.70	190.99	41.21
	Bottom	408.23	204.93	42.20
XY-BRP90	Top	380.55	191.71	42.78
	Middle	381.33	218.15	37.27
	Bottom	387.77	205.65	40.30
Z-B0	Front	357.83	175.99	43.38
	Middle	365.34	185.00	42.46
	Back	367.16	196.46	40.78
Z-BRP45	Front	390.52	194.70	36.78
	Middle	359.56	185.42	39.74
	Back	378.00	196.37	37.25
Z-BRP90	Front	370.59	187.76	35.59
	Middle	357.47	182.97	40.68
	Back	382.25	191.78	38.49

Figure 7. Fracture surface of the tested tensile specimen: *a* — Z-BRP45; *b* — XY-BRP90 displaying a ductile fracture profile

builds displayed a ductile fracture. The typical failure mechanism is evident in Figure 7 where the fracture surface(s) show necking back to the unaffected surfaces due to the elongation of the sample. The hardness tests were conducted on tensile samples and the results are summarized in Figure 8.

The figure shows that the specimens from the *Z* build yielded an average hardness *HRB* of 60.6, which is about 10 % lower than the average hardness (*HRB* 66.9) recorded on the *XY* specimens. These results appear to follow the trend observed on the tensile strength results. The figure also shows that specimens from both printed builds resulted in a hardness considerably lower than the recorded on the baseline. This difference as well as that observed on the tensile strength is associated to the thermal load-history induced on the parts during the printing process.

MICROSTRUCTURE ANALYSIS

XRD INVESTIGATION

The XRD investigations combined with the chemical analysis information, revealed that the main phase of the hybrid manufactured samples was based on an iron nickel phase ($Fe_{0.66}Ni_{0.34}$). SEM/EDS investigations, reported below, indicate the presence of secondary phases. However, it was not possible to confirm the existence of a secondary phase using the Rigaku Miniflex XRD. Here, all the printed Invar samples showed similar diffraction peaks like the plot shown in Figure 9. This plot displays the top, middle, and bottom sections of the BRP90 sample in the *XY* orientation. Three diffraction peaks corresponding to the $Fe_{0.66}Ni_{0.34}$ phase (cubic unit cell, $a = 3.604$ Å) can be observed at $2\theta = 43.47$, 50.58, and 74.55, corresponding to (111), (200), and (220) crystallographic planes, respectively. It must be noted, the other set of three diffraction peaks at $2\theta = 41.61$, 48.32, and 70.92, are due to the contamination of the X-ray tube in the Rigaku Miniflex, with a sputtered tungsten-base phase from the tungsten target (formed in an over-

used X-ray tube). The difference in peak height observed in top, middle, and bottom samples might be related to the samples' texture and grain preferential orientation, related to the printing and localized cooling conditions. The differences in texture among the top, middle, and bottom samples were confirmed by further light microscopy studies. Figure 10 shows the XRD spectra obtained from three samples prepared from the commercial Invar 36 bar. Here, the primary crystallographic phase is iron nickel, as well; however, the $Fe_{0.65}Ni_{0.35}$ (PDF 04-006-6665) index indicates a slight difference in the chemical composition compared to the printed Invar 36.

OPTICAL MICROSCOPY

The optical microscopy study was only performed on the *XY* samples to investigate the morphological aspects of the printed system across the height. The study indicates microstructural differences among the bottom, middle, and top locations, irrespective of the sample set. Typical grain features are shown in Figure 11 under a low magnification dark field. Here, the average grain size seems to increase from the bottom sample to the top sample. Elongated grains are observed in the bottom and middle sample, while the top sample shows equiaxed grain. The preferential orientation of the elongated grains might be related to the localized cooling conditions in the bottom and middle volumes of the printed Invar 36. The increase in grain

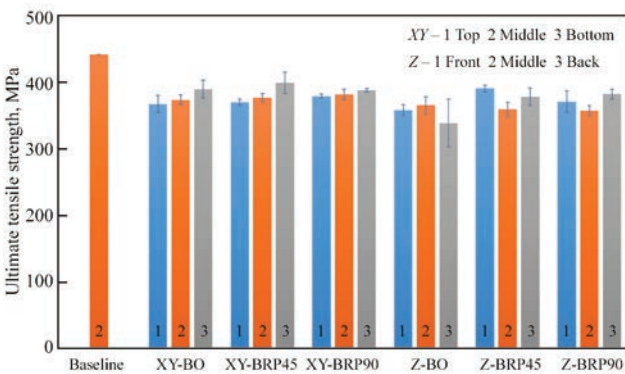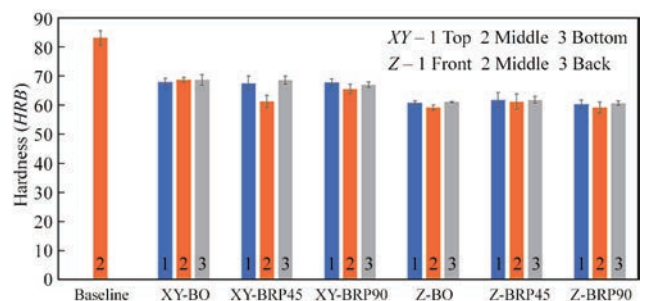**Figure 8.** Rockwell hardness (*HRB*) performance of the baseline and manufactured test specimen printed in *XY* and *Z* with B0, BRP45, and BRP90 orientations
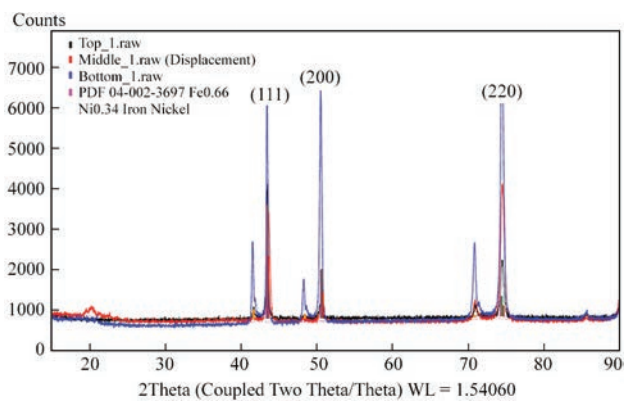
Figure 9. XRD spectra from top, middle, and bottom sections of XY-BRP90
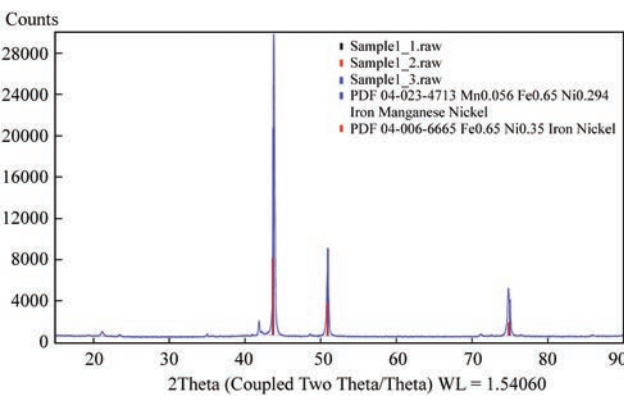
Figure 10. XRD spectra from commercially available Invar 36 baseline bar

Figure 11. Dark field LM micrographs of the cross-sectioned top (*a*), middle (*b*), and (*c*) bottom of Bi0 sample printed in *XY* orientation

size from the bottom to the top samples is highlighted on Figure 12 under a high magnification microscope.

The smaller grain size of the bottom sample, compared to the top one, might be explained by the fast-cooling conditions of the printed volume in contact with the build plate and the extended thermal history as shown by the infrared data. Figure 12 shows part of the laser track. The elongated grains of the bottom part grow perpendicular to the semicircular melt-pool boundary and toward the centerline of the melt pool, which is the hottest point of the molten pool. Due to the high thermal gradient in the direction orthogonal to the semicircular melt-pool boundary, epitaxial grain growth in this direction is the typical solidification mechanism that occurs in volumes of

bottom and middle parts. It is interesting to note the presence of micro-porosity on the printed samples, a feature that was observed near the edges of the specimens. Previous studies on powder and wire DED have shown that mechanisms associated with gas and bubbles trapped in the pool contribute to the formation of pores [33, 34]. This clearly suggests that a further optimization on the printing parameters is required to minimize such defects.

SEM/EDS INVESTIGATION

Figure 13 shows the typical secondary electron micrographs collected from the printed samples. The SEM investigation confirms the grain size increase from bottom to the top of the printed Invar 36 samples. Also, the micron-scale porosity seems to increase from the bottom to the top of the sample. Grain size [18] and porosity variation [25], combined with the variation in the chemical composition (see below) could explain the variation in the coefficient of thermal expansion (CTE) in the as-printed Invar 36.
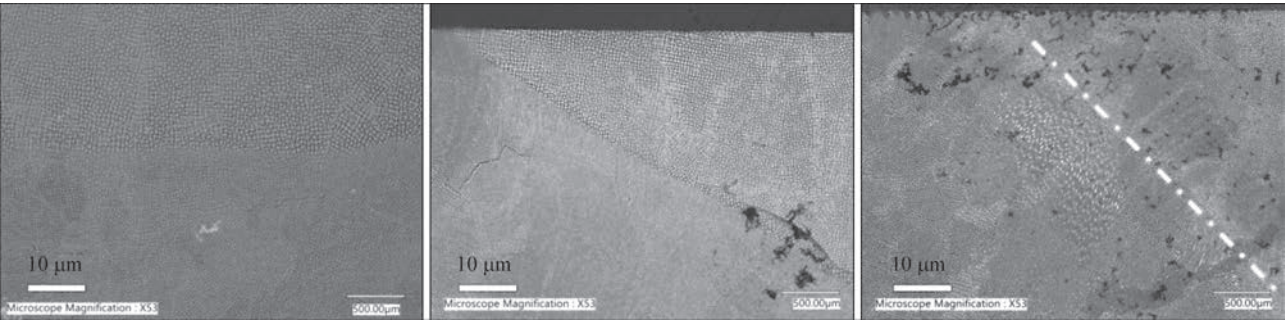
Figure 12. Typical bright field LM micrographs of the cross-sectioned top (*a*), middle (*b*) and bottom (*c*) volumes of Bi0 sample printed in *XY* orientation. Laser track in (*c*) indicated by dotted line
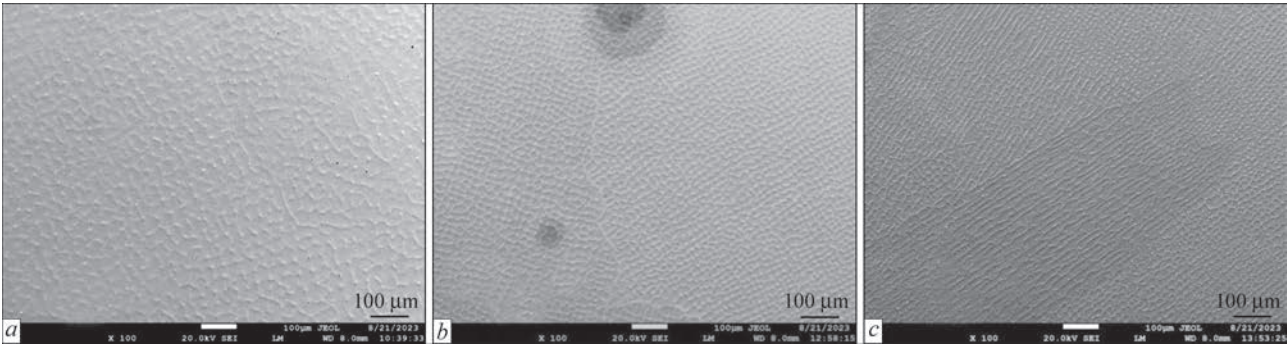
Figure 13. Secondary electron micrographs of the cross-sectioned XY-Bi0 sample top (*a*), middle (*b*) and bottom (*c*)
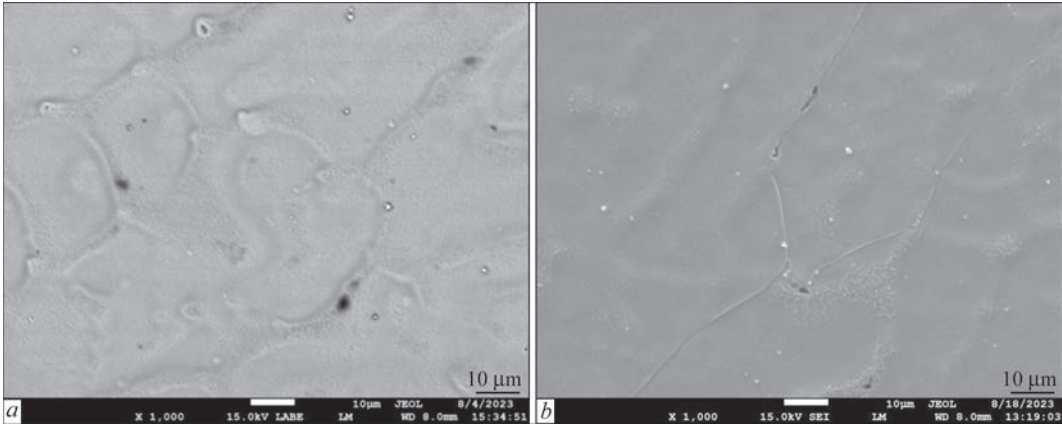
Figure 14. Representative SEM of the cross-sectioned samples: *a* — backscattered electron (BSE) micrograph of the XY-BRP90 specimen; *b* — secondary electron micrograph of the XY-BRP45 coupon

Figure 14 shows the representative backscattered electron (BSE) micrographs of the printed samples. For instance, the BSE contrast on the top sample collected from *XY* printed orientation (Figure 14, *a*), indicates the presence of at least two phases having different chemical (and very probably, crystallographic) content. Figure 14, *b* shows an electron micrograph of the bottom section of the XY sample, where elongated voids can be observed. The microscale voids dotting the crack path seem to be stress raisers for the applied stress.

Based on the EDS investigation, the chemical composition of all as-printed samples varies from the bottom to the top. A feature that could affect the mechanical and thermal properties of the printed coupons. This variation might be related to the change in printing conditions (printing parameters and printing environment), and to the presence of microvoids in the manufactured coupons. Figure 15, *a* shows the mean chemical composition of top, middle, and bottom volumes of a *XY* sample. The Fe content increases about 1.7 wt.% in between middle and top volumes, while
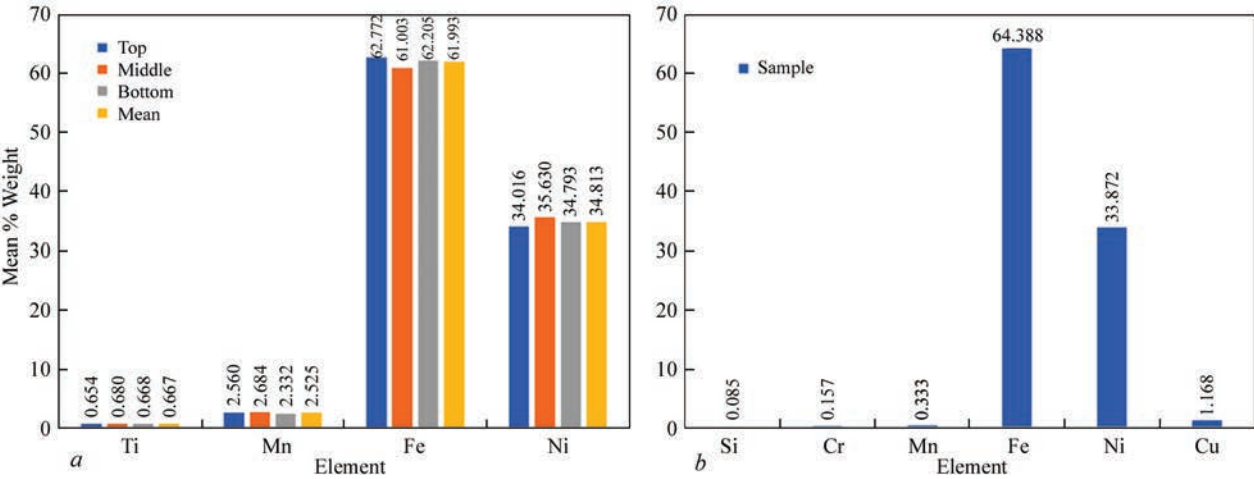
Figure 15. Chemical composition of top, middle, and bottom volumes of XY-BRP90, as determined by EDS investigation (*a*); chemical composition of commercially available Invar 36 rod, as measured in the present research (*b*)

Ni content decreases about 1.6 wt.%. This reduction in Ni content resulted in the higher CTE of printed parts. The Fe content in the hybrid manufactured Invar 36 sample is about 61.993 wt.%, while in the commercially available Invar 36 rod, the Fe content is about 64.388 wt.% (see Figure 15, *b*).

CONCLUSIONS

Test specimens manufactured using the Mazak LHWD hybrid system were studied in this work. The manufactured specimens were subjected to a series of mechanical and thermal tests to investigate their fundamental properties. The results showed that the printed parts exhibited a lower tensile and hardness performance than the commercially available material. Here, the samples obtained from the top section of the printed parts yielded higher mechanical properties than those extracted from the bottom; a feature associated to the heat sink performance provided by the building plate as well as to the larger thermal history to which the bottom sections were subjected to as recorded by an infrared camera. Indeed, an optical microscopy and SEM analysis revealed smaller crystal grains at the bottom of the printed samples than at the top. On the other hand, no clear distinction was observed on the coefficient of thermal expansion in terms of the printing location and manufacturing orientation. Here, although the printed samples resulted in a higher CTE than the commercially available Invar 36 stock material, their CTE values varied between 1.5 and 3 μm/m·°C. An ESD analysis showed that the printed samples yielded in average about 34 % Nickel, a percentage that could support their higher CTE. This work provides a preliminary study of DED printed Invar 36 as a feasible material for manufacturing low CTE composite tooling molds. Indeed, the incorporation of the hybrid technology will provide light-weight complex molds with tight dimensional requirements and surface finishes associated with typical subtracting CNC processes.

DISCLAIMER

The views and conclusions contained herein are those of the authors and should not be interpreted as necessarily representing the official policies or endorsements, either expressed or implied, of Air Force Research Laboratory or the U.S. Government.

REFERENCES

1. Acharya, S.S., Medicherla, V.R.R., Bapna, K. et al. (2021) Mixed ground state in Fe–Ni Invar alloys. *J. Alloys Compd.*, **863**, 158605.
2. Liu, H., Sun, Z., Wang, G. et al. (2016) Effect of aging on microstructures and properties of Mo-alloyed Fe–36Ni Invar alloy. *Materials Sci. and Eng.: A*, 654, 107–112.
3. Chen, C., Ma, B., Liu, B. et al. (2019) Refinement mechanism and physical properties of arc melted Invar alloy with different modifiers. *Mater. Chem. Phys.*, **227**, 138–147.
4. Ona, K., Sakaguchi, N., Ohno, H., Utsunomiya, S. (2020) The advanced super Invar alloys with zero thermal expansion for space telescopes. *Transac. of the Japan Soc. for Aeronautical and Space Sci., Aerospace Technology Japan*, **18**, 32–37.
5. Kim, B.G., Lee, D.G. (2009) The design of an optical sensor arrangement for the detection of oil contamination in an adhesively bonded structure of a liquefied natural gas (LNG) ship. *Meas. Sci. Technol.*, **20**, 065204.
6. He, G., Peng, X., Zhou, H. et al. (2023) Superior mechanical properties of Invar36 alloy lattices structures manufactured by laser powder bed fusion. *Materials*, **16**. DOI: https://doi.org/10.3390/ma16124433
7. Abbasi, S.M., Morakabati, M., Mahdavi, R., Momeni, A. (2015) Effect of microalloying additions on the hot ductility of cast FeNi36. *J. Alloys Compd.*, **639**, 602–610.
8. Martín-García, J.M., Portugal, R., Manssur, L.R.U. (2007) The Invar tensor package. *Comput. Phys. Commun.*, **177**, 640–648.
9. Wegener, T., Brenne, F., Fischer, A. et al. (2021) On the structural integrity of Fe–36Ni Invar alloy processed by selective laser melting. *Additive Manufacturing*, **37**, 101603.

10. Yakout, M., Elbestawi, M.A. (2020) Insights on laser additive manufacturing of Invar 36. In *Additive Manufacturing Applications for Metals and Composites*. IGI Global.

11. Sahoo, A., Medicherla, V.R.R. (2021) Fe–Ni Invar alloys: A review. *Materials Today: Proc.*, **43**, 2242–2244.

12. Kim, S.H., Choi, S.G., Choi, W.K. et al. (2014) Pulse electrochemical machining on Invar alloy: Optical microscopic/SEM and Non-contact 3D measurement study of surface analyses. *Appl. Surf. Sci.*, **314**, 822–831.

13. *Gil Del* Val, A., Cearsolo, X., Suarez, A. et al. (2023) Machinability characterization in end milling of Invar 36 fabricated by wire arc additive manufacturing. *J. of Materials Research and Technology*, **23**, 300–315.

14. Zhao, Y., Wu, A.P., Ren, J.L. et al. (2013) Temperature and force response characteristics of friction stir welding on Invar 36 alloy. *Sci. Technol. Weld. Joining*, **18**, 232–238.

15. Jiang, Z., Chen, X., Li, H. et al. (2020) Grain refinement and laser energy distribution during laser oscillating welding of Invar alloy. *Mater. Des.*, **186**, 108195.

16. Huang, G., He, G., Liu, Y., Huang, K. (2024) Anisotropy of microstructure, mechanical properties and thermal expansion in Invar 36 alloy fabricated via laser powder bed fusion. *Additive Manufacturing*, **82**, 104025.

17. Rishmawi, I., Rogalsky, A., Vlasea, M. et al. (2022) The effects of heat treatment on tensile and thermal expansion behavior of laser powder-bed fusion Invar 36. *J. Mater. Eng. Perform.*, **31**, 9727–9739.

18. Huang, G., He, G., Peng, X. et al. (2024) Effect of processing parameters on the microstructure, mechanical properties and thermal expansion behavior of Invar 36 alloy manufactured by laser powder bed fusion. *Materials Sci. and Eng.: A*, **897**, 146329.

19. Ren, G., Cui, Z., Hao, X. et al. (2024) Effect of subgrain microstructure on the mechanical properties of Invar 36 specimens prepared by laser powder bed fusion. *J. Alloys Compd.*, **1004**, 175839.

20. Guo, H., Liu, D., Xu, M. et al. (2024) Preparation, characterization and composition optimization design of laser powder bed fusion continuously graded Invar 36/316L stainless steel alloys. *Mater. Charact.*, **209**, 113709.

21. Asgari, H., Salarian, M., Ma, H. et al. (2018) On thermal expansion behavior of Invar alloy fabricated by modulated laser powder bed fusion. *Mater. Des.*, **160**, 895–905.

22. Yakout, M., Elbestawi, M.A., Veldhuis, S.C. (2018) A study of thermal expansion coefficients and microstructure during selective laser melting of Invar 36 and stainless steel 316L. *Additive Manufacturing*, **24**, 405–418.

23. Garibaldi, M., Ashcroft, I., Simonelli, M., Hague, R. (2016) Metallurgy of high-silicon steel parts produced using selective laser melting. *Acta Mater.*, **110**, 207–216.

24. Tan, H., Wang, Y., Wang, G. et al. (2020) Investigation on microstructure and properties of laser solid formed low expansion Invar 36 alloy. *J. of Materials Research and Technology*, **9**, 5827–5839.

25. Huang, G., He, G., Gong, X. et al. (2024) Additive manufacturing of Invar 36 alloy. *J. of Materials Research and Technology*, **30**, 1241–1268.

26. Yang, Q., Wei, K., Yang, X. et al. (2020) Microstructures and unique low thermal expansion of Invar 36 alloy fabricated by selective laser melting. *Mater. Charact.*, **166**, 110409.

27. Carroll, B.E., Palmer, T.A., Beese, A.M. (2015) Anisotropic tensile behavior of Ti–6Al–4V components fabricated with directed energy deposition additive manufacturing. *Acta Mater.*, **87**, 309–320.

28. Wang, Z., Palmer, T.A., Beese, A.M. (2016) Effect of processing parameters on microstructure and tensile properties of austenitic stainless steel 304L made by directed energy deposition additive manufacturing. *Acta Mater.*, **110**, 226–235.

29. Tian, Y., McAllister, D., Colijn, H. et al. (2014) Rationalization of microstructure heterogeneity in Inconel 718 builds made by the direct laser additive manufacturing process. *Metall. Mater. Transact. A*, **45**, 4470–4483.

30. Sridharan, N., Gussev, M., Seibert, R. et al. (2016) Rationalization of anisotropic mechanical properties of Al-6061 fabricated using ultrasonic additive manufacturing. *Acta Mater.*, **117**, 228–237.

31. Wang, P., Tan, X., Nai, M.L.S. et al. (2016) Spatial and geometrical-based characterization of microstructure and microhardness for an electron beam melted Ti–6Al–4V component. *Mater. Des.*, **95**, 287–295.

32. Ngo, T.D., Kashani, A., Imbalzano, G. et al. (2018) Additive manufacturing (3D printing): A review of materials, methods, applications and challenges. *Composites Pt B*, **143**, 172–196.

33. Zhang, K., Chen, Y., Marussi, S. et al. (2024) Pore evolution mechanisms during directed energy deposition additive manufacturing. *Nat. Commun.*, **15**, 1715.

34. Yi, H., Yang, L., Jia, L. et al. (2024) Porosity in wire-arc directed energy deposition of aluminum alloys: Formation mechanisms, influencing factors and inhibition strategies. *Additive Manufacturing*, **84**, 104108.

ORCID

Bharat: 0000-0002-4580-6329

Mario Rodriguez: 0009-0000-9969-9656

Holly Martin: 0009-0007-0835-1680

Brian Vuksanovich: 0000-0002-7212-5801

Virgil Solomon: 0000-0003-2990-855X

Eric MacDonald: 0000-0002-9356-1223

Yousub Lee: 0000-0002-5563-0419

Thomas Feldhausen: 0000-0002-7311-5189

CONFLICT OF INTEREST

The Authors declare no conflict of interest

CORRESPONDING AUTHOR

Bharat Yelamanchi

Youngstown State University, OH USA 44555.

E-mail: byelamanchi@ysu.edu

SUGGESTED CITATION

JOURNAL HOME PAGE

https://patonpublishinghouse.com/eng/journals/tpwj

INVESTIGATION OF CORROSION RESISTANCE OF MIXED ZINC ALUMINUM AND MAGNESIUM COATINGS IN VARYING ACIDIFIED SALINE ENVIRONMENTS

W. Rejmer[1], P. Matyszkiel[1], E. Cieszyńska-Bońkowska[2], C. Senderowski[3]

[1]Univesity of Warmia and Mazury in Olsztyn, Department of Materials and Machines Technology, Oczapowskiego 11, 10-719 Olsztyn, Poland
[2]Enzeit Technik, ul. Przejazdowa 21,05-800 Pruszków, Poland
[3]Warsaw University of Technology, Institute of Mechanics and Printing, Narbutta 85, 02-524 Warsaw, Poland

ABSTRACT

The increasing drive to use light materials, which will also meet the demands of industry, causes growing interest in zinc mixed coatings. Especially compositions of zinc, aluminum and magnesium are of considerable interest due to their sacrificial protection of coated steel sheet metal in neutral and saline environments. The question that materials experts face is the amount of coating used for anticorrosive protection, as it can significantly lower the cost of large-scale installations. In the presented research, corrosion parameters of commercially available coating with three varying coating masses are assessed. The tests were performed using Linear Polarization Resistance Method, which allows for determination of electrochemical parameters and corrosion wear. The obtained results show that a coating with the most mass does not always provide the most optimal protection in all environments. It is suggested that lower coating masses may lead to more uniform deposition of protective products of electrochemical reactions. Additionally it was found out that thickness of substrate leads to different corrosion protection parameters in same thickness coatings.

KEYWORDS: zinc-magnesium aluminum coatings, electrochemical corrosion, corrosion wear

INTRODUCTION

Corrosive material degradation costs the world economy trillions of dollars. The increase in demand for new materials and their cost is leading to a reassessment of materials testing in this field [1]. Norms for assessment of corrosive resistance of materials often employ testing in neutral environments. However, the increasing acidification of the environment caused by industrial processes and climate change should lead to more considerable testing in higher hydrogen ion concentrations [2]. Increased greenhouse gas emissions will inevitably lead to reductions in the pH of oceanic and intracontinental water environments. It is estimated that within the next two decades, the pH value of seawater will change from 8 to 7 [3, 4]. In addition, polluted industrial environments contain acidic ions, such as SO_4^{2-}, CO_3^{2-} and Cl^-; these ions originate from industrial effluents and can cause structural failure [5]. It is widely understood that fluid acidity, particularly highly aggressive acidic ions, is critical in the corrosion and degradation of metal alloys [5, 6]. A variety of mechanisms can cause corrosion. Its early stages can benefit further protection by forming dense protective layers on the surface, which can significantly reduce the corrosion rate [7, 8]. Examination of the time-dependent damage processes revealed that a surface corrosion layer can mitigate the influence of tensile stress on the the Ni–Cr–Mo–V [9]. Zinc and other amphoteric coating materials applied to metallic surfaces are of considerable interest for this reason alone. Various order elements, such as aluminum and magnesium, are also added to improve the anodic properties of zinc [10, 11]. Zinc coating has excellent corrosion resistance and protection against steel corrosion. It has great application prospects in the corrosion protection of iron and steel materials. Its chemical and electrochemical properties lead to the formation of a metal oxide or carbonate layer in the atmosphere, which covers the surface of the alloy and prevents further oxidation. This is due to the fact that the standard potential of zinc is more anodic than the standard potential of iron. Therefore, the galvanized layer with more negative potential will corrode preferentially even when a local breakage occurs. Furthermore, it still has electrochemical protection for steel, sacrificing itself to protect iron-containing substrates. However, environmental changes and the needs of application scenarios impose stringent requirements on the corrosion resistance of Zn coatings. Corrosion experiments on Zn–Al–Mg alloy coating have been widely conducted. Tests at marine test sites revealed that increasing the eutectic content of the coating improved the corrosion resistance. This finding is related to the formation of stable layered double hydroxides. Similar studies under varying atmospheric conditions for up to 6 years showed that mixed zinc–aluminum–magnesium coatings exhibited excellent corrosion resistance with an

average mass loss ratio of around 3 suggesting that their high corrosion resistance is related to the formation of protective corrosion products [12].

To shorten the time of corrosion experiments, Zn alloy coatings are often studied under simulated environmental conditions in the laboratory rather than in conventional atmospheric environments, in which corrosion is slow. Accelerated studies revealed two types of corrosion areas: grey and white coloured. Both contained hydroxyl zinc, but most of the grey regions comprised hydroxyl zinc chloride, while most of the white areas were sparsely packed substances such as zinc carbonate. The inner corrosion products were dense layered double hydroxides which serve a protective role [13]. Other research in accelerated environments investigated the types of corrosion products and percentages of stabilized products in the coating. Those studies proposed that Mg is preferentially corroded in the coating and that the corrosion products buffer the pH and inhibit oxygen reduction [13]. Experimental evidence has been found that zinc-magnesium-aluminium alloy underwent localized corrosion (similar to pitting corrosion) under high pH conditions, indicating that this alloy might not be suitable in such conditions [14]. The research aims to assess coating mass's influence on its electrochemical properties in a mildly acidified saline environment.

MATERIALS AND METHODS

The research material consisted of Zn3.5Al3Mg type coatings produced by ArcelorMittal by the hot-dip galvanizing method [15] on S350GD and S320GD steel substrates of various thicknesses. The investigation focused on three coating types with varying substance weights (310, 430 and 620 g/m²) and different coating thicknesses. The coatings were coated on both sides and were designated ZM-310, ZM-430, and ZM-620. The ZM-310 coating was applied to a steel material measuring 1.5 mm in thickness, while the ZM-430 coating was applied to steel materials measuring 2.5 and 3 mm thick. In contrast, the ZM-620 coating was the sole product manufactured on S320GD steel with a thickness of 3 mm. According to the manufacturer of the tested coatings, the main component is zinc with 3 wt.% magnesium and 3.5 wt.% aluminium. The structure properties and chemical composition of the coating's surface were analyzed with a Quanta FEG 250 scanning microscope integrated with an EDAX x-ray microanalysis detector. Sodium chloride solutions of 0.25, 0.5 and 1M were used for corrosive testing. Such environments are comparable to environments presented in ISO–12944. The first solution is similar to C4-type environments: chemical plants, swimming pools, ship and boat repair yards, industrial areas, and

coastal areas with medium salinity. The second most concentrated solution has corrosion similar to C5 environments: buildings or areas with almost continuous condensation and high pollution, industrial areas with high humidity and aggressive atmosphere. The most concentrated solution gives results similar to C5–M, structures or areas with almost continuous condensation and high pollution, coastal and offshore areas inland with high salinity [16]. Crystalline sodium chloride (99 % weight ratio, Chempur Poland) and buffer solution with a pH value of 6.5 achieved through the use of (Chempur, Poland) were used to prepare a slightly acidic environment. The study consisted of measurements using the Linear Polarization Resistance (LPR) method. To perform the measurement, a degreased sample (ethanol 96 % by volume) should be placed in an electrochemical vessel and connected to a potentiostat-galvanostat (Atlas 1131). The LPR method involves stabilizing the electrochemical system to a fixed potential, lowering its potential by ΔE, and raising it above the stationary potential by the same amount. During the measurement, the results of the sample potential (V) and the density of the flowing current are read (A/m²). The density of the flowing current is related to the amount of corrosion processes occurring on the metal surface. The resulting polarization curve consists of two parts: the anodizing and cathodizing curve. Tafel curves are then drawn to the anodizing and cathodizing curves. The intersection point of the Tafel curves allows the current density and corrosion potential to be read (Figure 1).

Corrosion wear was determined from the corrosion current values based on Faraday's law (1) [2].

$$m = \frac{MIt}{zF},\qquad(1)$$

m — mass of corroded material, g; M — molar mass of metal undergoing reaction, g/mol; z — amount of
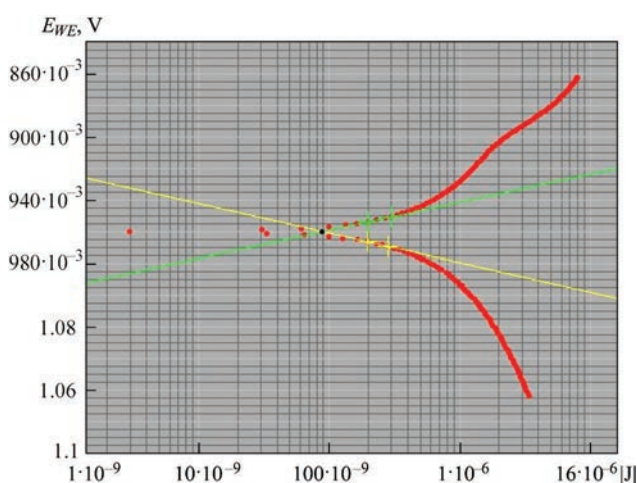
Figure 1. Example of a polarization curve with Tafel tangents

electrons given up in a single oxidation process; F — Faraday's constant 96500, °C/mol; I — corrosion current density, A cm^{-2}; t — time, s.

In order to calculate corrosion wear, the mass percentage composition of the coating was converted to atomic percentage. Subsequently, the molar mass of the alloy was determined to be 59 g/mol. Given that 96.5 % of the coating composition comprises zinc and magnesium, which donate two electrons during the oxidation process, it was assumed that the number of electrons donated per unit process would be 2. To determine the life of the coating, the corrosion potentials of the individual coating components and the amount of coating per square meter of material were used.

RESULTS

SEM ANALYSIS

The SEM/EDS examinations (Figure 2 and Table 1) revealed that two thinner coatings (Figures 2, *a*, *b*) were characterized by a more homogeneous layered structure with numerous material defects in the form of grooves and microcracks with visible grains delamination on the coating surface (Figure 2, *b*). The

coatings structure is formed of elongated grains consisting of the solid solution areas of Al in Zn (α) on a formed eutectic background (α+β).

It is generally accepted that immersion time and bath temperature influence the cracking and delamination of the primary diffusion layer at the interface with the steel substrate material. However, forming brittle intermetallic phases from the Fe–Al system due to the diffusion of iron from the steel substrate plays a significant role in the delamination of the structure of thin coatings in this zone [17]. A SEM/EDS study of the chemical composition in micro-areas allowed to establish that the most probable phase forming the diffusion layer in the interface with the steel substrate is the FeAl$_3$(Zn), which in the final stage of structure formation transforms, creating micro-areas with the participation of even more brittle Fe$_2$Al$_5$(Zn) phase. This causing microcracks and delamination of layers, as visible in the structure of the ZM-430 coating (Figure 2, *b*). The structure of the same ZM-430 coating on 3 mm thick S350GD steel shows the influence of the steel substrate on the formation of a layer with a high degree of surface development (Figure 2, *c*). Most likely, this effect is due to the high residual stresses that arise from the differing linear coefficients of
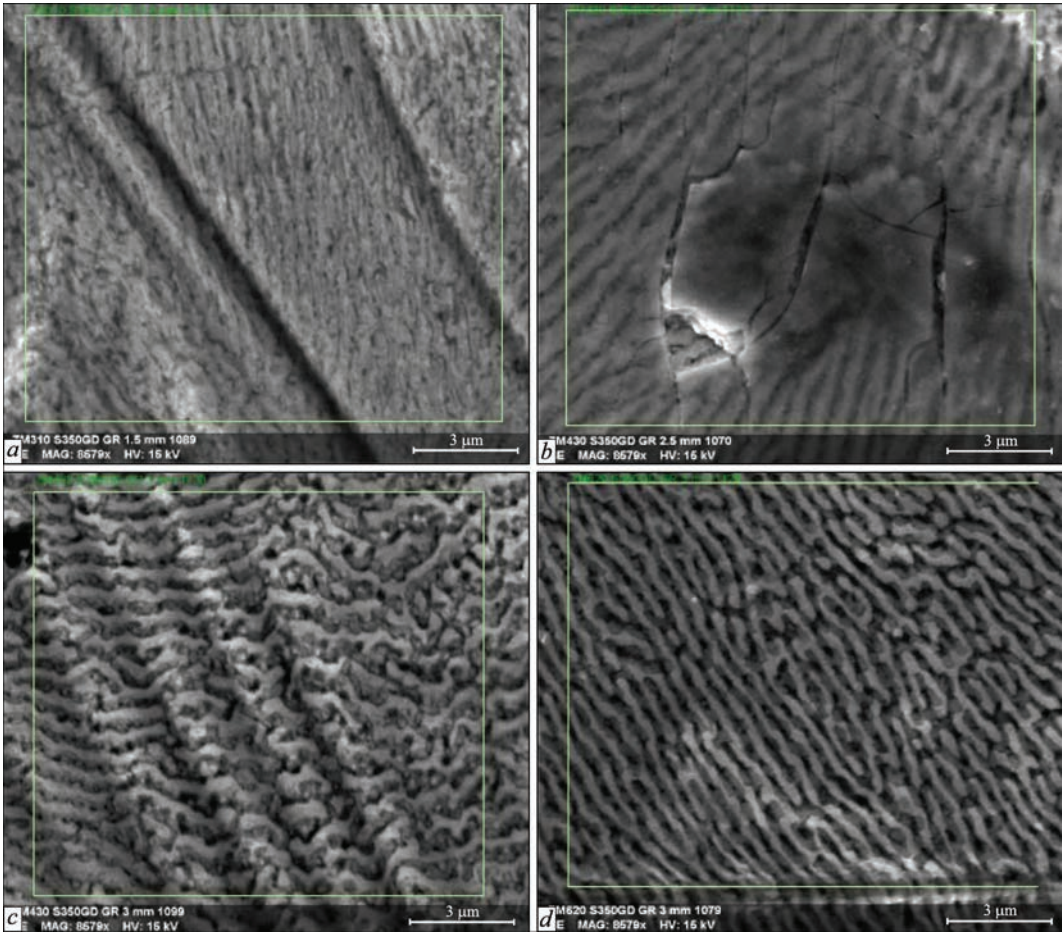
Figure 2. Example SEM/ SE images for: ZM-310 — on 1.5 mm steel (*a*); ZM-430 — on 2.5 mm (*b*) and 3 mm steel (*c*), respectively; and ZM 620 — on 3 mm steel (*d*)

thermal expansion between the steel substrate and the complex, heterogeneous structure of the Zn–Al–Mg coating, which contains high-aluminium intermetallic phases from the Fe–Al system. Studies of Zn–Mg–Al alloy coatings have shown that one of the causes of crack formation is the tensile stresses within the structure, primarily generated by an increased cooling rate [18]. Depending on the thickness of the substrate material and the obtained coating, this phenomenon can influence the proportion of micro-cracks and the microstructural characteristics of the tested coatings. This effect can be observed for ZM-430 coatings of the same weight applied to S350GD steel substrate with different thicknesses of 2.5 and 3 mm. Analysis of the obtained results shows a favourable effect of grain growth kinetics on the structure formation of the ZM-620 coating, produced in a hot dip bath on 3 mm thick S320GD steel. By increasing the thickness of the coating, the rate of the Fe–Al reaction and the formation of brittle intermetallic phases are eliminated, resulting in a more structurally uniform coating in the surface area with no visible material defects (Figure 2, *d*). Microanalysis of the chemical composition on the surface of the ZM-620 coating shows similar amounts of magnesium as indicated by the manufacturer. It has also been found that as the mass (thickness) of the coating increases, the percentage of alloying elements decreases and the carbon and oxygen content increases (Table 1). The formation of carbonate layers, also

Figure 3. Average values of corrosion potentials

found in [19], is most likely responsible for this. Carbonates form an oxidised protective layer but, unfortunately, are also thought to be permeable to acidic environments.

LPR ANALYSIS

Corrosion potential results are presented in Figure 3 and Table 2. Except for the ZM-310 coating, every other coating has exhibited the highest corrosion potential values in 0.25 M NaCl. The ZM-310 coating showed the lowest corrosion potential in this solution, –1.05±0.01 V. In the least saline solution, the 3 mm thick samples coated with ZM-430 coatings showed the highest average potentials (–0.97±0.009 V), but in most saline solutions, gave the lowest potentials (–1.03±0.01 V). The differences between potentials are minor and can be assumed to be the same. In higher salinity solutions, the highest potential was measured for the ZM-430 coating on 2.5 mm steel substrate (0.98±0.01 V in both solutions). It is worth noting that this coating exhibits the least variation in potential when salinity conditions are changed. This

Table 1. Semiquantitative EDS analysis of coatings surfaces

Element	ZM-310 1.5 mm		ZM-430 2.5 mm	
	wt.%	at.%	wt.%	at.%
Zinc	82.22±0.56	55.52±0.92	80.44±4.24	52.79±7.07
Oxygen	5.62±0.06	15.52±0.33	6.60±2.33	17.33±5.13
Carbon	4.24±0.38	15.58±1.25	4.8±0.77	16.95±1.55
Aluminum	4.47±0.1	7.31±0.24	4.30±0.44	6.79±0.52
Magnesium	3.28±0.06	5.90±0.05	2.96±0.09	5.21±0.31
Chromium	0.2±0.35	0.17±0.29	0.5±0.53	0.39±0.34
Phosphorus	0	0	0.4±0.36	0.53±0.47

Table 1. Cont.

Element	ZM-430 3 mm		ZM-620 3 mm	
	wt.%	at.%	wt.%	at.%
Zinc	80.88±2.68	52.86±4.09	77.15±3.42	46.83±4.93
Oxygen	5.50±1.64	14.56±3.58	8.56±2.10	20.99±4.13
Carbon	5.45±0.43	19.33±0.87	6.32±0.66	20.78±1.20
Aluminum	4.6±0.19	7.28±0.57	3.91±0.21	5.74±0.41
Magnesium	3.17±0.1	5.56±0.09	2.66±0.32	4.34±0.61
Chromium	0.22±0.39	0.17±0.3	0.85±0.27	0.64±0.18
Phosphorus	0.18±0.31	0.23±0.4	0.53±0.46	0.68±0.59

Table 2. Results of corrosion potentials

Coating, mm	Corrosion potential, V			
	Measurement 1	Measurement 2	Measurement 3	Measurement 4
0.25 M NaCl				
ZM310_1.5	–1.05	–1.06	–1.05	–1.04
ZM430_2.5	–0.99	–0.97	–0.97	–0.97
ZM430_3	–0.97	–0.96	–0.97	–0.96
ZM620_3	–1.00	–0.98	–0.97	–0.98
0.5 M NaCl				
ZM310_1.5	–1.03	–1.04	–1.03	–1.02
ZM430_2.5	–0.98	–0.97	–0.98	–0.98
ZM430_3	–0.99	–0.99	–1.00	–1.01
ZM620_3	–1.01	–0.98	–0.99	–0.99
1 M NaCl				
ZM310_1.5	–1.01	–1.02	–1.01	–1.00
ZM430_2.5	–0.98	–0.97	–0.99	–0.99
ZM430_3	–1.02	–1.04	–1.03	–1.04
ZM620_3	–1.00	–1.01	–1.01	–1.00
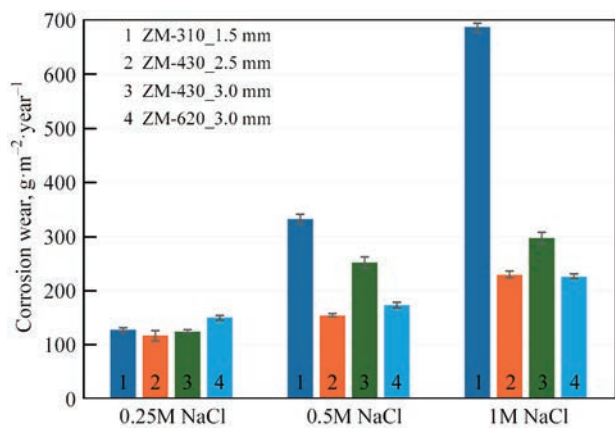
Figure 4. Coating corrosion wear

Table 3. Corrosion wear of coatings

Coating	Corrosion wear, $g \cdot m^{-2} \cdot year^{-1}$			
	Measurement 1	Measurement 2	Measurement 3	Measurement 4
0.25 M NaCl				
ZM-310, 1.5 mm	131.20	121.07	126.86	126.86
ZM-430, 2.5 mm	123.97	108.05	123.48	107.08
ZM-430, 3 mm	124.93	123.97	119.62	126.38
ZM-620, 3 mm	150.98	143.26	147.60	153.39
0.5 M NaCl				
ZM-310, 1.5 mm	320.29	337.36	328.00	339.58
ZM-430, 2.5 mm	150.50	152.91	155.32	155.32
ZM-430, 3 mm	258.54	236.35	260.47	249.86
ZM-620, 3 mm	171.72	164.97	174.61	176.54
1 M NaCl				
ZM-310, 1.5 mm	686.88	685.91	678.19	697.49
ZM-430, 2.5 mm	228.64	225.74	237.32	223.81
ZM-430, 3 mm	288.45	299.06	289.41	310.64
ZM-620, 3 mm	224.78	218.99	227.67	229.60

may be attributed to the high oxygen content in the coating, possibly resulting from protective oxide layers [20]. The ZM 310 coating is predominantly zinc and aluminium rich in the surface layer, which, due to the lowest anodic potential of these metals, may cause a potential increase with increasing salinity [21].

In all of the investigated environments, the lowest average corrosion wear in 0.25 M and 0.5 M NaCl is exhibited by the ZM-430 coating on steel with a thickness of 2.5 mm, which amounts to 115.6 ± 9.34 $g \cdot m^{-2} \cdot year^{-1}$, 153.31 ± 2.31 $g \cdot m^{-2} \cdot year^{-1}$, respectively. In most saline solution, the most minor corrosion wear is exhibited by ZM-620 coating (225.26 ± 4.62 $g \cdot m^{-2} \cdot year^{-1}$). In 0.25 M NaCl environment, the ZM-620 coating showed the highest corrosion wear (148.81 ± 4.39 $g \cdot m^{-2} \cdot year^{-1}$). In higher salinity corrosive environments, the highest corrosion wear for coating ZM-310 was calculated to be 331.31 ± 8.90 $g-m^{-2} \cdot year^{-1}$ for 0.5 M environment and 687.12 ± 7.93 $g \cdot m^{-2} \cdot year^{-1}$ for 1 M NaCl (Table 3). During corrosion tests in 1M NaCl solution sample ZM-310 exhibited orange coloring of solution. This observation is probably caused by coating penetration and resulting presence of iron salts in the solution. Additionally the corrosion products of other samples exhibited a white-gray color while ZM-310 sample exhibited black corrosion products, which may be composed of non soluble Fe^{2+} and Fe^{3+} salts. Both of these observations can be related to coating penetration.

The average corrosion wear values are shown in Figure 4, while results from singular measurements are shown in Table 3. Corrosion wear seems to be dependent on coating mass, but not directly. In lower salinity solutions, the most densely coated sample (with ZM-620 coating) shows higher corrosion wear values, which increase less with increasing salinity. It can be assumed that ZM-620 coating is more effective in creating other protective layers due to the

high carbon content associated with carbonate salts, and hydroxides layered [21].

CONCLUSIONS

Amount of coating used on steel sheet determines to some extent its corrosion properties. However the highest amount of coating does not always lead to higher potentials and lower corrosion wear. It may be suggested that deposition of substances to top of the coating can be more beneficial in materials with lower coating content. Coating ZM-430 dipped onto 2.5 mm steel sheet exhibits smaller corrosion wear and higher corrosion potentials in some environments than ZM-610 and ZM-430 on thicker steel sheets which can be attributed to different cooling rates.

ACKNOWLEDGEMENT

REFERENCES

1. Ossai, C.I., Boswell, B., Davies, I.J. (2015) Pipeline failures in corrosive environments — A conceptual analysis of trends and effects. *Eng. Failure Analysis*, **53**, 36–58. DOI: https://doi.org/10.1016/j.engfailanal.2015.03.004

2. Senderowski, C., Rejmer, W., Vigilianska, N., Jeznach, A. (2024) Changes in corrosion behaviour of zinc and aluminium coatings with increasing seawater acidification. *Materials*, **17**(**3**), 536. DOI: https://doi.org/10.3390/ma17030536

3. Hao, X., Ruihong, Y., Zhuangzhuang, Z. et al. (2021) Greenhouse gas emissions from the water–air interface of a grassland river: A case study of the Xilin River. *Sci. Rep.*, **11**, 2659. DOI: https://doi.org/10.1038/s41598-021-81658-x

4. Chen, CT.A., Lui, HK., Hsieh, CH. et al. (2017) Deep oceans may acidify faster than anticipated due to global warming. *Na-*

ture Clim. Change, **7**, 890–894. DOI: https://doi.org/10.1038/s41558-017-0003-y

5. Xu, Y. Huang, Y. Cai, F. Lu, D. Wang X. (2022) Study on corrosion behavior and mechanism of AISI 4135 steel in marine environments based on field exposure experiment. *Sci. of the Total Environment*, **830**, 154864. DOI: https://doi.org/10.1016/j.scitotenv.2022.154864

6. Hao, W. Liu, Z. Wu, W.X. Li, Cuiwei Du, Zhang, D. (2017) Electrochemical characterization and stress corrosion cracking of E690 high strength steel in wet-dry cyclic marine environments. *Materials Sci. and Eng.: A*, **710**, 318–328. DOI: https://doi.org/10.1016/j.msea.2017.10.042

7. Song, Y. Liu, R. Cui, Y. Meng, F. Liu, L.Wang, F.(2023) Corrosion of high-strength steel in 3.5 % NaCl solution under hydrostatic pressure: Initial corrosion with tensile stress coupling. *Corrosion Sci.*, **219**, 111229. DOI: https://doi.org/10.1016/j.corsci.2023.111229

8. LeBozec, N. Thierry, D. Persson, D. Riener, C.K. Luckeneder, G. (2019) Influence of microstructure of zinc-aluminium-magnesium alloy coated steel on the corrosion behavior in outdoor marine atmosphere. *Surface and Coatings Technology*, **374**, 897–909. DOI: https://doi.org/10.1016/j.surfcoat.2019.06.052

9. Huanhuan Wei, Yiqun Tang, Chen Chen, Peifeng Xi, (2024) Corrosion behavior and microstructure analysis of butt welds of Q690 high strength steel in simulated marine environment. *J. of Building Eng.*, **84**, 108509. DOI: https://doi.org/10.1016/j.jobe.2024.108509

10. Dolgikh, O., Simillion, H., Lamaka, S.V. et al. (2019) Corrosion protection of steel cut-edges by hot-dip galvanized Al(Zn, Mg) coatings in 1 wt.% NaCl: Pt I. Experimental study. *Materials and Corrosion*, **70**, 768–779. DOI: https://doi.org/10.1002/maco.201810209

11. Predko, P., Rajnovic, D., Grilli, M.L. et al. (2021) Promising methods for corrosion protection of magnesium alloys in the case of Mg–Al, Mg–Mn–Ce and Mg–Zn–Zr: A recent progress review. *Metals*, **11**(**7**), 1133. DOI: https://doi.org/10.3390/met11071133

12. Thierry, D., Persson, D., LeBozec, N. (2024) *Lo*ng-term atmospheric corrosion rates of Zn55 Al-coated steel. *Mater. Corros.*, **75**, 694–704. DOI: https://doi.org/10.1002/maco.202314209

13. Schürz, S., Luckeneder, G.H., Fleischanderl, M. et al. (2010) Chemistry of corrosion products on Zn–Al–Mg alloy coated steel. *Corrosion Sci.*, **52**. DOI: https://doi.org/10.1016/j.corsci.2010.05.044

14. Romina Krieg et al. (2014) Corrosion of zinc and Zn–Mg alloys with varying microstructures and magnesium contents. *J. Electrochem. Soc.*, **161**, C156. DOI: https://doi.org/10.1149/2.103403jes

15. https://industry.arcelormittal.com/industry/repository/fce/Brochures/Magnelis_book_EN.pdf (available at 11.10.2024)

16. ISO 12944

17. Kania, H. (2017) *Structure shaping and corrosion resistance of Zn–Al coatings obtained in hot dip metallization*. Gliwice, Silesian University of Technology.

18. Jihun Choi, Eui-Jin Jung, Dong-Jae Park et al. (2024) Impact of cooling rates on the microstructure and cracking susceptibility of hot-dip galvanized Zn–12 wt.% Al–5 wt.% Mg coatings. *Surf. and Coat. Technol.*, **488**, 131050. DOI: https://doi.org/10.1016/j.surfcoat.2024.131050

19. Prosek, T., Larché, N., Vlot, M. et al. (2010) Corrosion performance of Zn–Al–Mg coatings in open and confined zones in conditions simulating automotive applications. *Materials and Corrosion*, **61**, 412–420. DOI: https://doi.org/10.1002/maco.200905425

20. Zaid, B., Saidi, D., Benzaid, A., Hadji, S. (2008) Effects of pH and chloride concentration on pitting corrosion of AA6061 aluminum alloy. *Corrosion Sci.*, **50**, 1841–1847. DOI: https://doi.org/10.1016/j.corsci.2008.03.006

21. Martin, A., Texier-Mandoki, N., Crusset, D. et al. Corrosion behavior and sacrificial properties of Zn and Zn–Al coatings in conditions simulating deep geological disposal of radioactive waste at 80 ℃. *Coatings*, 12(**8**), 1044. DOI: https://doi.org/10.3390/coatings12081044

ORCID

W. Rejmer: 0000-0002-1955-1553

C. Senderowski: 0000-0001-9584-3139

CONFLICT OF INTEREST

The Authors declare no conflict of interest

CORRESPONDING AUTHOR

W. Rejmer

Univesity of Warmia and Mazury in Olsztyn,

Department of Materials and Machines Technology,

Oczapowskiego 11, 10-719 Olsztyn, Poland.

E-mail: wojciech.rejmer@uwm.edu.pl

CORROSION-MECHANICAL STATE OF THE HEAT PIPELINE AFTER LONG-TERM OPERATION

P. Yukhymets[1], L. Nyrkova[1], R. Dmytriienko[1], H. Kaminski[2], C. Zaruba[2], P. Linhardt[2], G. Ball[2], V. Yehorenko[3]

[1]E.O. Paton Electric Welding Institute of the NASU
11 Kazymyr Malevych Str., 03150, Kyiv, Ukraine
[2]Technical University of Vienna. Karlsplatz 13, 1040 Vienna, Austria
[3]CE "Kyivteploenergo". 5 Ivan Franko Sq., 01001, Kyiv, Ukraine

ABSTRACT

Metal properties of heat pipeline areas thinned under operating conditions is necessary component for determining its real state, and therefore their research is an actual task. The work investigates the corrosion-mechanical state of a heating pipeline made of BSt3sp steel after more than 40 years of operation. Based on the conducted research, it was established that corrosion of the feeding pipeline is more severe than that of the return pipeline, while the external corrosion of the pipelines is more intense than the internal one. The cracking of the oxide layer accelerates with increasing stresses in the range of the design pressure and leads to the activation of corrosion processes and formation of through defects that prevents destruction by the mechanism of low-cycle fatigue. It is shown that tensile and yield strength of steel correspond to the minimum normalized values. The reduction in plasticity of the feeding pipeline metal does not exceed 10 %, while that for return pipeline is below the minimum normalized value which is probably due to strain aging. The least damaged layer adjacent to the inner surface of pipes has increased strength and plasticity characteristics due to the pipe manufacturing technology. While hydraulic test may not lead to the expected destruction at the location of through defects, its probability raises with increase of the test pressure.

KEYWORDS: heat pipelines, corrosion, mechanical properties, hardness, through defects

INTRODUCTION

Reliable operation of heat pipelines is vital for public safety, environmental protection and economic stability. The processes of general and local corrosion are among main factors of reducing the operational stability of pipelines of heat networks, strain aging, as well as deterioration of mechanical characteristics and resistance of metal to destruction. Corrosion leads to decrease in thickness of the pipe wall, origin of stress concentrators, decline in resistance to crack initiation and propagation, which can cause pipeline destruction at operation and test pressure [1, 2].

The real mechanical properties of the metal of the pipelines after long-term operation are necessary to assess their actual strength, residual life and investigation into the causes of failure. Experimental determination of the mechanical properties of pipe steels 19G and 17G1C after long operation in gas and oil pipelines revealed their minor changes [3]. At the same time, the question of the influence of long-term operation on the mechanical properties of structural materials of heat pipelines subjected to specific loads and impact of external and internal environment remains studied insufficiently. A characteristic feature of the pipelines of the heat network after long operation is the presence of local corrosion thinning, which is quite large in area and can eventually devolve into the category of critically thinned areas — where plas-

tic deformations are observed at the hydraulic test pressure and below. Publications [4, 5] show the results of laboratory modeling of the heat pipeline operation. The obtained data on corrosion-mechanical properties made it possible to substantiate the low-cycle destruction of critically thinned areas and to provide recommendations on the pressure of periodic hydraulic tests of heat pipelines. Metal properties of areas thinned under operating conditions are one of the necessary components for determining their real state, and therefore their research is an actual task.

OBJECT OF RESEARCH

For conducting research were used two significantly corroded fragments, each ~2 m length, cut from feeding and return pipelines of the D325 main heating line laid in non-passable channel (Figure 1). Both fragments according to the results of periodic hydraulic test were recognized by the operating organization — KP Kyivteploenergo as unfit for further operation and transferred to PWI.

According to the technical documentation, the main heating line with design parameters of temperature $T_d = 150$ °C and internal pressure $P_d = 1.6$ MPa was installed in 1976 using electrically welded heat-treated pipes 325×8 (external diameter × wall thickness, mm) manufactured from steel BSt3sp [6] (Tables 1–3) and covered with bitumen-pearlite insulation.

Figure 1. Feeding and return pipelines in a non-passable channel (*a*); through corrosion defects in the feeding pipeline (*b*)

Table 1. Chemical composition of the pipe metal

Source	Mass fraction of elements, %									
	C	Mn	Si	S	P	Cr	Ni	Cu	As	Mo
[5]	0.14–0.22[**]	0.40–0.65	0.12–0.30	<0.055	<0.045	<0.30	<0.30	<0.30	<0.08	–
Feeding pipe[*]	0.11	0.46	0.22	0.015	0.011	0.09	0.08	0.086	–	0.009
Return pipe[*]	0.11	0.47	0.22	0.018	0.012	0.09	0.08	0.090	–	0.009
[*]Results of spectral analysis of metal. [**]Deviation from the lower limit of carbon content according to [6] is not a rejection sign.										

For further investigation of the metal properties were selected the blanks from the thinnest parts of the feeding pipe (Table 3).

RESEARCH METHODS

CORROSION STATE

Visual control of the pipeline fragments was carried out according to [8], their corrosion condition was assessed according to [9].

Energy dispersive spectroscopy (EDS) microanalysis of oxide layer was conducted using scanning electron microscope Philips XL30 with EDAX Sapphire detector unit.

Experimental setup for investigation of influence of inner pressure on external corrosion included (Figure 2):

● blank No. 4 (Table 3);

● electrochemical cell made of acrylic glass tube glued to specimen surface (corresponding to pipe external surface) with acidfree silicone rubber glue in area with low number of visible defects in the oxide layer (as checked out under a microscope);

● electrolyte — $NaHCO_3$ solution prepared from deionized water with 500 mg/L HCO_3^-, chosen due to its relatively inert behavior in the corrosion of steel (not aggressive, not strongly inhibiting) and pH buffering effect, thus minimizing fluctuations in open circuit potential;

● silver-silver chloride electrode (SSE) reference electrode for continuous open circuit potential (OCP) measurement.

Continuous OCP measurement was used to detect the formation of cracks in the oxide layer during elongation test in steps of 200 N with a traverse speed of 0.1 mm/min and 2 min holding time. Stepwise elongation was performed to give OCP time of equilibration.

Table 2. Mechanical properties of pipes according to the certificate[*]

Source	σ_t^{wm}, MPa	σ_t, MPa	σ_{02}, MPa	δ, %
Certificate	438–465	441–456	–	32–38
[6]	–	372–480	245	26
[7]	>372	>372	>225	>22
[*]σ_t^{wm} — tensile strength of the of the welded joint metal; σ_t/σ_{02} — yield strength/conditional yield strength of the base metal; δ — relative elongation.				

Table 3. Thickness of blanks

Nos	Minimum thickness (mm) of the left/right side edge of the blank	
1	0.9/1.3	
2	0.8/0.9	
3	0.5/1.3	
4	1.1/1.7	
5	1.5/1.7	
6	0.9/1.3	

Figure 2. Corrosion experimental setup: *a* — *1* — blank No. 4; *2* — electrochemical cell filled with solution and SSE reference electrode; *3* — tensile machine traverse; *b* — *A* — enlarged

MECHANICAL PROPERTIES OF THE METAL OF THE ZONE WITH MINOR CORROSION DAMAGE

To study the mechanical properties of the metal (σ_t; $\sigma_{0.2}$, δ_5, ψ — relative narrowing of the cross-section) flat proportional samples $l_0 = 5.65\sqrt{F_0}$ with a thickness of 3 mm and width of the working part of 8 mm were made with mechanical processing of both surfaces in the thickness direction (Figure 3). The samples were cut out from the pipes in the circumferential and longitudinal directions. The places for the grips of circumferential samples before milling were straightened in the press in such way as not to deform the working part.

Mechanical tests were performed on the test machine MTS-318.25 with deformation rate 2 mm/min at temperature of ~22 °C, extensometer gauge length 25 mm, survey interval 0.1 s.

MECHANICAL PROPERTIES OF THE METAL OF THE MOST THINNED ZONE OF THE FEEDING PIPELINE

Tensile test of sample No. 3 (Figure 4, *a*) made from blank No. 3 (see Table 3) was performed on Zwick Z050 testing machine according to [10] with a deformation rate of 1.25 mm/min at temperature ~23 °C, extensometer gauge length 40 mm, the survey inter-

val 0.02 s. Mechanical properties metal (σ_t, σ_{02}, δ_5, ψ) were determined on the base of test results.

Tensile testing of samples (Figure 4, *b*) made from blank No. 1 (see Table 3) was carried out at a constant room temperature using a dilatometer. For definition of tensile strength σ_t and yield strength σ_{02} of the material were used shorter samples, which made it possible to optimize the volume of mechanical processing.

LOW FORCE HV HARDNESS

Vickers hardness measurements *HV*1, *HV*0.3 were carried out according to [11] using hardness tester EMCO Test M1C 010 and CARL ZEISS Axio Imager.M2m microscope.

GRAIN SIZE

The grain size of ferrite and pearlite in the hardness measurement area was defined using CARL ZEISS Axio Imager.M2m microscope at magnification 500:1 according to [12].

RESULTS OF EXPERIMENTS AND THEIR ANALYSIS

The results of visual inspection proved that both pipes: feeding and return are single-seam, welded

Figure 3. Sample for tensile tests: l_e — extensometer gauge length; l_0 — original gauge length; F_0 — original cross-sectional area

Figure 4. A sample for tensile testing of the metal of the thinnest zone: *a* — on a tensile machine; *b* — on the dilatometer; l_e — extensometer gauge length

with high-frequency currents. At the time of inspection protective cover is practically absent. The outer surface of both pipes is covered with a layer of brown corrosion products, there are remnants of a protective coating, probably bituminous. Local corrosion damage detected on the surface of the pipes identified according to [9] as corrosion spots and pits of various sizes. The inner surface is covered with a layer of brown corrosion products that are easily separated from the pipe wall and fall apart. Corrosion of the inner surface is continuous and uniform. The corrosion state of the pipe fragments is unsatisfactory, while the corrosion damage of the feeding pipe is more significant. The thickness of the wall of the feeding pipe is unevenly reduced, probably due to corrosion, in the range from 7–8 to 1–2 mm; the thickness of the remains of the protective cover is 280–470 μm. Visually, the pits on the outer surface have a greater depth than on the inner surface — it should be assumed that the outer corrosion is more intense than the inner one. Corrosion pits on the outer surface vary in size: from 3×3 mm to 25×50 mm; in the region of the smallest wall thickness three through corrosion defects with dimensions of ~7×5, 6×5 and 13×7 mm were found (see Figure 1, b). Corrosion destruction probably started from side of the outer surface. Wall thickness of the return pipe varies from 7–8 mm to 3–4 mm, the thickness of the remains of protective cover is 0.25–6.7 mm.

Figure 5 shows the results of EDS microanalysis of the oxide layer of the feeding pipeline. As can be seen, the main component of the layer is iron, presumably in the form of FeO and Fe_2O_3 oxides, which were formed as a result of the electrochemical reaction between iron and water.

The potential of the open circuit turned out to be quite sensitive to the cracking of the protective layer. During the entire tensile time of the sample, a potential shift from –0.527 to –0.565 V, which indicated the loss of the protective properties of the oxide layer, presumably due to cracking and peeling. Under elastic deformation by tensile force in range $0 < S < 1200$ N (taking into account the thickness of the cross-section of the blank at the location of the electrochemical cell ~2 mm this corresponds to the pressure $0 < P < 0.5$ MPa in the pipeline D325) the potential almost did not change and reached –0.523 V. Further increase of tensile force up to 3000 N caused decease of OCP by about 5–7 mV, but with an increase in the force from 3000 to 4000 N, a sharp shift of the potential from –0.530 to –0.555 V was noted, which is due to the formation of areas of freshly exposed metal.

A synopsis of force and OCP over time (Figure 6) shows that there is a critical elastic load $S \sim 3000$ N (corresponding to an internal pressure $P \approx 1.3$ MPa),
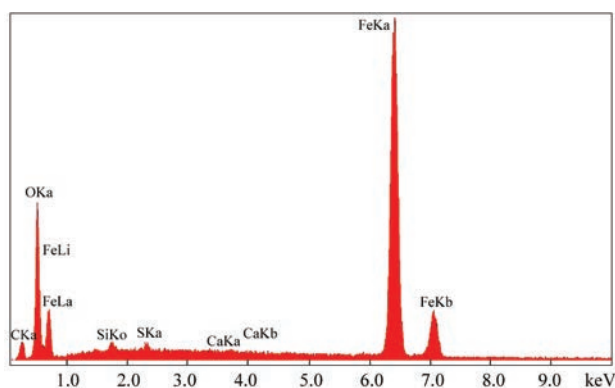
Figure 5. EDS spectrum of the oxide layer on the surface of feeding pipe

where the OCP rapidly decreases with each subsequent increase in tension. This indicates the beginning of the formation of deep cracks in the oxide layer, which significantly activate local corrosion processes.

The synopsis of force and OCP over time (Figure 6) reveals that there is a critical elastic load $S \sim 3000$ N (which corresponds to the internal pressure $P \approx 1.3$ MPa in the D325 pipeline with a thickness of $a = 2$ mm in the thinning zone), where OCP decreases rapidly and instantaneously with each further step in force. This indicates the onset of formation of deep cracks in the oxide layer, activating corrosion processes to a significant degree.

However, OCP provides no quantitative information on the corrosion processes induced by such cracking. On the other hand, the true quantitative effect in practice is hardly accessible by laboratory experiments as it depends on a large number of parameters occurring in the real environment (presence of humidity or liquid water, chemical composition of the water, possible galvanic effects in the system, wet-dry-cycles, etc.).

The results of visual inspection and OCP measurements satisfactory agree with the data of corrosion-mechanical tests of 17G1S steel from D630 pipe [5], according to which:

Figure 6. Change in the potential of the open circuit (1) of the sample under applied tensile force (2)

Figure 7. Tensile (σ_t) and yielding (σ_{02}) strength of metal of feeding and return pipes; upper indexes: a — axial direction; c — circumferential direction. 1 — certificate data; 2 — range of values; $3, 4$ — minimal values of σ_t, σ_{02} according to [7], correspondingly

Figure 8. Elongation after fracture δ_5 of metal of feeding and return pipes; upper indexes: a — axial direction; c — circumferential direction. 1 — certificate data; 2 — range of values; 3 — minimal value of δ_5 according to [7]
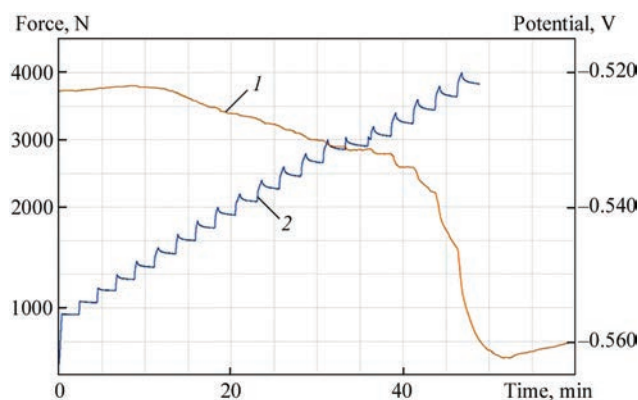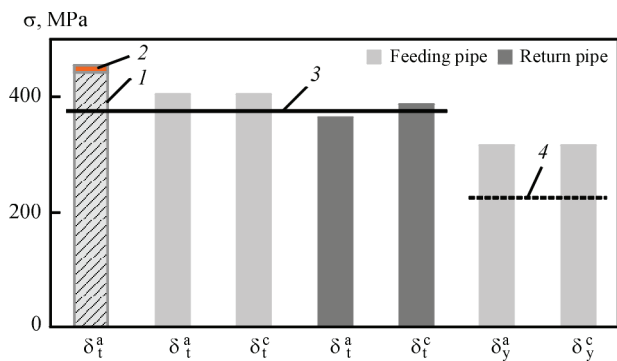
● at temperature of 80 °C (average operating temperature of feeding heat pipeline) the corrosion rate is twice higher than at a temperature of 40 °C (average operating temperature of a return pipeline);

● the corrosion process is accelerated as the working pressure increases (the internal pressure in feeding pipeline is ~2 times higher than in a return pipeline) and becomes more substantial when the stresses periodically attain the level corresponding to the pressure of hydraulic tests ($P = 2$ MPa).

Comparing of the results of tensile tests with the data of the certificate (Figures 7, 8) shows that after long-term operation (more than 40 years), the value of tensile strength in the axial direction σ_t^a of material of feeding pipeline decreased by ≈10 % and return pipeline by ≈18 %. Strength characteristics σ_t and σ_{02} of metal of feeding and return pipelines in circumferential and axial directions are practically the same and meet the minimum requirements of regulatory documentation, that generally agrees with the results [4] obtained in the absence of residual deformation. Reduction in plasticity of material of feeding pipeline in circular and axial direction does not exceed 10% and meets requirements [7]. Decrease in plasticity of material of return pipeline is more significant, especially in longitudinal direction, where it is lower than the
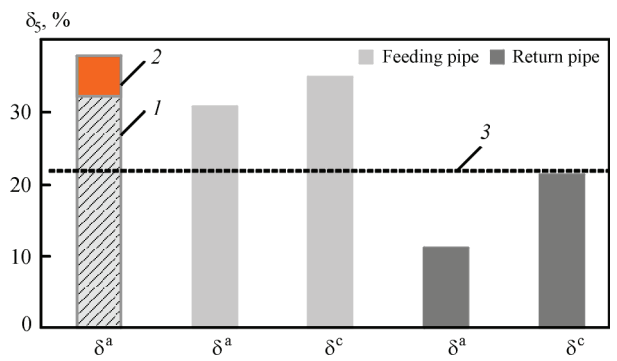
minimum regulatory value by ≈50 % which is probably a consequence of strain aging in the conditions of local bending of the pipeline and increases the susceptibility to brittle failure, including under explosive loading.

Results of tensile tests on material of feeding pipeline are given in Table 4 and Figure 9.

The increased strength and plasticity characteristics of the material of the significantly thinned zone of the pipe are explained by selection of samples No. 3, D1-1, D1-2 for tensile tests from the least damaged layer adjacent to the inner surface of the pipe, the properties of which are specific due to the pipe manufacturing technology, as well as the influence of scale factor (the thickness of the samples differs by ~6 times).

The trends of hardness change across thickness of blanks Nos 4 and 6 (Figure 10, c) agree with the results (Table 4.) The increase in hardness near the inner surface of the pipe indicates technological strengthening of the metal during the pipe manufacturing process, as well as the insignificance of internal corrosion. The hardened near-surface layer on the outside, apparently due to more intense corrosion, was not preserved.

Stated above can be confirmed also by the results of grain size measurements (Figure 11). The average grain size near the inner surface of the pipe is ≈2 (blank No. 6)

Table 4. Mechanical properties of material of feeding pipeline in axial direction

Specimen No.	1	3	D1-1	D1-2
Test machine	MTS	Zwick	Dilatometer	
Location	Minor corrosion	Significant corrosion thinning		
σ_t, MPa	408.0	442.1	449.7	443.7
σ_{02} MPa	320.0	333.1	338.3	333.2
δ_5, %	30.8 ($l_e = 25$ mm)	23.70 ($l_e = 40$ mm)/37.8*	–	–
ψ, %	56.4	73.8	–	–

*Value of relative elongation $\delta_5 = 37.8$ % of the non-proportional sample 3 was calculated according to [13] for comparison with the relative elongation of the proportional sample 1.
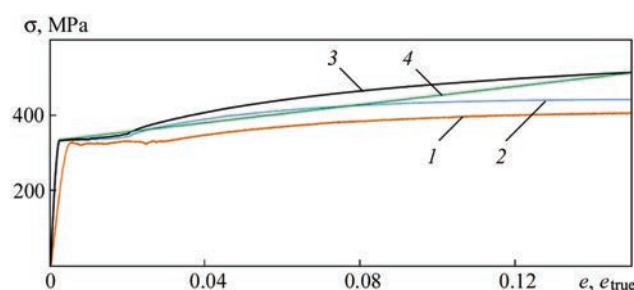
Figure 9. Tensile stress diagrams of samples Nos 1 and 3 within the limits of uniform thinning; *1* — specimen No. 1, regular diagram ($e = \Delta l_e / l_e$ (l_e — initial calculated length according to the strain gauge, Δl_e — elongation of initial calculated length according to the strain gauge), $\sigma = S/F_0$, (S — tensile force; F_0 — area of specimen cross-section); *2* — specimen No. 3, regular diagram; *3* — true stress-strain diagram of specimen No. 3 ($e_{true} = \ln(1 + e)$; $\sigma_{true} = \sigma(1 + e)$); *4* — approximated bilinear hardening diagram of specimen No. 3

and 10 % (blank No. 4) smaller than in the middle part of the cross-section across the thickness.

In Figure 12 are shown the results of hardness measurements in the zone of significant thinning of No. 4 blank, performed on the side face (in the direction of maximum tensile stresses caused by internal pressure). Despite the fact that the minimum thinning thickness $a_{min} = 0.68$ mm is significantly lower than the threshold value of the thickness $a_{max}^{CTA} = 0.97$ mm, which is calculated by substituting the mechanical properties of sample No. 1 (Table 4) in (1) and determines the beginning of the plastic deformation of

the pipeline wall at the pressure of hydraulic tests $P = 2$ MPa:

$$a_{max}^{CTA} = \frac{PD_0}{2\left(\sigma_{02} + \dfrac{P}{2}\right)} \tag{1}$$

the obtained values are practically the same in the middle of the thickness and in the near-surface layers of the metal. This indicates the absence, as a result of intensive corrosion of the original technologically strengthened layers of the outer and inner surfaces, as well as the absence of accumulated residual deformations, which is confirmed by FEA calculations and measurements of the hardness on the side surface of the sample after tensile test.

The dimensions of a fragment of the longitudinal section of the supply pipeline D325 were used to construct the geometric model of the pipeline (Figure 12, *a*). Modeling of defects on the surface of the pipe was carried out by rotating the corresponding complementary segments around the axes located coaxially with the pipe (Figure 13). The thickness of the pipe $a = 2$ mm approximately corresponds, according to visual inspection, to the average value of the wall thickness of adjacent sections in the area where the specified fragment of the longitudinal section is located. The true tensile diagram of sample No. 3 (Figure 9), approximated by the bilinear method
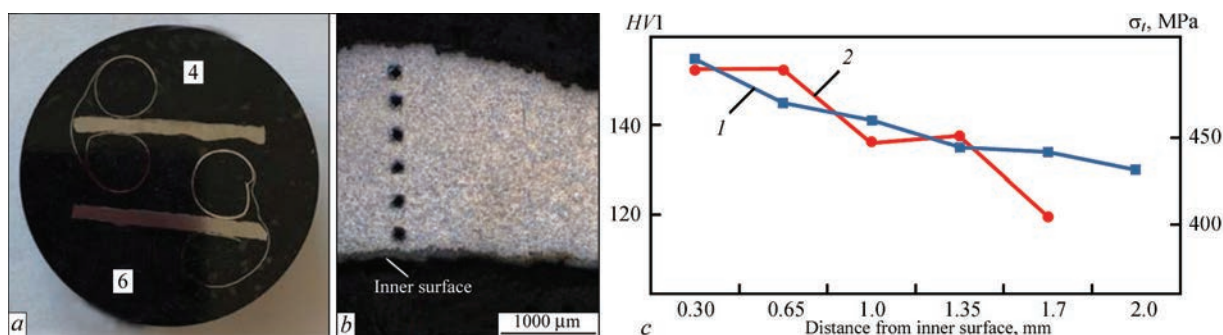
Figure 10. Measurement of hardness along the wall thickness of a pipe with significant corrosion thinning: *a* — measurement template, the numbers indicate the blank numbers (see Table 3); *b* — specimen from blank No. 4 after indentation; *c* — hardness *HV*1 and tensile strength σ_t across the thickness of the specimens No. 4 (*1*) and No. 6 (*2*); calculation of σ_t values according to [11]

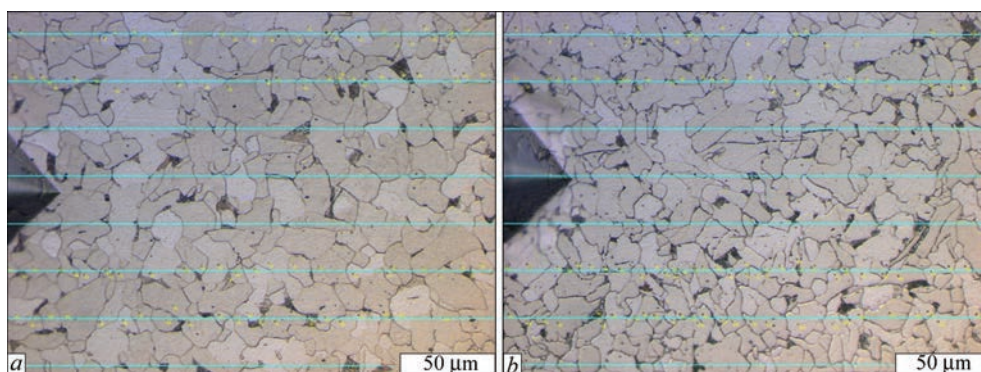**Figure 11.** Measurement of grain size of sample No. 4 at the: *a* — middle of wall thickness; *b* — near the inner surface
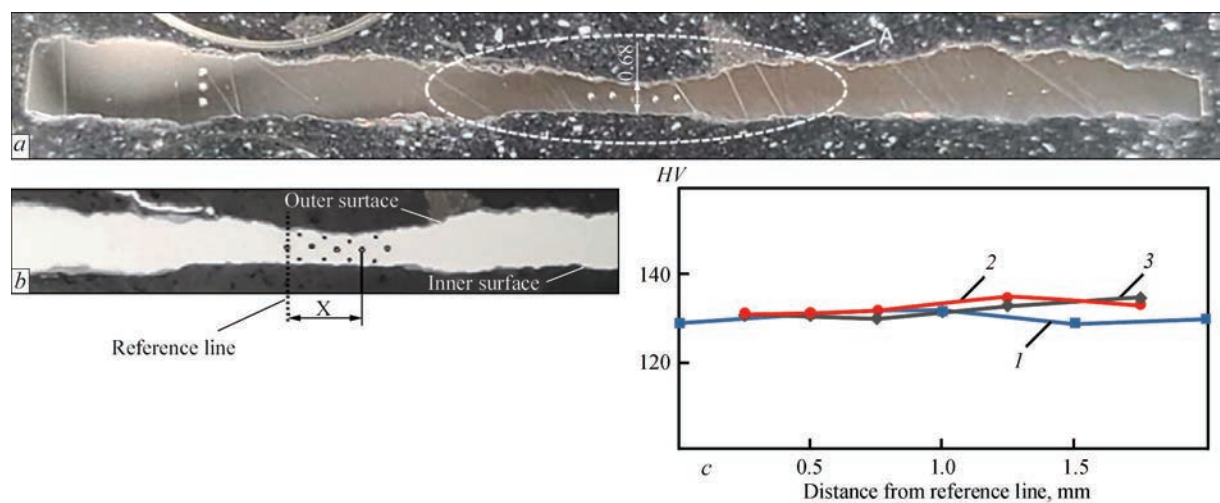
Figure 12. Measurement of hardness along the thickness of a significantly thinned wall: *a* — template after *HV*1 measurements; *b* — zone A after *HV*1 and *HV*0.3 measurements; × — distance from the reference line to the measurement point; *c* — hardness along wall thickness: *1* — middle of the thickness, *2* — outer surface; *3* — inner surface
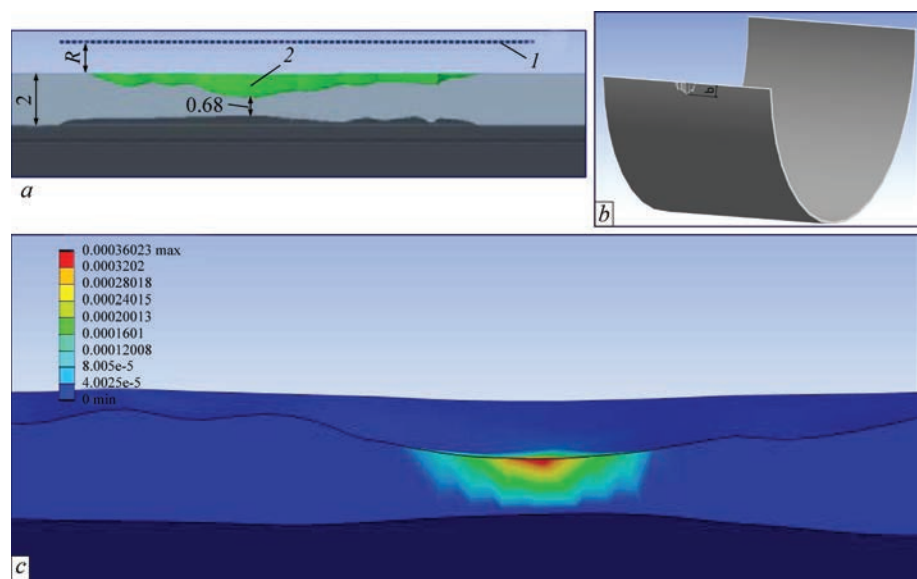
Figure 13. Model defect: *a* — application scheme: *1* — axis of rotation; *2* — complementary segment, *R* — radius of rotation; *b* — defect on outer surface (*b* — half width of defect); *3* — distribution of plastic strains

(σ_{02} = 334 MPa, σ_t = 516 MPa, tangential modulus G_t = 1200 MPa), was used in the calculation. Table 5 presents the maximum plastic deformations of three defects with different geometric parameters under the hydraulic test pressure P = 2 MPa. Relatively low values of the maximum deformations on the outer surface in the zone of greatest thinning are a consequence of unloading bending caused by the action of internal pressure.

The results of Vickers hardness measurement under a load of 0.3 kg (*HV*0.3) on the side surface of

sample D1-1 after its tensile test are shown in Figure 14.

The approximate value of residual plastic deformation e_r at the *i*-th point of hardness measurement was determined as

$$e_{ri} \approx \ln\left(\frac{a_0}{a_i}\right),$$

where a_0 — initial thickness of the cross-section of the sample; a_i — thickness of the cross-section of the sample at the *i*-th point after testing.

The given data (Figure 14, *c*) confirm that the values of the maximum plastic deformations e_r < 0.1 % of the template with the minimum thickness a_{min} = 0.68 mm do not significantly affect the hardness.

Table 5. Maximal plastic strain *e* in defect

Variant No.	Radius R, mm	Width b, mm	$e \cdot 10^{-2}$, %
1	3	2.5	0.07
2	50	8.2	4
3	100	11.4	10

26
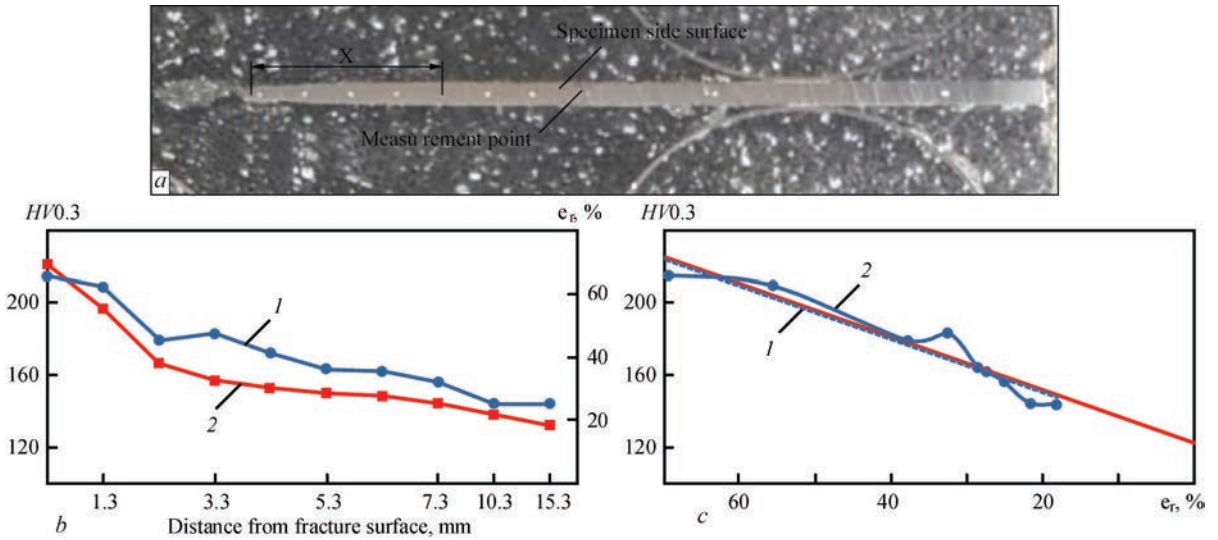
Figure 14. Hardness along the length of the side surface of sample D1-1 after tensile testing: *a* — side surface of the sample; × — the distance of the measurement point from the fracture surface; *b* — results of hardness measurement (*1*) as a function of the distance from the fracture surface and residual plastic deformation e_r (*2*); *c* — linear approximation of hardness values *HV* (*1*) depending on residual deformation e_r (*2*)

Further decrease in the thickness of the pipe and wall can lead to an increase in the rate of corrosion due to an increment in the operating stresses and residual plastic deformation. At the same time, under the influence of variable operating loads, accumulated low-cycle damage occurs in the surface layer of the most thinned areas and corrosion pits [4]. The presence of through corrosion defects indicates that, due to the fast development of wall corrosion, accumulated fatigue damage in the constantly renewed surface layer does not have time to reach a critical value.

Evaluation of the strength in the presence of through-hole defects, can be done using hypothesis according to which the bearing capacity of the pipeline will decrease if:

$$A_d > A_0,$$

where A_d — the longitude cross-sectional area of the weakening caused by defect; A_0 — longitudinal cross-sectional area of the maximum round hole, which does not reduce bearing capacity of the pipeline.

According to [14] for pipe 325×8:

$$A_0 = d_0^{P_b} a = 100.8 \text{ mm}^2,$$

where $d_0^{P_b}$ — max diameter of the round hole at burst pressure P_b of the pipe:

$$d_0^{P_b} = 0.25\sqrt{D_m a},$$

where D_m — average diameter of the pipe; a — nominal pipe thickness.

For assessment of strength of the considered fragment of feeding pipeline let's schematize through de-

Figure 15. Schematization of through hole defects: *a* — top view: d_1, d_2 — diameters of defects circumscribing holes; *b* — calculation scheme: a_{HT} — minimal allowable thickness under pressure P; l_w — length of adjacent weakened zone; a_{min} — minimal remain thickness; A_{WC} — calculated area of adjacent weakened zone; A_h — area of schematized hole; ΔA_{WC} — increase of weakened area

fects by circumscribing holes with diameter d_1 and d_2 (Figure 15, *a*). As far as (Figure15, *b*):
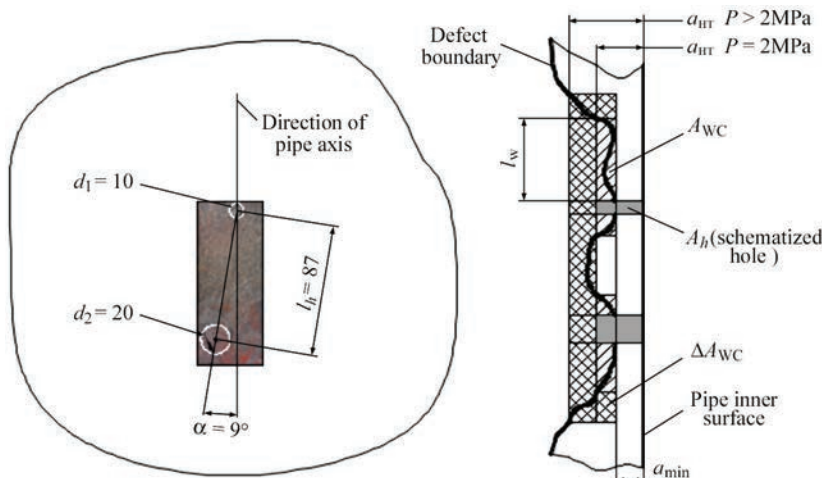
$$l_d < 2\sqrt{D_m a} \text{ and } \alpha < 15°$$

we will consider these holes as lying in the same cross-section and belonging to the same defect of complex shape. Since no destruction occurred during the hydraulic test ($P = 2$ MPa), it can be stated in relation to the specified defect that:

$$A_d = \sum A_h + \sum A_{WC} < A_0,$$

where A_h — area of schematized hole:

$$A_h = da_{HT},$$

where d — diameter of circumscribing hole; a_{HT} — minimal allowable thickness during hydraulic test according to (1); A_{WC} — calculated area of longitudinal cross-section of adjacent to hole zone with remaining thickness less then a_{HT}:

$$A_{WC} = \left(a_{HT}^P - a_{min}\right)l_W,$$

where a_{min} — minimal remain thickness of defect excluding through holes; l_W — length of longitudinal cross-section of adjacent to hole zone with remaining thickness less than a_{HT}.

Thus, hydraulic test does not guarantee planned destruction of the pipeline in the presence of relatively small through defects. Accordingly, the insignificant leakage of water caused by them, makes it difficult their detection, especially when pipeline lays in an impassable channel.

It should be noted that at the time of conducting hydraulic test information on the presence of through defects and their characteristic geometric parameters, as a rule, is not available, therefore preliminary determination of the destructive pressure of the damaged pipeline is impossible. At the same time with an increase of the test pressure the probability of failure of pipeline with through defects become large due the raising of weakened area ΔA_{WC} (Figure15, *b*).

CONCLUSIONS

Based on the conducted research, it was established that after long-term operation of the heat pipeline:

● Corrosion state of the heat pipelines is unsatisfactory. The protective coating does not meet the requirements of regulatory documents in terms of physical and mechanical indicators. The damage of the feeding pipeline, which was subjected to more significant operational loads, is more severe than that of the return pipeline, while the external corrosion of the pipelines is more intense than the internal one.

● Cracking of oxide layer, which begins in most thinned areas and in corrosion pits of feeding pipe-line, accelerates with increasing stresses in the range of the design pressure, which leads to the activation of corrosion processes and formation of through defects that prevents destruction by the mechanism of low-cycle fatigue.

● Value of the tensile strength of the structural material (BSt3sp) of the feeding pipeline decreased by ≈10 %, return pipeline by ≈18 %. Tensile and yield strength of the pipeline material in the circumferential and axial direction are practically the same and correspond to the minimum normalized values. Reduction in plasticity of the material of feeding pipeline does not exceed 10 %, while that for return pipeline is more significant, especially in the axial direction, where it is below the minimum normalized value which is probably due to strain aging and increases the tendency to brittle failure.

● Increased strength and plasticity characteristics of the material of significantly thinned areas are caused by the selection of tensile samples from least damaged layer adjacent to original inner surface, the properties of which are specific due to the pipe manufacturing technology, as well as influence on results of the scale factor of used for comparison specimens.

● Hydraulic test may not lead to expected destruction at the location of through defects, depending on the geometric parameters of damage, which, given relatively small size of defects and accordingly insignificant leakage of water, makes it difficult to detect them when pipeline lays in an impassable channel.

REFERENCES

1. Torop, V.M. (2022) Conducting hydraulic tests of pipelines of heat networks in order to achieve the specified reliability of their operation. *Tekh. Diahnost. ta Neruiniv. Kontrol*, **3**, 35–41 [in Ukrainian].

2. Pleshivtsev, V.G., Pak, Yu.A., Pak, Yu.A., Filippov, G.A. (2008) Factors that reduce the structural strength of pipe metal and the prospects for creating new pipe steels for heating networks. In: *Proc. of 3rd Sci.-Pract. Conf. on Heat Networks. Modern Practical Solutions* [in Russian]. www.rosteplo.ru/Tech_stat/stat_shablon.php?id=2076pov

3. Penkin, A.G., Terentyev, V.F., Maslov, L.G. (2004) *Assessment of the degree of degradation of mechanical properties and residual service life of pipe steels using acoustic emission and kinetic hardness methods* [in Russian]. //www.sds.ru/articles/degradation/index.html

4. Yukhymets, P.S., Dmytryenko, R.I., Palienko, O.L., Yegorenko, V.M. (2022) Mechanical properties of the metal of critically thinned sections of the heat pipe and features of their destruction. *Tekh. Diahnost. ta Neruiniv. Kontrol*, **4**, 34–46 [in Ukrainian].

5. Yukhymets, P.S., Nyrkova, L.I., Gopkalo, O.P. (2022) Specific features of corrosion heating network pipelines made of 17G1S steel. *Materials Sci.*, 58(**1**), 35–40.

6. (2005) GOST 380: *Carbon steel of ordinary quality. Brands.*

7. (1980) GOST 10705: *Electric-welded steel pipes. Technical Conditions.*

8. (2005) DSTU EN 13018: *Non-destructive testing. Visual control. General requirements.*

9. (1985) GOST 9.908: *Unified system of protection against corrosion and aging. Metals and alloys. Methods of determining corrosion indicators and corrosion resistance.*
10. (2009) DIN EN ISO 6892-1: *Metallic materials — Tensile testing — Pt 1: Method of test at room temperature.*
11. (2018) ISO 6507-1: *Metallic material. Vickers hardness test. Pt 1: Test method.*
12. (2024) ASTM E112: *Standard test methods for determining average grain size*.
13. (1999) EN ISO 2566-1: *Conversion of elongation values. Pt 1: Carbon and low alloy steels.*
14. (1986) PNAE G-7-002: *Standards for calculation of strength of equipment and pipelines of nuclear power installations.*

ORCID

P. Yukhymets: 0000-0002-8824-9024,
L. Nyrkova: 0000-0003-3917-9063
R. Dmytriienko: 0000-0001-8842-5051
P. Linhardt: 0000-0002-4523-2185

CORRESPONDING AUTHOR

P. Yukhymets
E.O. Paton Electric Welding Institute of the NASU
11 Kazymyr Malevych Str., 03150, Kyiv, Ukraine.
E-mail: yupeter@ukr.net

EFFECTIVENESS OF THE TECHNOLOGY OF AUTOMATED EDDY CURRENT FLAW DETECTION WITH ARRAY PROBE

Iu.Yu. Lysenko[1], Yu.V. Kuts[1], Y. Mirchev[2], O.E. Levchenko[1], S.M. Glabets[1,3]

[1]National Technical University of Ukraine "Igor Sikorsky Kyiv Polytechnic Institute"
37 Prosp. Beresteiskyi, 03056, Kyiv, Ukraine
[2]Institute of Mechanics of Bulgarian Academy of Sciences
Acad. G. Bontchev St., bl. 4, 1113 Sofia, Bulgaria
[3]Laboratory of SC LLC "SPF "Diagnostychni Prylady"
103 Patriotiv Str., 03061, Kyiv, Ukraine

ABSTRACT

The effectiveness of application of matrix converter method at eddy current testing (ECT) is studied in the work. Advantages of eddy current matrix application are analyzed, which include improvement of sensitivity to small defects, shortening of the total control time and improvement of the probability of detection of various types of defects. To evaluate their effectiveness, a dimensionless coefficient is proposed, which takes into account the inspection time, the reliability of defect detection, and the sensitivity to defects of a certain size. Experimental studies on specimens with artificially induced defects of different dimensions, types and orientation confirmed the rationality of application of this coefficient for testing parameter optimization, in order to improve defect detection in structural elements. The influence of various factors, such as condition of the surface, sensor configuration in the matrix and verification parameters on the productivity of ECT hardware and software with matrix converters was additionally analyzed. Obtained results will promote better understanding of the possibilities and limitations of matrix application in ECT of the components of transport, aviation and defense equipment. It will allow optimizing the strategies of checking the tested products, improving the reliability of defect detection and general maintenance practices in many industries.

KEYWORDS: automated eddy current testing, converter matrix, effectiveness, mathematical modelling, flaw detection, signal processing, numerical methods

INTRODUCTION

The requirement of safety and reliability of operation in modern critical sectors of economy, such as aircraft, defense, automotive, oil and gas, and power generation prioritize effective checking and assessment of the current state of components. The need to detect defects in critical elements and components of structures for various purposes is the decisive factor to prevent irreversible failures and to ensure optimal operation of the system. New engineering solutions in the mentioned sectors and application of new materials increase the demand for advanced methods and procedures of nondestructive testing (NDT) and adaptation of the known methods to new NDT tasks [1–3].

Among the advanced directions of NDT development, the method of matrix eddy current testing (MEDT) is known by its numerous advantages, and it belongs to attractive solutions for detection of defects and evaluation of their characteristics in structural elements in different branches of the economy [4, 5]. MEDT application envisages using several closely located electric coils, combined into converter arrays, which promotes improvement of the coverage area of the tested object (TO) and increased sensitivity to small defects. Such an approach allows revealing anomalies, which may be undetected by single converters, and improves the overall effectiveness of TO diagnostics. At the same time, scanning by several channels and acquisition of a significant volume of data in one pass of the eddy current matrix (ECM) significantly shorten the testing time, which is extremely important at examination of large-sized TO, as it also shortens the equipment downtime during maintenance [6, 7].

MEDT capabilities include defect detection both on the surface and inside TO. This makes it more effective for detection of cracks, corrosion damage, delamination and other hidden defects, which can violate the structural integrity of structural elements. It is of special importance in the context of transport and defense industry, where reliability and safety are critical factors for life protection and preservation [5, 8].

Despite the fact that MEDT demonstrates considerable potential for application in different sectors, certain problems related to its introduction and optimization remain unsolved. ECM application allows obtaining information on the size, shape and orientation of the detected defects, based on the amplitude value of coil signals. However, complex interaction of factors, including the size of the converter array, its geometry,

material properties and testing parameters, requires a comprehensive evaluation of their influence [9].

Aggregate analysis of informative parameters of ECM signals, namely amplitude and phase of the harmonic signals, will allow more precise characterization of the defect nature and improvement of the reliability of decision taking in automated systems of eddy current flaw detection. More over, it is rational to process and analyze the considerable volumes of measurement information obtained using ECM in the form of digital data, using advanced information technologies, including artificial intelligence, that may improve data analysis and interpretation, increasing the testing effectiveness and reliability [10, 11]. It will also allow quantitative evaluation of the defect characteristics and will facilitate taking substantiated decisions as to the strategies for the acceptability of further operation or restoration repair of critically important structural elements [12].

THE OBJECTIVE

of the work is to study the effectiveness of ECM technology in flaw detection, using the proposed dimensionless efficiency factor, which takes into account the checking time, reliability and sensitivity, as well as experimental testing of MEDT technology on material with artificial defects with the known characteristics.

THEORETICAL SUBSTANTIATION OF ECM EFFICIENCY FACTOR

Analysis of the advantages of ECM application showed that, compared to the traditional converters this methodology ensures a higher sensitivity to small defect detection, reduction of the overall control time and increased probability of detection of various defect types [13, 14]. In view of that, it was proposed to assess the effectiveness of ECM application in flaw detection by a dimensionless coefficient, which is found from the following formula:

$$k_{ef} = k_t k_P k_S, \qquad (1)$$

where k_t, k_P, k_S are the relative coefficients characterizing reduction of testing time, increase of testing reliability and improvement of the testing device sensitivity, respectively. If evaluation of a specific defect parameter (for instance, its length, depth or crack depth) is performed alongside defect detection, coefficient (1) can be completed by a multiplier, characterizing the increase of the reliability of this parameter assessment.

The coefficient, which characterizes the reduction in inspection time, is determined by relative shortening of the time of TO examination by the following formula:

$$k_t = \frac{T_{ECC}}{T_{ECM}}, \qquad (2)$$
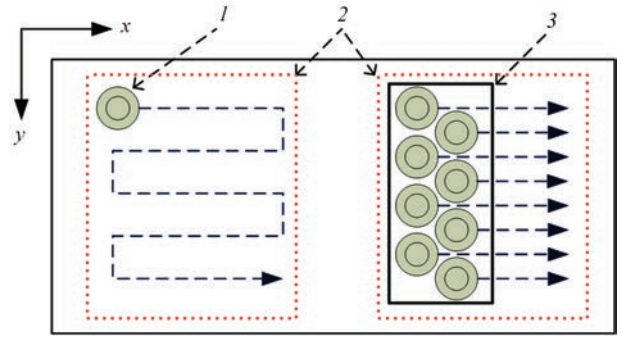
Figure 1. Trajectories of ECC and ECM scanning over TO surface: *1* — ECC; *2* — scanning area; *3* — ECM

where T_{ECC}, T_{ECM} is the total testing time, when using the traditional single eddy current converter (ECC) and ECM, respectively.

To assess the testing time, it is necessary to take into account the duration of movement by a single ECC and by ECM along the trajectory of TO surface scanning [8]. Let us assume that: 1) transverse size (along the *y* coordinate) of the tested area coincides with ECM transverse size, along which the sensors are located (Figure 1); 2) ECM moves only along *x* coordinate, while for covering such a TO surface area, it is necessary to move ECC both along *x* coordinate and along *y* coordinate. In this case, values of time intervals T_{ECC}, T_{ECM} are determined by the following expressions:

$$T_{ECC} = mn(t_r + t_m), \qquad (3)$$

$$T_{ECA} = mt_r + nmt_m, \qquad (4)$$

where t_r and t_m are the time required, respectively, for repositioning the ECC or ECA probe to the next measurement point and for performing a measurement at an one point; m, n is the number of measurement points on TO surface along *x* and *y* axes, respectively.

As in the accepted assumptions the number of ECC scanning lines is equal to the number of elements in the array (n), and $t_r \gg t_m$, then coefficient (2) can be approximately represented by the following expression:

$$k_t \approx n. \qquad (5)$$

The coefficient, which characterizes the improvement in inspection reliability, can be determined as the ratio of the probabilities of detection of defects of a certain type and size during application of ECC (P_{ECC}) and ECM (P_{ECM}) by the following formula:

$$k_P = \frac{P_{ECC}}{P_{ECA}}. \qquad (6)$$

It is rational to determine this coefficient experimentally, using test specimens with artificial or natural defects under the condition that the parameters of excitation of eddy current electromagnetic field and the gain factors of measurement channels are the same for ECC and ECM.

Figure 2. Specimen from AD31T5 alloy: 1–12 — defects of different types and dimensions

Coefficient k_S can be defined as the ratio of absolute sensitivities $S_{\text{ECC}}(l)$ and $S_{\text{ECM}}(l)$ at detection of a certain type of defect in the range of the change of its parameter size Δl by the following formula:

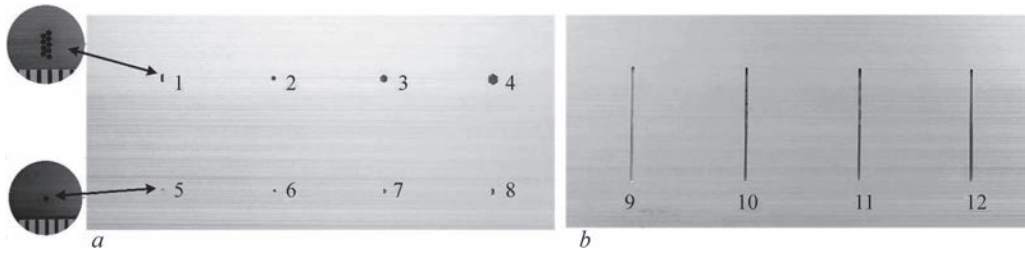$$k_S = \frac{S_{\text{ECM}}(\Delta l)}{S_{\text{ECC}}(\Delta l)}, \quad (7)$$

where parameter l is the specific parameter of the defect (length, depth of location, crack depth, etc.).

The latter coefficient should also be determined under the condition of similar for both the converters parameters of excitation of eddy current electromagnetic field and measurement channel gain factors. As an example, if the amplitude method of defect detection is used, and the test specimen has two defects of dimensions $l_1, l_2 \in \Delta l, l_1 < l_2$, and these defects generate in the converters the signals of amplitudes U_{ECM} (l_1), $U_{\text{ECM}}(l_2)$, and $U_{\text{ECC}}(l_1)$, $U_{\text{ECC}}(l_2)$, the converter sensitivities will be defined as follows:

$$S_{\text{ECM}}(\Delta l) = \frac{U_{\text{ECM}}(l_2) - U_{\text{ECM}}(l_1)}{l_2 - l_1};$$

$$S_{\text{ECC}}(\Delta l) = \frac{U_{\text{ECC}}(l_2) - U_{\text{ECC}}(l_1)}{l_2 - l_1}, \quad (8)$$
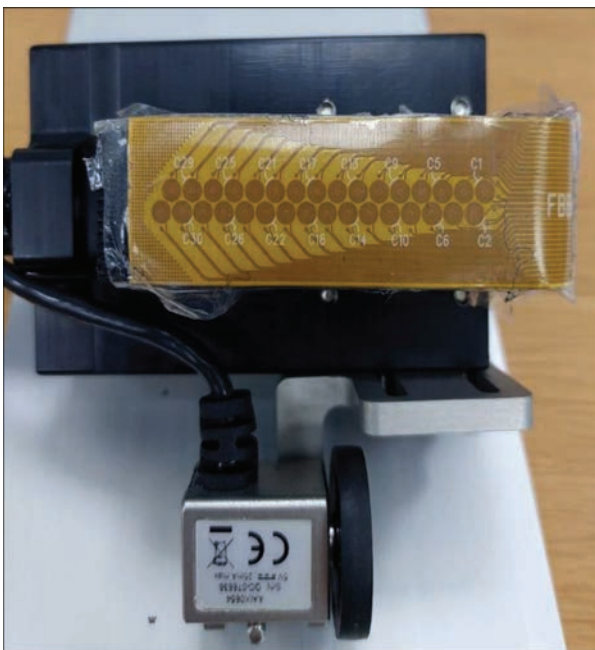
Figure 3. Eddy current matrix used in the experiments

and coefficient (7):

$$k_S = \frac{U_{\text{ECM}}(l_2) - U_{\text{ECM}}(l_1)}{U_{\text{ECC}}(l_2) - U_{\text{ECC}}(l_1)}, l_1, l_2 \in \Delta l. \quad (9)$$

Thus, a dimensionless coefficient was proposed for comprehensive assessment of the reduction of testing time, increase of testing validity and its sensitivity, which is quite suitable for determination of the effectiveness ECM application.

In case it is impossible to experimentally determine the coefficient components k_{p} and k_{S} they can be taken equal to a unity, and the approximate value of k_{ef} can be assessed as $k_{\text{ef}} \approx k_{\text{t}}$.

EXPERIMENTAL STUDIES

MATERIALS AND INSTRUMENTS USED

In order to conduct investigations, a specimen from aluminium alloy 31T5 (AD31T5), widely used in aircraft industry, was prepared. This specimen has artificially introduced defects of different configuration and size (Figure 2, a, b) and is of the following dimensions: 360 mm long, 120 mm wide and 5 mm thick. In the test specimen the longitudinal defects have the width of 1 mm and depth of 1–4 mm. In addition, the specimen surface has defects which are clusters of a different number of holes (Figure 2, a) and cracks of different depth (Figure 2, b). The holes have the depth of 4 mm and diameter of 0.5 mm each, and they are arranged in different numbers and in close proximity of each other. However, some dimensions of the thus formed defects can be too small for adequate testing with ECM used in the study.

In this investigation we used eddy current flaw detector Olympus Omniscan MX with ECM (Figure 3), which belongs to the category of flexible sensors and is made from film by the printed circuit board technology [15]. For adjustment to the examined surface, the sensor can be mounted on a base with the required curvature. ECM consists of 32 coils, each of 3 mm diameter.

The flaw detector implements multiplexing of individual matrix elements to prevent the mutual influence of adjacent elements, and its specialized software allows generating signal C-scans with simultaneous representation of the signals in the form of hodographs.

EXPERIMENTAL PROCEDURE
AND RESULT DISCUSSION

Scanning results in the form of C-scans of the studied specimen surface are shown in Figure 4 (for convenience, the scanning results are divided into three zones and defect numbering in keeping with Figure 2 is used). The following settings were used in the conducted experiment: working frequencies of 80, 160, 320 Hz, signal amplitude in the excitation coils of 1 V, signal amplification of 78 dB in the measurement channel.

The sensitivity level of 78 dB was selected for adequate interpretation and comparison of testing results, which satisfied (by the amplitude scale) all the TO scanning modes and provided clear visualization (visibility) of the defects. Higher sensitivity increases the risk of faulty operation because of a higher noise level and it may lead to the situation, when defects will be overlooked, while defectfree TO areas will be considered defective [16].

Quantitative assessment of defect parameters can be obtained by the signal amplitudes after ECM passing through a defective area. Obtained values of defect signal amplitudes are summarized in Table 1.

Figure 4, *a*, *b* shows the results of scanning TO areas with a different number of holes. Analysis of their scanning results shows that the highest sensitivity is achieved at the frequency of 320 Hz. However, if we take into account the relative position of the holes in one cluster (for instance, defects 2 and 8 have the same number of holes, but differ by their relative location), then the frequency of 80 Hz yields a difference in amplitude greater than 600 mV, but with frequency increase the influence of the geometry becomes less noticeable by amplitude. So, defect 2 is characterized by the same amplitude value at frequencies of 160 and 320 Hz.

The given data lead to the following conclusions. First, the signals from defects 9–12 differing by the artificial defect depths, practically do not differ by amplitudes at each of the frequencies. Such a result meets

the theoretical expectations, as the depth of eddy current penetration into aluminium at the frequency of 80 kHz is ~ 0.3 mm at the specific electrical conductivity of aluminium of ~ 36 MS/m, and the minimal depth of defects 9–12 is 1 mm. Secondly, for defects 1–8 (Figure 2) a certain dependence of defect signal amplitude on their dimensions and total area (shape) is observed.

For a more detailed analysis of this dependence, let us single out a subgroup of defects of one type in the form of an extended set of holes. Defects 1, 6, 7, 8 belong to this group. Values of signal amplitudes of these defects, arranged in the ascending order of defect size (or number of holes n) for different working frequencies are given in Table 2 and in Figure 5.

Analysis of the derived graphs leads to the following conclusions.

1. At less than 80 KHz working frequencies, the converter is capable of detecting defects smaller than

Table 1. Data of TO experimental study

Defect number	Defect parameter	Size, mm	Amplitude of signal from defect, V		
			80 kHz	160 kHz	320 kHz
1	Length	2.9	4.6	10.6	10.6
2		1.7	2.7	7.9	7.9
3		2.9	5.7	10.7	10.8
4		4.1	7.5	10.9	10.9
5		0.5	0.02	1.1	1.6
6		1.1	1.0	2.7	4.3
7		1.7	2.0	6.2	10.3
8		2.3	3.4	8.3	10.5
9	Depth	1.0	7.7	11.3	11.6
10		2.0	7.8	11.8	11.9
11		3.0	7.9	12.0	12.3
12		4.0	8.0	12.3	12.4
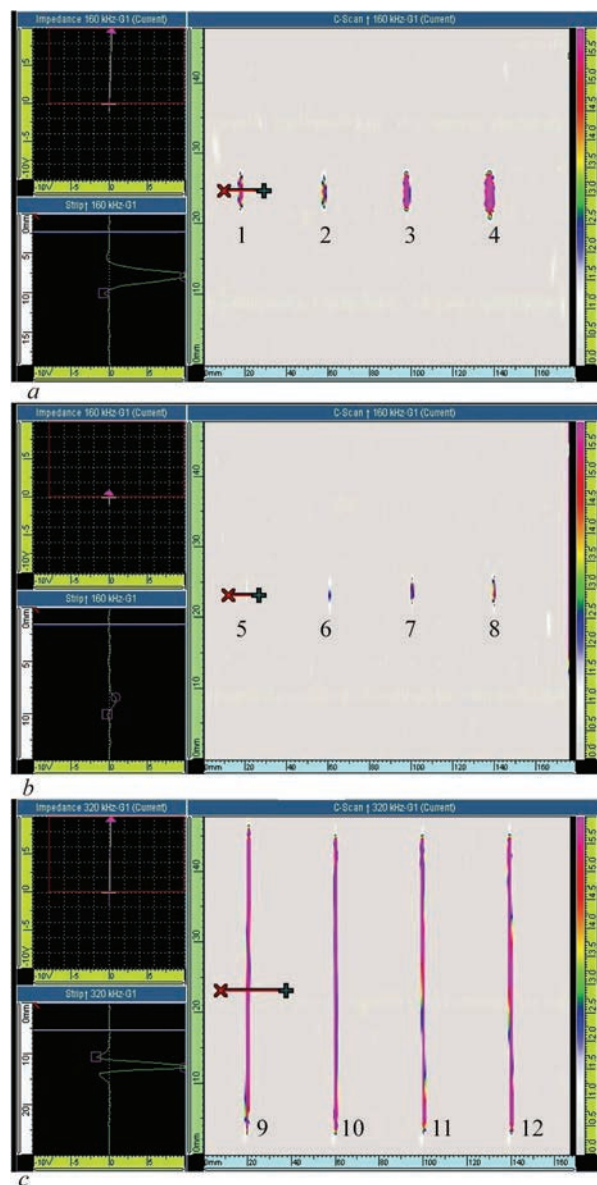
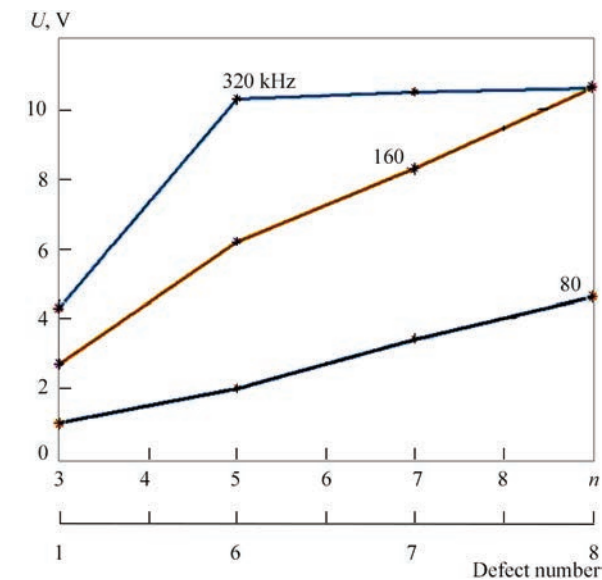**Figure 4.** Graphic representation of TO scanning results on the screen of Olympus Omniscan MX flaw detector

Figure 5. Graphs of dependence of amplitudes of signals from defects 1, 6, 7, 8 on their size and working frequency

Table 2. Experimental data on studying TO defects, arranged by defect size

Defect number	Number of holes n in the defect/defect length, mm	Amplitude of signal from defect at different working frequencies, V		
		80 kHz	160 kHz	320 kHz
6	3/1.1	1.0	2.7	4.3
7	5/1.7	2.0	6.2	10.3
8	7/2.3	3.4	8.3	10.5
1	9/2.9	4.6	10.6	10.6

the dimensions of ECM coils (coil diameter is 3 mm). For instance, a signal of not less than 1 V amplitude was received from defect 6 of ~ 1.1 mm length, which is indicative of the high sensitivity of the converter to small-sized defects.

2. Presented dependencies at frequencies of 80 and 160 kHz are close to the linear ones, giving grounds for their use for quantitative assessment of defect dimensions. However, a decision should be first taken on the defects belonging to a certain class, as different functional dependencies will be in place for different classes and frequencies.

3. Converter sensitivity is increased with increase of working frequency, but the range is reduced at the same time. For instance, at the frequency of 320 kHz this range is limited by the value of ~ 1.1 mm. However, there is a greater possibility of expanding it into the range of smaller defect dimensions.

Thus, for defects 1–8 there exists a certain dependence of signal amplitudes on their size and areas (shape of the hole set) (Figure 2, a). It is obvious that for a more detailed analysis of this dependence, it is necessary to single out a subgroup of defects, which are of the same type by the hole cluster shape. Defects 1, 6, 7 and 8 with the length of 2.9; 1.1; 1.7 and 2.3 mm along the vertical, respectively, should be included into this subgroup. Comparing the signal values for these defects, it is obvious that for defect 6 of ~ 1.1 mm length a signal with not less than 1 V amplitude was received, which is indicative of the high sensitivity of ECM to fine defects at the assigned scanning settings.

One can also see from Figure 4, b that the colour representation of defects 5 and 6 is the least noticeable at the above-mentioned scanning settings. Detection of defect 5, represented by one hole of 0.5 mm diameter is complex, without preliminary ECM setting up and cal-

ibration, which points to the need for a more thorough selection of the scanning mode for defects of this size.

Figure 4, c shows the results of scanning of a TO area with cracks of different depth. In keeping with the results (Table 1), the highest sensitivity was achieved at the frequency of 160 kHz. Proceeding from the experimental data, it can be assumed that increase of the crack depth by 0.1 mm will lead to a change in voltage by approximately 30–33 mV, which is suitable for measurement, taking into account the flaw detector capabilities.

The coefficient of effectiveness of ECM application provided $k_P \approx k_S \approx 1$ is determined by a gain in reducing the time of obtaining measurement information: $k_{ef} \approx k_t = n = 32$.

On the whole, the conducted experiment results confirmed the high productivity and effectiveness of eddy current flaw detection (ECFD) technology based on application of ECM and at the same time they allowed revealing the limitations and weak points of this technology that requires further investigation, in order to determine the optimal operating modes of such converters in different ECFD tasks and to conduct process automation.

CONCLUSIONS

This study emphasizes the key role of ECM technology to control products from electrically conducting materials in many industries. During investigations the attention was focused on testing reliability and sensitivity, as well as evaluation of ECM productivity at defect detection. A dimensionless coefficient was proposed, which allows assessment of the improvement of testing reliability and sensitivity, as well as relative reduction of the time of object testing that is acceptable for determination of the effectiveness of ECM application.

Experimental data derived on TO with defects of different types, dimensions and orientations, revealed significant ECM advantages for eddy current flaw detection. Use of several closely located coils improved the coverage and sensitivity to small-sized defects during their detection, which could be missed in the case of application of flaw detectors with the traditional single-element ECC. TO scanning and data acquisition in one ECC passage from a considerable area of its surface enabled reducing the control time and simplifying the mechanical part of the means of automated eddy

current testing that is essential in the case of examination of objects of considerable dimensions.

Improvement of the technology of ECT with ECM application enables expansion of functional capabilities of this kind of control and improvement of technical characteristics of control means that will promote increase of safety and reliability of operation of critically important structures and mechanisms for various purposes.

REFERENCES

1. Hellier, C. (2001) *Handbook of nondestructive evaluation.* McGraw-Hill.

2. d*Destructive evaluation and quality control.* Vol. 17. ASM International.

3. Uchanin, V.M., Lutcenko, G.G., Opanasenko, A.V. (2023) Automated eddy current inspection systems with surface probe of double differential type. *The Paton Welding J.,* **5**, 48–56. DOI: https://doi.org/10.37434/tpwj2023.05.08

4. ASTM International (2017) *ASTM E2884−17 Guide for eddy current testing of electrically conducting materials using conformable sensor arrays.*

5. EN ISO 20339:2017: *Non-destructive testing — Equipment for eddy current examination — Array probe characteristics and verification* (ISO 20339:2017).

6. Lysenko, I., Kuts, Y., Uchanin, V. et al. (2023) Problems of using eddy current arrays NDT: Lecture Notes in Networks and Systems. Eds by Pawelczyk M., Bismor D., Ogonowski S., Kacprzyk J. *Advanced, Contemporary Control. (PCC 2023)*, **708**, 287–293. DOI: https://doi.org/10.1007/978-3-031-35170-9_27

7. Allard, A.M., Grenier, M., Sirois, M., Wassink, C. (2021) *Understanding eddy current array for high-performance inspections:* Materials Evaluation. DOI: https://doi.org/10.32548/2021.me-04226

8. Lamarre, A. (2015) *Eddy current array technology serves a variety of industries:* Quality Magazine. https://www.qualitymag.com/articles/92427-eddy-current-array-technology-serves-a-variety-of-industries

9. Kuts, Yu.V., Uchanin, V.M., Lysenko, Yu.Yu. et al. (2021) Application of Hilbert transform for analysis of signals of automated eddy current inspection. Pt 2. Deriving secondary diagnostic features and examples of realization. *Tekh. Diahnost. ta Neruiniv. Kontrol*, **4**, 11–18. DOI: https://doi.org/10.37434/tdnk2021.04.01

10. Deng, Y., Liu, X. (2011) Electromagnetic imaging methods for nondestructive evaluation applications. *Sensors*, 11(**12**), 11774–11808. DOI: https://doi.org/10.3390/s111211774

11. Mook, G., Michel, F., Simonin, J. (2011) Electromagnetic imaging using probe arrays. *J. of Mechanical Eng.*, 57(**3**), 227–236. DOI: https://doi.org/10.5545/sv-jme.2010.173

12. Lysenko, I., Kuts, Y., Uchanin, V. et al. (2024) Evaluation of eddy current array performance in detecting aircraft component defects. *Transact. on Aerospace Research*, **2**, 1–9. DOI: https://doi.org/10.2478/tar-2024-0007

13. Uchanin, V.M. (2023) Surface eddy current probes of double differential type as an effective tool to solve non-destructive inspection problems. *The Paton Welding J.*, **2**, 46–55. DOI: https://doi.org/10.37434/tpwj2023.02.07

14. Mook, G., Michel, F., Simonin, J. (2008) Electromagnetic imaging using probe arrays. In: *Proc. of 17th World Conf. on Nondestructive Testing, Shanghai.* www.ndt.net. DOI: https://doi.org/10.5545/sv-jme.2010.173

15. Sun, Z., Cai, D., Zou, Ch. et al. (2017) Design and optimization of a flexible arrayed eddy current sensor. *Measurement Sci. and Technology,* 28(**4**), 8. DOI: https://doi.org/10.1088/1361-6501/aa5b76

16. Ma, Q., Gao, B., Tian, G.Y. et al. (2020) High sensitivity flexible double square winding eddy current array for surface micro-defects inspection, *Sensors and Actuators A: Physical*, **309**, 111844. DOI: https://doi.org/10.1016/j.sna.2020.111844

ORCID

Iu.Yu. Lysenko: 0000-0001-9110-6684,
Yu.V. Kuts: 0000-0002-8493-9474,
Y. Mirchev: 0009-0002-4882-5282,
O.E. Levchenko: 0000-0002-3914-1818,
S.M. Glabets: 0009-0004-2740-9209

CONFLICT OF INTEREST

The Authors declare no conflict of interest

CORRESPONDING AUTHOR

Iu.Yu. Lysenko
National Technical University of Ukraine
"Igor Sikorsky Kyiv Polytechnic Institute"
E-mail: j.lysenko@kpi.ua

JOURNAL HOME PAGE

https://patonpublishinghouse.com/eng/journals/tpwj

DEVELOPMENT OF THE TECHNOLOGY OF PRODUCING A BIOCOMPATIBLE ALLOY BASED ON ZIRCONIUM–TITANIUM–NIOBIUM SYSTEM FOR MEDICAL IMPLANTS

O.V. Ovchynnykov[1], V.O. Berezos[2], V.S. Yefanov[3], D.S. Akhonin[2], D.I. Mozulenko[4]

[1]JSC "Institute of Titanium"
180 Sobornyy Prosp., 69035, Zaporizhzhia, Ukraine
[2]E.O. Paton Electric Welding Institute of the NASU
11 Kazymyr Malevych Str., 03150, Kyiv, Ukraine
[3]Ukrainian State University of Science and Technology
2 Lazaryan Str., 49010, Dnipro, Ukraine
[4]National University "Zaporizhzhia Polytechnic"
64 Zhukovski Str., 69063, Zaporizhzhia, Ukraine

ABSTRACT

The paper gives an overview of development and application of biocompatible alloys based on zirconium, titanium and niobium, featuring a low modulus of elasticity. The technology of producing a biocompatible 60Zr–20Ti–20Nb alloy and semi-finished products from it in the form of rods and powders for additive manufacturing was developed, and their structure and mechanical properties were studied. The potential for application of the developed biocompatible 60Zr–20Ti–20Nb alloy for manufacturing medical implants is shown.

KEYWORDS: zirconium, titanium, niobium, biocompatible alloys, electron beam melting, technological modes, chemical composition, structure, modulus of elasticity, mechanical properties

INTRODUCTION

Over the recent decades considerable attention was given to development and investigation of new materials for the medical industry, particularly in the field of implant creation. Modern implants require application of materials which are characterized not only by high biochemical compatibility and strength, but also special functional properties, such as shape memory, low modulus of elasticity, etc. [1–3]. One of the dominating criteria of application of metals for medical purposes is the criterion of survival of implants made from these materials in the human body.

At first a lot of attention was given to commercial titanium alloys of Ti–6Al–4V, Ti–6Al–7Nb type [4, 5], but the negative aspects appeared rather quickly. Titanium-based alloys have higher rigidity (Young's modulus, 110–120 GPa), which is three times higher than the value of bone rigidity (20–30 GPa) [6]. This difference leads to so-called voltage screening effect, causing bone resorption around the implant and leading to disintegration processes, i.e. creating a high degree of biomechanical incompatibility. More over, these alloys release toxic ions of vanadium and aluminium into the human body, leading to long-term processes of restoration of vital functions of the body.

In a separate set of polyfunctional biomedical materials a particularly important place is taken up by low-modulus titanium alloys, differing by a complex of extremely important characteristics: high ductility and strength, corrosion resistance and biocompatibility, owing to its biomechanical properties [7].

At present the achievements in the field of development of metallic biomaterials are focused on new variants of titanium-zirconium alloy, which are free of toxic elements, and have much lower modulus of normal elasticity (40–80 GPa). The low-modulus alloys based on zirconium-titanium compositions, while corresponding to biocompatibility criterion, also provide the technological capabilities at their manufacture by currently available methods, and ensure good prospects in the area of application of both the traditional technologies of manufacturing serial implants, and advanced additive technologies for individual implants [8].

Investigations of the equilibrium constitutional diagram of Ti–Zr system point to the rationality of development of alloys for medical purposes with zirconium content of 35–50 at.%. Minimal temperatures of melting and polymorphous transformation correspond to this range. It should be noted that martensite transformation is characteristic for Ti–Zr alloys at cooling, so that additional alloying, for instance by niobium, is used. Such alloying not only ensures a lowering of polymorphous

Table 1. Composition of zirconium master alloy (main alloying elements), wt.% (not more than)

Grade	N	O	C	Fe	S	Ni	Cl	Al	Ca	Mn	Ti	Cr
Iodide zirconium	0.005	0.05	0.008	0.03	0.008	0.02	–	0.005	0.02	0.001	0.005	0.02
KTTs-110	0.006	0.14	0.020	0.030	0.010	0.01	0.003	0.005	0.01	0.001	0.007	0.005

Table. 2. Composition of titanium sponge, wt.% (not more than)

Grade	N	O	C	Fe	Si	Ni	Cl
TG-90	0.02	0.04	0.02	0.05	0.01	0.04	0.08
TG-120	0.02	0.06	0.03	0.11	0.02	0.04	0.08

transformation temperature, but it also allows fixing by hardening the state with minimal values of the modulus of elasticity. Here, a high ductility is preserved.

Wide-spread application of low-modulus Ti–Zr alloys is limited by the complexity and multistage nature of the technological process of producing wrought semi-finished products in the technological schemes of manufacturing the implants — 6 mm diameter rods and 50–60 mm diameter electrodes for spraying the powders used in additive processes. A separate problem is producing ingots of Ti–Zr alloys with homogeneous chemical and phase composition of the metal in the product volume to provide a uniform distribution of deformation efforts inside the next semi-finished products and end products. Titanium, zirconium and niobium are chemically active elements, requiring methods of melting in vacuum. An essential difference between the metals in the density and melting temperatures, as well as technological difficulties in charge preparation, limits the possibilities for application of a number of vacuum melting methods. In keeping with analysis of works [9–11], the most rational technique is the method of electron beam melting (EBM). However, there is a range of unsolved issues as to the technological modes of melting, number of remelting cycles and determination of element transition coefficients.

OBJECTIVE

of this investigation was to produce a low-modulus zirconium β-alloy and to manufacture and study the characteristics of billets for implants from this alloy, which ensures the required level of mechanical and special properties determined by the medical purpose.

The alloy forms with application of chemically active elements, which requires special production conditions. In particular, it is necessary to conduct the melting process under vacuum and apply special techniques for averaging the chemical composition, stabilization of temperature and concentration parameters of alloy ingot formation. The above conditions of formation of the alloy and ingots from it are provided by cold-hearth electron beam melting.

Thus, this study is a complex analysis of the properties and application of 60Zr–20Ti–20Nb alloy, emphasizing its significance and good prospects for medical industry, particularly in the context of improvement of the quality and safety of medical implants.

INVESTIGATION MATERIALS AND METHODS

In order to develop 60Zr–20Ti–20Nb alloy with predicted properties, two different charges of the following composition were used: charge 1 — zirconium iodide, niobium and titanium sponge (TG-120); charge 2 — zirconium KTTs-110, niobium and titanium sponge (TG-90).

In order to lower the cost of charge materials, zirconium of KTTs-110 grade was used instead of zirconium iodide in charge composition 2 to produce experimental Zr–Ti–Nb alloy. Despite the fact that KTTs-110 zirconium has a higher concentration of oxygen, titanium sponge TG-90 was used in charge 2 for equalizing the amount of oxygen in the final alloy. Element composition of the raw material is given in Tables 1–3, and the material used — in Figure 1.

Alloying element content in the ingots was determined by the method of inductively-coupled plasma. Methods of optical emission spectrometry (ICP-OES) were applied using ICP-spectrometer ICAP 6500 DUO.

Samples for metallographic studies were polished using an abrasive disc (240–400–600 μm abrasive), with finish polishing on a felt circle with diamond emulsion (3 μm). Metallographic studies of macro- and microstructure of unetched and etched samples and analysis of fractograms of the cast and wrought alloy were performed in optical microscope NEO-PHOT-32 (Carl Zeiss Jena, Germany), as well as in scanning electron microscope JSM-IT300LV (Jeol,

Table 3. Composition of niobium master alloy, wt.% (not more than)

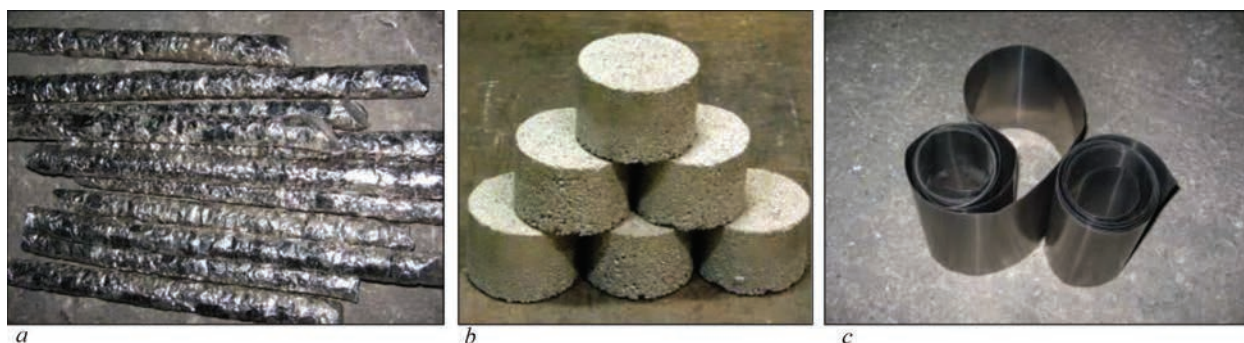| N	O	C	Fe	Si	Ta	Ti
0.05	0.04	0.06	0.08	0.03	0.3	0.07

Figure 1. Charging materials: *a* — iodide zirconium TU 95.46–82, rods; *b* — sponge titanium of TG-90 grade DSTU 3079–95, briquettes; *c* — niobium NBSh-1 GOST 16100–79, sheet

Japan) with the magnification of 500–5000. To perform analysis of macro- and microstructure, the samples were etched in a solution of hydrofluoric (20 %) and nitric (20 %) acids with a glycerin base. Three samples were used for each measurement method. Investigations of the ingot material microstructure were performed using optical microscope AxioObserver 5 at magnifications of 25–200. Etching of samples for metallographic studies was performed in "Titan" reactive of $HF:HNO_3:H_2O = 1:2:6$ composition.

Characteristics of distribution of the main alloying elements in the produced powders were assessed using scanning electron microscope Olympus DSX 1000 with DSX10-SXLOB1X lens and were analyzed using LEXT Olympus Analysis program. SEM images were obtained in scanning electron microscope Hitachi SU3900 under different conditions of vacuum and accelerating voltage of 15 kV. Energy dispersive spectroscopy (EDS) was conducted using Bruker detector and Esprit software.

Mechanical parameters of the developed alloy and end rod were studied using INSTRON 8801 system, (Instron, Norwood, Massachussets, USA). In order to determine the mechanical properties, the following parameters were assessed: tensile strength (σ_t, MPa), yield limit ($\sigma_{0.2}$, MPa), modulus of elasticity (E, DPa), relative elongation (δ, %) and reduction in area (ψ, %).

Measurements of Young's modulus of synthesized alloys were performed by nondestructive resonance method of pulsed excitation in RFDA Professional System 24 (Belgium). Mechanical vibrations in the studied samples of a flat shape were excited by a blow from the striker. Determination of Young's modulus was conducted by resonance frequency measurement, and the derived signal was calculated by fast Fourrier transform.

TECHNICAL REQUIREMENTS TO LOW-MODULUS ALLOY OF Zr–Ti–Nb ALLOYING SYSTEM AND PRODUCTS FROM IT

Modern technology of producing commercial billets for implants is a rather complicated technical assignment both as to achieving the required geometry, and as to mechanical properties of the billets.

Technological scheme of producing the billets consists of the following stages: charging, ingot melting, ingot machining, forging, rolling, drawing, heat treatment, centrifugal grinding. Producing billets from experimental Zr–Ti–Mn alloy requires development and determination of a specific scheme and modes of deformation and heat treatment:

● billet in the form of a 6 mm dia rod for the technological scheme of producing the implants;

● consumable products (50–60 mm diameter electrodes) for the technological scheme of producing powders by spraying method.

In keeping with the results of previous studies the following requirements to the billets from Zr–Nb–Ti alloy were formulated: chemical composition: Zr, at.% 51 ±2.0 (50 wt.%); Ti, at.% 31 ±1.5 (19 wt.%); Nb, at.% 18.0 ±1.5 (21 wt.%); mechanical properties: ultimate strength $\sigma_t > 700$ MPa; Young's modulus $E < 57$ GPa (considering that for the human bone E is equal to 30 GPa); requirements to billet geometry: diameter of 6 mm ±2 mm; length of 1500–3000 mm; surface roughness Ra 1.6–3.2; deviation from roundness should correspond to accuracy class h7; curvature should not exceed 0.5 % of the length.

Comparison of the obtained characteristics of experimental Zr–Nb–Ti alloy by the stretching diagram shows that elasticity modulus E is in the same range for the produced alloy samples, and it is equal to 27–29 GPa. Obtained values correspond to the claimed requirements to the implant metal. The level of mechanical properties, however, is lower than that for titanium alloy, namely for rod billet from VT6 alloy. The conclusion of the technological regulations for further treatment is that deformations, as well as modes of deformation and heat treatment, should provide simultaneous shaping of the implant billet (6 mm diameter rod) with improvement of the mechanical properties at uniaxial stretching to the level of VT6 alloy.

DEVELOPMENT OF THE TECHNOLOGY OF PRODUCING Zr–Ti–Nb ALLOY, INVESTIGATION OF THE ALLOY AND PRODUCTS FROM IT

Research work by the technology of producing low-modulus Zr–Ti–Nb alloy was performed with the purpose of optimization of the technological modes of producing ingots of an alloy based on Zr–Nb–Ti system by EBM method.

The technology of cold-hearth EBM is an effective method of producing sound ingots with the possibility of using a high proportion of wastes [12].

Cold-hearth application allows not only cleaning from impurities and inclusions of different density, but also producing an ingot of a homogeneous chemical composition and sound structure. More over, cold-hearth remelting allows alloying the liquid metal during melting, as well as processing the metal melt by different reagents.

At remelting, crystallization proceeds under the conditions of continuous coming of metal into the liquid pool, heating of the liquid pool surface, and ingot cooling. These factors ensure a favourable configuration of the liquid pool and high temperature gradient at crystallization, lowering the probability of initiation and development of macrostructure defects.

The essence of EBM process (Figure 2) consists in a horizontal feed of consumable billet *4* with the set rate into the melting zone, its melting by electron beams of guns *2*, *3* above cold hearth *5*. As the cold hearth is filled, the liquid metal is poured into mould *6*, where ingot *7* of the required length is formed.

Ingot melting was conducted in electron beam unit UE-208M into 110 mm diameter mould (Figure 3) [13].

Ingots were produced in the following sequence: calculation of the quantity of charge, allowing for metal evaporation; performing operations on initial material preparation and forming the consumable billet; preparation (cleaning of melting chamber and gun plate, cleaning the cold hearth and mould, tray cleaning, cleaning the electron gun beam guide from condensate, dust and remains of metal from previous melts) and setting up equipment (replacement of electron beam gun cathodes) and fixtures; performing melting in the specified modes; selection of samples
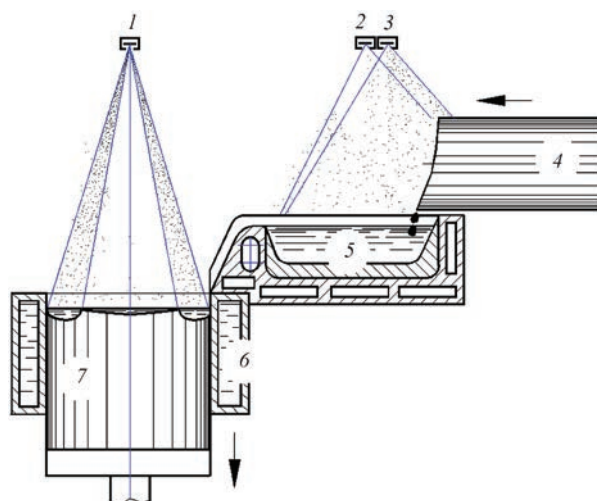
Figure 2. Scheme of cold-hearth EBM: *1–3* — electron beam guns; *4* — consumable billet; *5* — cold hearth; *6* — mould; *7* — ingot

for fast analysis of the produced ingot — chemical and gas analysis; selection of samples for mechanical testing of the produced ingot.

Calculated composition of the charge billet is given in Table 4.

During experimental melts the following technological parameters were monitored; melting rate and beam currents, accelerating voltage values. Numerical values of accelerating voltage and beam current were measured and adjusted, using instruments designed for it. Melting rate was adjusted by varying the speed of consumable billet feeding into the melting zone.

In order to determine the technological modes of conducting the EBM process to produce 60Zr–20Ti–20Nb alloy, a mathematical model was constructed of turbulent hydrodynamic and thermal processes in a cylindrical ingot of 110 mm diameter under the conditions of quasi-stationary mode of electron beam melting, which determines the dependence of the shape and depth of the metal pool in the mould on melting rate and power of electron beam heating of the melt surface.

Table 4. Composition of the charge for producing ingots of 60Zr–20Ti–20Nb alloy

Component	wt. %	kg
Zr	59	35.5
Nb	21	12.4
Ti	20	12.5
Total	100	60.4

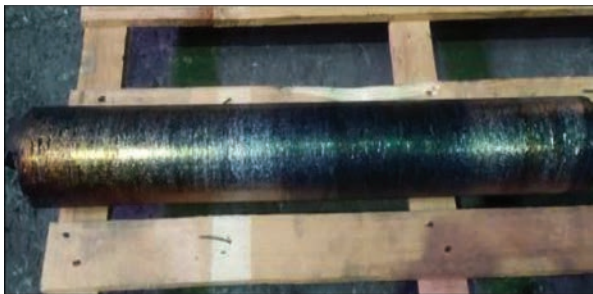**Figure 3.** Appearance of upgraded electron beam unit UE-208M

Figure 4. Ingot of 110 mm diameter of 60Zr–20Ti–20Nb alloy

It is known [9] that the flat and shallow shape of the metal pool at ingot production promotes formation of a fine homogeneous structure of the ingot metal and inhibition of the liquation processes at melt solidification. Analysis of the results of calculations by the plotted mathematical model allowed determination of the technological parameters of the stationary mode of electron beam melting which should ensure chemical homogeneity of the ingot and homogeneity of its structure, and they are the following:

Technological parameters of electron beam melting of a 110 mm ingot of 60Zr–20Ti–20Nb alloy

Total power of EB heating, kW 110
Power in the mould, kW 20
Melting rate, kg/h 20

After completion of melting, the produced ingots were cooled under the conditions of vacuum in the melting chamber. EMB ingot of 110 mm diameter from experimental alloy 60Zr–20Ti–20Nb is shown in Figure 4.

The quality of the ingot external surface is satisfactory, foundry corrugations are not more than 2 mm, and no cavities, cracks or pores are revealed.

Sample selection was performed from the ingot side surface by drilling to 5 mm depth without cutting fluid application during its machining (Figure 5).

The quality of the produced ingot metal was evaluated by the results of determination of its chemical composition (Table 5). Analysis of the derived results showed that deviations of zirconium content along the ingot length from its average value do not exceed 1.7 %; titanium — 0.8 %; niobium — 0.8 % that practically completely corresponds to the requirements of technical assignment.

Figure 5. Selection of samples from 110 mm dia ingot of 60Zr–20Ti–20Nb alloy

Figure 6. Appearance of machined 110 mm dia ingot of 60Zr–20Ti–20Nb alloy

For further operations, the ingot was treated by machining (Figure 6).

The quality of the metal internal volume was studied by the method of nondestructive ultrasonic testing (UT) using UD4-76 flaw detector. No shrinkage cav-

Table 5. Chemical composition of 110 dia ingot of 60Zr–20Ti–20Nb alloy, wt.%

Sample	Zr	Ti	Nb	O	Others
1	57.5	19.6	22.4	0.053	
2	58.7	18.3	22.4	–	
3	60.7	18.2	20.9	–	<0.6
4	58.9	19.7	20.8	–	
Average value	59.0	18.9	21.7	0.053	<0.6

Figure 7. Appearance of 59 mm dia forgings of 60Zr–20Ti–20Nb alloy

ities, pores and other inhomogeneities were found in the ingot metal.

Work results suggest the possibility of producing by EBM sound ingots of low-modulus alloys of 60Zr–20Ti–20Nb type, designed for application as bioinert alloys for medical purposes.

DEFORMATIONAL AND HEAT TREATMENT AND SHAPING A BILLET WITH HIGHER MECHANICAL PROPERTIES

Deformational processing was performed using thermal preparation in an automatic forging complex AKP-500 with 5 MN hydraulic press, manipulator and two heating furnaces with precise temperature control. Three-stage heating mode was performed: 700 °C for 2.5 h, then 900 °C for 1 h with subsequent transfer to the force forging at the temperature of 1000 °C for 1 h.

Forging was performed by "circle-square" scheme in the following modes: transition from 106 mm diameter to 91 mm square; transition from 91 mm square to 75 mm square; transition from 75 mm square to 60 mm square; transition from 60 mm square to
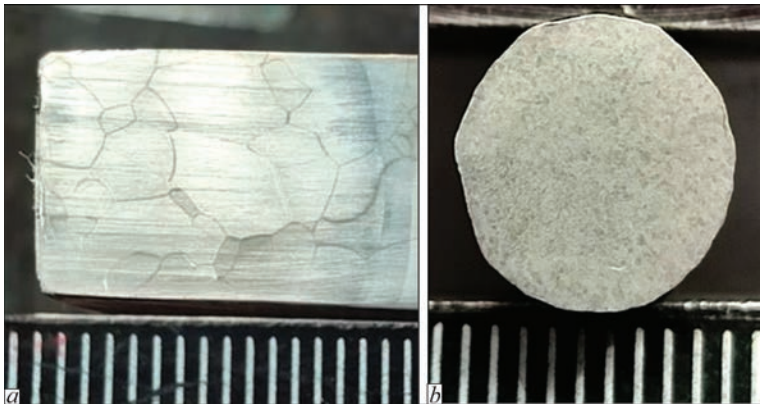

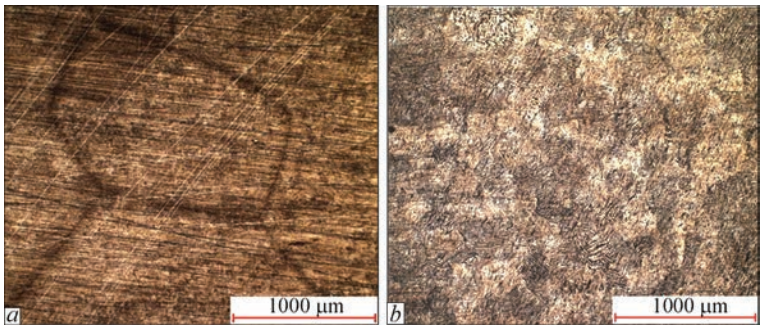**Figure 8.** Macrostructure of 110 mm dia ingot after EBM (*a*) and of 6 mm rods from 60Zr–20Ti–20Nb alloy (*b*)

Figure 9. Microstructure of 110 mm dia ingots (*a*) and final 6 mm rod billets (*b*)

Table 6. Comparative characteristic of 6 mm dia rod billet of 60Zr–20Ti–20Nb alloy and VT6 titanium alloy for dental implants

Alloy	Mechanical properties				
	σ_t, MPa	$\sigma_{0.2}$, MPa	E, GPa	δ, %	ψ, %
60Zr–20Ti–20Nb	850÷900	670÷700	28–30[*] 59–66[**]	12	40–58
VT6	830÷1254	–	115[*] 102–104[**]	10	44
Grade 5 ELI	860	795	–	10	25

[*]Values of the modulus of elasticity were determined by calculations from stretching diagram of samples for mechanical testing.
[**]Values of the modulus of elasticity were determined by the method of pulsed excitation in RFDA Professional System 24.
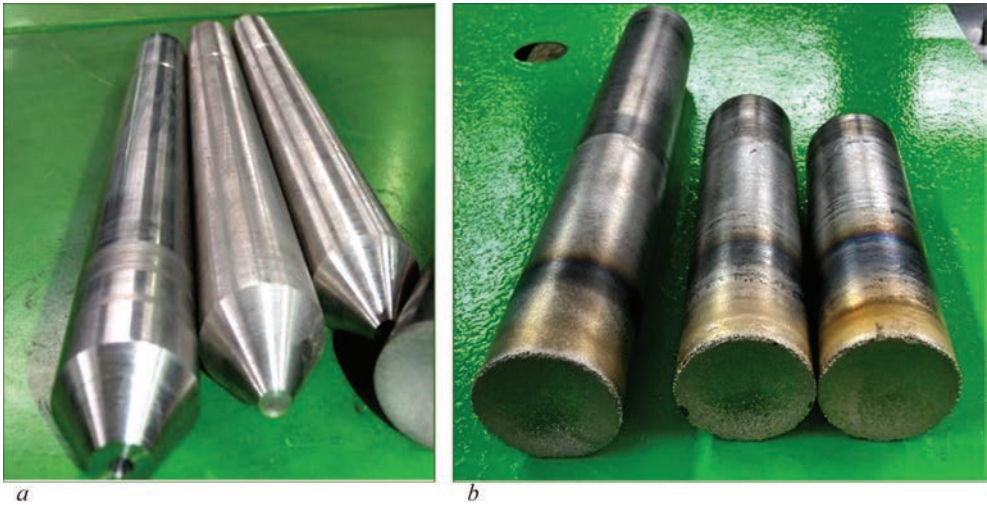

Figure 10. Electrodes of 50 mm dia from 60Zr–20Ti–20Nb alloy to produce spherical powders before spraying (*a*) and after spraying (*b*)

59 mm diameter; metal heating in the forging furnace after each pass, and cooling of the forging in air.

Produced forgings are shown in Figure 7.

Rod forging was followed by rolling and drawing to 6 mm diameter. As a result, the rod billets have the fol-

Figure 11. UTsR-4 unit for centrifugal spraying

lowing geometrical characteristics: 6 mm diameter; up to 3150 mm length; h7 class of accuracy; surface roughness of Ra0.8. Macrostructure of 6 mm diameter rods of 60Zr–20Ti–20Nb alloy is shown in Figure 8.

Macrostructure analysis showed that β-primary grains of the ingots of equiaxed type with a coarse fringe of up to 5 μm size (Figure 8, *a*) were refined to fine-grained macrostructure in the rods (Figure 8, *b*).

Results of studying the microstructure revealed that the microstructure was refined to 50–60 μm size (Figure 9).

Microstructural analysis showed that it changes from cast coarse-grained structure of 150–200 μm primary grains to deformed fine equiaxed structure with platelike submicrostructure.

Mechanical properties of the produced rod of 6 mm diameter of 60Zr–20Ti–20Nb alloy in comparison with titanium alloy VT6/Grade 5 are given in Table 6.

One can see from the comparative data that the rod billet from an alloy based on Zr–Ti–Nb system has minimal value of the modulus of elasticity (27.6 GPa), which is 3 times lower than that of VT6 alloy (115 GPa) and it is close to the value of modulus of elasticity of the human bone (30 GPa). It gives grounds to talk about improvement of biocompatibil-
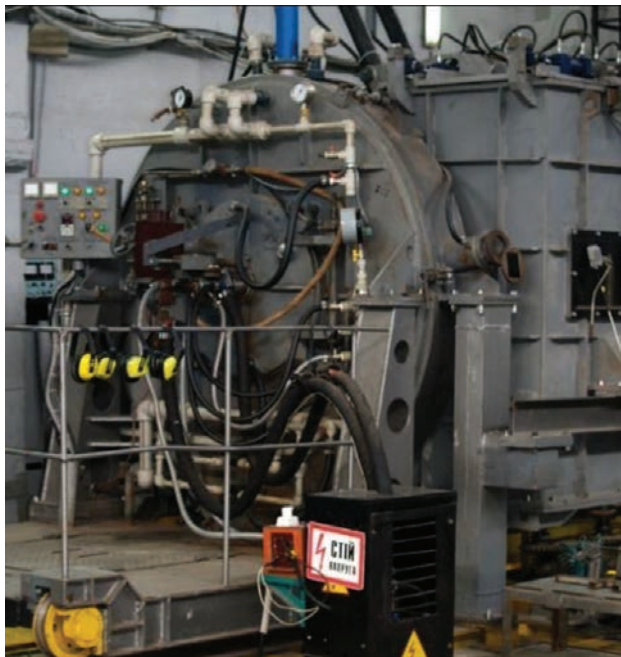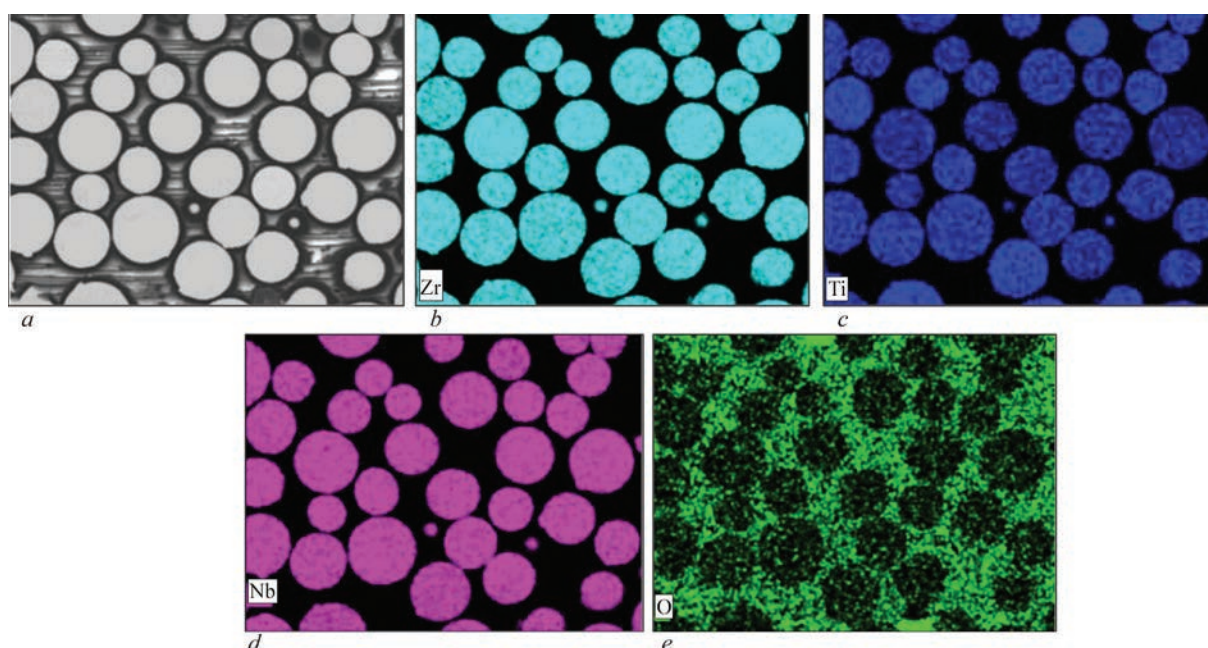
Figure 12. Electronic photo of 60Zr–20Ti–20Nb powder (*a*) and maps of distribution of zirconium (*a*), titanium (*b*), niobium (*c*) and oxygen (*e*) over analysis zone

Table 7. Fractional composition of produced metal powders from Zr–Ti–Nb alloy

Fraction	Bulk density, g/cm³	Weight, g
+200	4.2	900
+180	4.19	128
−140+125	4.00	2654
−90+56	3.97	1589
−56+40	–	95
−40 tray	3.96	261

ity. At the same time, load resistance corresponds to that of analogous VT6 alloy that confirms the level of mechanical properties of the zirconium alloys.

PRODUCING POWDERS OF Zr–Ti–Nb ALLOY

Forgings of 59 mm diameter from 60Zr–20Ti–20Nb alloy were used to produce by machining a test batch of electrodes of 50 mm diameter for manufacturing spherical powders by the method of centrifugal plasma spraying [14] (Figure 10).

Appearance of UTsR-4 unit for centrifugal spraying is shown in Figure 11.

Produced metal powders of 60Zr–20Ti–20Nb alloy were sifted on vibration sieves into different fractions.

An example of fractional composition of the produced metal powders of Zr–Ti–Nb alloy is given in Table 7.

The main criterion of powder quality is the chemical composition of the powders, alongside the shape and fractional composition. Analysis of investigation results led to the conclusion that the microstructure (Figure 12, *a*) is homogeneous, without inclusions,

pores or structure inhomogeneities. Results of analysis of chemical composition of the main elements and oxygen impurities showed that they are uniformly distributed (Figure 12, *b–e*). No concentrational heterogeneities of the elements were found.

Thus, the scientific and engineering solutions on melting ingots of 60Zr–20Ti–20Nb alloy allowed producing rods and spherical powders, meeting all the technological and service requirements of TU U24.4-43658421-002:2021 "Powder from an alloy based on zirconium–titanium–niobium system".

CONCLUSIONS

1. Given results of research work indicate the possibility of producing by EBM the ingots of low-modulus alloys based on zirconium of 60Zr–20Ti–20Nb type designed for application as bioinert alloys for medical purposes.

2. A technology was developed to produce Zr–Ti–Nb alloy by electron beam melting, with satisfactory distribution of alloying components and homogeneous defectfree structure.

3. A scheme of deformational processing of the billet is proposed which allowed producing the required geometry of a rod of 6 mm diameter, 3150 mm length, with deviation from roundness in keeping with h7 accuracy class and surface roughness of Ra 0.8. As a result of conducting testing on samples from a rod billet, evaluation of mechanical properties of experimental 60Zr–20Ti–20Nb alloy was obtained: ultimate strength of 850–900 MPa, elongation of 12 %.

4. Obtained evaluations showed that the rod billet from experimental β-Zr alloy of 60Zr–20Ti–20Nb

composition has the modulus of elasticity $E = 28$–30 GPa (calculated from stretching diagrams of samples for mechanical testing) and modulus of elasticity $E = 59$–66 GPa (determined by the method of pulsed excitation in RFDA Professional System 24) that is much lower than in VT6 alloy ($E = 102$–115 GPa) and is closer to the value of modulus of elasticity of the human bone ($E = 30$ GPa).

5. Presented results are indicative of practical possibilities of producing consumable materials for implants (6 mm diameter rods) and spherical powders for additive technologies of manufacturing high-precision implants, where the microstructure is uniform without inclusions, pores or structural inhomogeneities, corresponding to all technological and service requirements. Results of the conducted studies were used to prepare technical conditions TU U24.4-43658421-002:2021 "Powders from an alloy of zirconium–titanium–niobium" system.

REFERENCES

1. Liu, Xuanyong, Chu, Paul K., Ding, Chuanxian (2004) Surface modification of titanium, titanium alloys, and related materials for biomedical application. *Materials Sci. and Eng.: R: Reports*, 47(**3**), 49–121. DOI: https://doi.org/10.1016/j.mser.2004.11.001

2. Elias, C.N., Lima, J.H.C., Valiev, R., Meyers, M.A. (2008) Biomedical applications of titanium and its alloys. *JOM*, 60(**3**), 46–49. DOI: https://doi.org/10.1007/s11837-008-0031-1. S2CID 12056136

3. Niinomi, M. (2000) Development of high biocompatible titanium alloys. *Func. Mater.*, **20**, 36–44.

4. Fellah, Mamoun, Labaiz, Mohamed, Assala, Omar et al. (2014) Tribological behavior of Ti–6Al–4V and Ti–6Al–7Nb alloys for total hip prosthesis. *Advances in Tribology*, 451387. DOI: https://doi.org/10.1155/2014/451387

5. Lopez, M.F., Gutierrez, A., Jimenez, J.A. (2002) In vitro corrosion behaviour of titanium alloys without vanadium. *Electrochimica Acta*, 47(**9**), 1359–1364. DOI: https://doi.org/10.1016/S0013-4686(01)00860-X

6. Ivasyshyn, O.M., Skyba, I.O., Karasevska, O.P., Markovskyi, P.E. (2013) *Biocompatible alloy with low modulus of elasticity based on zirconium-titanium system (variants).* Ukraine, Pat. 102455 [in Ukrainian].

7. Niinomi, M. (2008) Mechanical biocompatibilities of titanium for biomedical applications. *J. of the Mechanical Behavior of Biomedical Materials*, **l**, 30–42. DOI: https://doi.org/10.1016/j.mbbm.2007.07.001

8. Mishchenko, O., Ovchynnykov, O., Kapustian, O., Pogorielov, M. (2020) New Zr–Ti–Nb alloy for medical application: Development, chemical and mechanical properties, and biocompatibility. *Materials*, 13(**6**), 1306. DOI: https://doi.org/10.3390/ma13061306

9. Berezos, V.O., Akhonin, D.S. (2023) Electron beam melting of titanium alloys for medical purposes. *Suchasna Elektrometal.* **2**, 5–13 [in Ukrainian]. DOI: https://doi.org/10.37434/sem2023.02.01

10. Ladokhin, S.V., Levitsky, M.I., Chernyavsky, V.B. et al. (2007) *Electron beam melting in foundry.* Kyiv, Stal [in Russian].

11. Grechanyuk, N.I., Kulak, L.D., Kuzmenko, N.N. et al. (2017) Melting of ingots of Ti–Nb–Si–Zr system titanium alloys by the method of electron beam melting. *Suchasna Elektrometal.*, **2**, 17–20 [in Russian]. DOI: https://doi.org/10.15407/sem2017.02.03

12. Akhonin, S., Pikulin, O., Berezos, V. et al. (2022) Determining the structure and properties of heat-resistant titanium alloys VT3-1 and VT9 obtained by electron-beam melting. *Eastern-European J. of Enterprise Technologies*, 5(**12**(119), 6–12. DOI: https://doi.org/10.15587/1729-4061.2022.265014

13. Akhonin, S.V., Pikulin, A.N., Berezos, V.A. et al. (2019) Laboratory electron beam unit UE-208M. *Suchasna Elektrometal.*, **3**, 15−22 [in Russian]. DOI: http://dx.doi.org/10.15407/sem2019.03.03

14. Ovchynnykov, O.V., Khaznaferov, M.V. (2022) *Introduction to additive technologies of nonferrous metals.* Kyiv, Naukova Dumka [in Ukrainian].

15. https://powdermet.com.ua/

ORCID

O.V. Ovchynnykov: 0000-0002-5649-1094,
V.O. Berezos: 0000-0002-5026-7366,
V.S. Yefanov: 0000-0002-6363-4081,
D.S. Akhonin: 0009-0000-2054-4054,
D.I. Mozulenko: 0000-0002-0428-9265

CONFLICT OF INTEREST

The Authors declare no conflict of interest

CORRESPONDING AUTHOR

V.O. Berezos
E.O. Paton Electric Welding Institute of the NASU
11 Kazymyr Malevych Str., 03150, Kyiv, Ukraine.
E-mail: titan.paton@gmail.com

JOURNAL HOME PAGE

https://patonpublishinghouse.com/eng/journals/tpwj

FABTECH 2024 EXHIBITION

ARC SPECIALTIES AND ASM INTERNATIONAL

At the invitation of Dan Allford, President of Arc Specialties, Houston, USA, as part of long-term co-operation with the E.O. Paton Electric Welding Institute (PWI), a business visit to the USA was held in October 2024 of Dr. Volodymyr Kachynskyi, a senior scientist at the PWI. The program of the visit included presentations of the latest results of the PWI work on scientific achievements in the development of advanced technologies of welding and related processes such as flash butt welding, electron beam welding and additive technologies, narrow gap welding, manual laser welding, explosion technologies, underwater welding and cutting, electron beam welding in space, high frequency live tissue welding, microplasma spraying, plasma-inductive process of single crystals tungsten growing, method for determination of residual stresses in welded joints, magnetically impelled arc butt welding (MIAB) also their industrial application for the purpose of economic growth. During the visit, presentations were held by Arc Specialties.

Presentation at Arc Specialties with live demo MIAB welding

Arc Specialties is the leading supplier of choice for automated manufacturing systems with over 40 years of experience in 33 countries around the world: from different arc welding technologies, 3D cladding, hardfacing and plasma cutting to material handling, precision positioning equipment and assembly hard automation. And the American Society Metals (ASM International) with the support of Jean-Marc Tetevuide, business development specialist at Har-Bach Fusion Technology Company, for representatives of scientific organizations and industrial companies in the USA. ASM International is an association for attracting specialists in the field of materials science and their organizations to the resources necessary to solve scientific and technical problems in order to achieve the required results. The total number of people present was approximately 120 individuals.

Presentation of PWI developments for ASM International, Houston, USA

AMERICAN WELDING SOCIETY

On October 14, the PWI was presented at the American Welding Society (AWS) Annual Business Meeting. During the AWS work, several meetings were held, including with the AWS President in

Meeting with the
Mr. Ernest Levert Sr.,
President of the AWS in 2003

Meeting with Ms. Nancy C. Cole,
President of the AWS in 2013

Meeting with Richard Holdren, coming AWS President in 2025, Dan Allford,
President of Arc Specialties and Dr. Volodymyr Kachynskyi, PWI

2003, Mr. Ernest Levert Sr., the AWS President in 2013, Ms. Nancy C. Cole, and the coming AWS President in 2025, Mr. Richard Holdren.
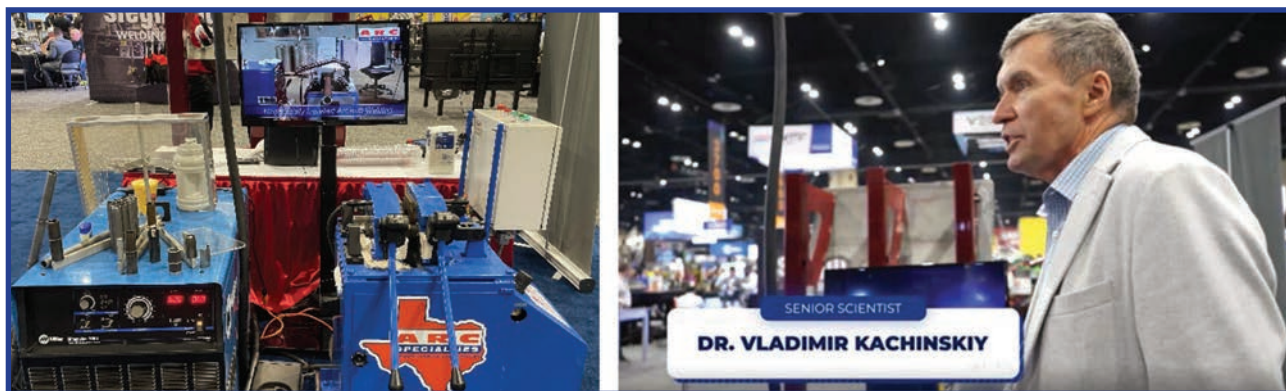
FABTECH 2024

Additionally, from October 15 to 17, the AWS development, a MIAB welding machine, was presented at the FABTECH 2024 exhibition in Orlando with a demonstration of the welding process. The PWI developed MIAB welding process was included in the 60 coolest technology demonstrations in one video presented at FABTECH, according to the renowned expert Jake Hall, The Manufacturing Millennial. FABTECH Expo is North America's largest metal forming, fabrication, welding, and finishing event.

At the 2024 FABTECH exhibition, over 1,500 companies showcased their products and services to 35,000 exhibitors across 750,000 square feet of exhibit space. Despite the inclement weather caused by Hurricane Irma that impacted Orlando, Florida the week prior, FABTECH was a resounding success. The event attracted a substantial number of exhibitors and attendees, who expressed their optimism about the future of manufacturing globally and in the United States. A notable highlight of this year's FABTECH was the demonstration of collaborative robots (cobots). While arc welding is not traditionally associated with cobot, the collaborative nature of a cobot, coupled with its ability to sense human contact and deactivate before causing harm, enhances the safety of welding operations. Repetitive, routine, and ergonomically challenging tasks can be tedious and hazardous for workers in virtually any manufacturing environment. Cobots can significantly increase productivity levels by automating virtually any manual task, including small batches or quick changeovers. Ad-

FABTECH 2024

ditionally, cobots can reuse programs to perform repetitive tasks. In the coming years, cobots are expected to witness increased adoption, particularly in welding and cutting applications. This trend is accompanied by a decline in the number of manufacturers, as the current market is overcrowded with new entrants, many of which may not survive beyond a few years. Another area of innovation introduced at FABTECH was 3D printing, or additive manufacturing (AM). While AM is often perceived as a novel technology, welding is one of its pioneering additive technologies. AM is rapidly transitioning from a novelty

**The MIAB welding machine was presented at the FABTECH 2024
with a demonstration of the live welding process by Dr. Volodymyr Kachynskyi**

to a viable manufacturing method. Much of the work involves the use of gas metal arc welding using small wires, a process known as wire-arc additive manufacturing.

While significant research continues in developing codes and specifications for this new technology, as well as measuring material properties in printed parts, there is scope for innovation in the use of other welding processes with higher deposition rates than traditional GMAW. High-performance AM candidates include electroslag and submerged arc welding. There has been a significant emphasis on automating not only the welding processes, but also the automation of part preparation, machining, cleaning, post-weld inspection, and post-weld finishing. Future manufacturing cells will incorporate more processes in a smaller footprint. There is also a noticeable trend away from traditional capital-intensive procurement of large systems toward more accessible, low-cost models. The first model is robots as a service, where the supplier retains ownership and simply provides the equipment for a fee for a limited time. This allows manufacturers to take advantage of robotics without making significant capital investments. This also justifies the use of robots for shorter production runs.

The second model is leased robots. In this model, the manufacturer retains ownership as well as responsibility for monitoring, software updates, and maintenance. It also eliminates the risk of large capital expenditures. It is likely that both of these models will become more common in the industry. At the ARC Specialties booth, we proudly demonstrated several innovative technologies. The first was the concept of deploying traditional robots in hazardous environments, such as drilling ships in the Gulf of Mexico, to replace humans in physically demanding and dangerous tasks. By making robots mobile, numerous opportunities are opened up for working on stationary or excessively large parts that would be economically impractical to move manually. The second was a robot capable of both welding and cutting in the field on a moving magnetic base. This application utilized a collaborative robot, which improved safety and reduced the size of the robot to allow for mobility in tight spaces and single-handed operation.

Our third exhibit showcased MIAB a technology developed by the PWI. We were fortunate to have Dr. Volodymyr Kachynskyi who contributed to its development, present and demonstrate this unique technology. MIAB is relatively unknown in the United States, and visitors were amazed by its ability to weld small diameter pipes in under four seconds, which would typically take hours using traditional methods. Overall, the exhibit highlighted the rapid pace of technological advances. Computers, sensors, and robots are becoming faster, more efficient, and more accessible, allowing us to solve previously impossible problems. Automating quality control allows for greater measurement consistency and maintaining high levels of product quality. The cobot arm's repeatability of +/–0.03 mm (30 microns) is ideal for automating high-precision operations in quality control and testing. However, it is equally important to maintain a clear understanding of welding processes, parameters, and procedures to ensure success. Despite the challenges caused by the COVID-19 pandemic, trade shows remain indispensable platforms for connecting technology providers with end users. As such, we expect trade shows to continue to play a key role in the future of the industry.

**Volodymyr Kachynskyi, PWI, Ukraine,
Dan Allford, President of Arc Specialties, USA**

SAZ s.r.o. — RELIABLE MACHINERY FOR THE RAILWAYS

SaZ s.r.o. is a Czech mechanical Engineering Company, which since 1954 has specialized in the design, production and repair of special road and railway machinery, road-rail vehicles (double-track machines), in particular rail machines with telescopic lifting platforms, insulated platforms for working with contact wires and rail layers, machines for flash-butt welding of rails, railway track layers and other equipment designed for servicing the railway and tram tracks.

SaZ s.r.o. production range includes railway platforms and transporters, railway boogies, body superstructures, access ramps, etc.

SaZ s.r.o. main clients are large construction companies, municipal transport companies, fire and road transport services, as well as small companies, involved in maintenance and repair of railway and tram tracks.

Since 2011 **SaZ s.r.o.** has also concentrated on engineering, namely: highway construction, road construction, railway construction, real estate construction and other construction work.

Over these years **SaZ s.r.o.** Company has grown and has become one of the main suppliers not only in Czechia and Slovakia, but also in many other countries, for instance in Denmark, Italy, Hungary, Poland, Germany, France, Spain, Austria, Bulgaria, Latvia, Lithuania, India, Australia, Azerbaijan, Ukraine, Ghana, Israel, and oth.

Continuous investments into research and development allow **SaZ s.r.o.** Company proposing innovative and high-quality products, which meet the highest technical standards and clients' requirements. Our modern production facilities and a team of qualified experts ensure that each product leaving our shops is a guarantee of reliability and productivity.

SaZ s.r.o. double-track machinery performs the tasks of renovation and construction of the tracks, cleaning the railway track from sand, dirt, snow, maintenance and upgrading of power transmission lines. The Company product line also includes special double-track fire trucks

Double-track machine DUOLINER MIJ is designed primarily for conducting expert operations on bridge structures, diagnostics and detailed inspection of both road and railway bridges

Double-track machine R DUOTRAM H is designed for movement and working on the motor roads, railway and tram tracks, predominantly for maintenance of contact lines

Double-track machine IT DUOLINER is fitted with a working platform with scissors for railway maintenance, hydraulic valve and measuring pantograph

Company Certification. In addition to certificates of quality control system ISO 9001:2015, certificates of the environmental management system ISO 14001:2015 and certificate of conformity of production management EN ISO 3834-2:2005, **SaZ s.r.o.** also has other certificates that demonstrate a high standard of quality.

UKRAINIAN-CZECH COOPERATION

Seventy-year experience of **SaZ s.r.o.** successful operation has found its implementation in solving the ever-present problem — creation of efficient equipment for welding the railway rails. In 2023 **SaZ s.r.o.** Company in close cooperation with the E.O. Paton Electric Welding Institute (PWI) of the NAS of Ukraine successfully set up production of double-track
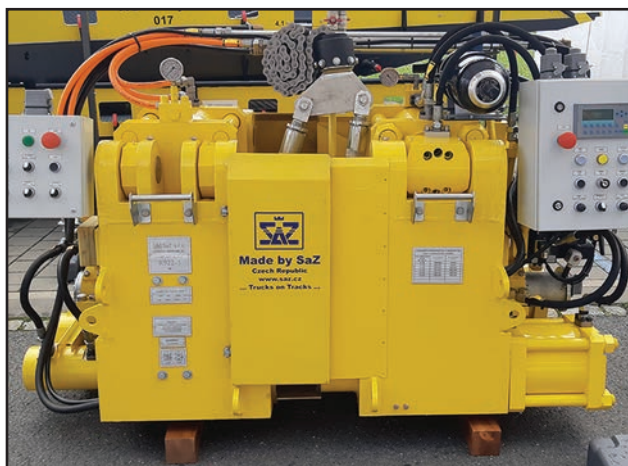
rail-welding complexes **WELDERLINER**, fitted with K922-1 mobile machines for flash-butt welding (FBW).

SaZ s.r.o., which previously did not specialize in welding equipment, mastered production of K922-1 machines for FBW in a very short time frame, ensuring an extremely high production quality.

Mobile (suspended) K922-1 machine is an original development of the PWI and it implements the innovative technology of pulsed flash-butt welding. K922-1 machines are fitted with a modern computerized system of multifactor monitoring of welding parameters, high-speed hydraulic drives, as well as a cutting device, which removes the hot flash without unclamping the welded rail section. The welded butt joint can be held during the time required for cooling of the joint to the specified temperature. K922-1 machines have been successfully used, as part of mobile rail-welding complexes, for dozens of years in many countries of the world on all the continents, both for construction and repair work on rails of any types and dimensions.

Double-track **WELDERLINER** complexes, fitted with K922-1 machines, meet all the requirements of the international safety standards for the quality of welded butt joints of rails, and the requirements on EU environmental indicators.

SaZ s.r.o. Company has successfully fulfilled the contracts for supplying several rail-welding **WELDERLINER** complexes to customers in the EU countries. **WELDERLINER** complexes have successfully passed comprehensive testing specified by the European standard EN 14587-2:2009.

For Ukraine, as a country with an extremely extensive network of railways, introduction of **WELDERLINER** complexes, fitted with modern mobile K922-1 machines, is highly relevant. **SaZ s.r.o.** Company provides maintenance of **WELDERLINER** complexes, service, training of the operators and engineering personnel. All the testing and adjustment operations in the rail-welding complexes of **SaZ s.r.o**. Company are conducted with the participation of PWI specialists.

WELDING WIRE FROM "DNIPROMETYZ TAS"
YEAR-END RESULTS AND INNOVATIONS FOR THE FUTURE

The year 2024 has been a period of significant achievements for "DNIPROMETYZ TAS" in welding material production. By focusing on quality, innovation, and expanding its product range, the Company has strengthened its position in domestic and international markets. The factory's products, including G3Si1 and G4Si1 grades, have gained customer trust in various economic sectors, from construction to mechanical engineering.

Since the launch of cutting-edge production lines for welding wire by the Swedish manufacturer Lämneå Bruk AB, the welding wire manufacturing and sales division has achieved a leading position among Ukrainian producers, even amid wartime challenges, reaching over 1,500 tons per year.

PRODUCT RANGE EXPANSION

In response to the demands of modern industries, "DNIPROMETYZ TAS" offers a wide selection of welding wire:

● Copper-coated wire G4Si1 and G3Si1, with diameters from 0.8 to 2.0 mm, available on spools weighing 15, 5, 2.5, and 1 kg. Precision winding ensures stable wire feeding during welding;

● Polished wire without coating, available in diameters of 0.8, 1.0, 1.2, and 1.6 mm on 15 and 18 kg spools;

● Wire for robotic systems in 250 kg drums, optimizing production processes at large enterprises.

EXPANDING INTERNATIONAL INFLUENCE

A key achievement this year was accreditation by Deutsche Bahn. As one of the largest transportation operators in Europe and globally, Deutsche Bahn plays a vital role in mobility and significantly influences the transportation sector. This accreditation confirms the factory's products meet the highest European Union quality standards.

Additionally, the welding wire successfully passed testing at the E.O. Paton Electric Welding Institute, paving the way for applications in steel bridge construction.

The factory also actively showcased its solutions at leading international exhibitions, such as *Wire 2024* in Düsseldorf, the XXII International Industrial Forum in Kyiv, *WeldTech 2024* in Warsaw, and *InnoTrans 2024* in Berlin. These events demonstrated international interest in welding materials from Ukrainian producers, facilitating new partnerships, knowledge exchange with other manufacturers, and valuable feedback for product improvement. "DNIPROMETYZ TAS" continues to strengthen its position in foreign markets, presenting its products to clients worldwide and proudly upholding the "MADE IN UKRAINE" mark on the global stage.
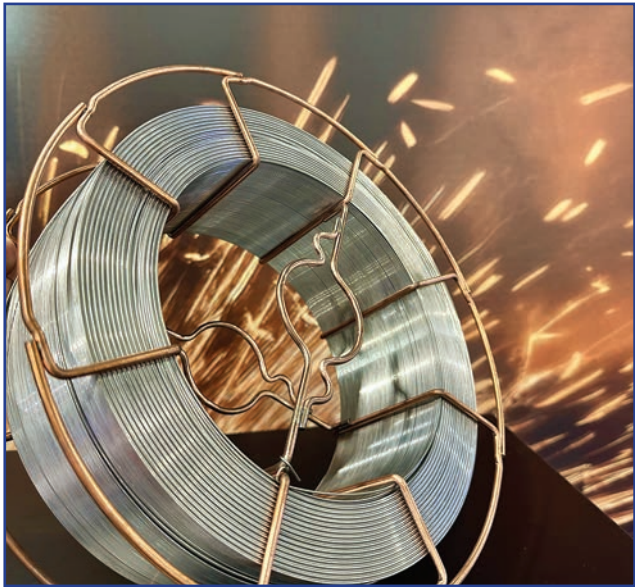
EMERGING INDUSTRY TRENDS

The global welding materials market shows steady growth, driven by industrialization, urbanization, and increased automation. Welding process automation significantly boosts productivity, improves weld quality, and reduces the risk of injuries.

"DNIPROMETYZ TAS" actively invests in developing robotic solutions, offering welding wire in convenient packaging for automated production lines. In 2024, the Company also implemented new approaches to customer training and support. Its welding production technologists provide consultations, technical assistance, and support at every stage of product usage.

PROVEN QUALITY

Welding wire from "DNIPROMETYZ TAS" complies with international standards, including ISO 9001, TÜV NORD certification, and DB accreditation. These certifications guarantee excellent quality, high-strength welds, corrosion resistance, and durability. The CE marking confirms compliance with safety requirements in the European Union.

LOGISTICS AND CUSTOMER FOCUS

Efficient logistics are one of the factory's strengths. With its fleet of vehicles, the Company ensures fast product delivery across Ukraine and abroad, reducing lead times and increasing customer satisfaction.

LOOKING TO THE FUTURE

"DNIPROMETYZ TAS" continues to invest in advanced technologies and improve its products. The Company is confident that its innovative solutions will help clients adapt to new challenges, ensuring quality and reliability in any conditions.

MARKET PROSPECTS FOR WELDING MATERIAL

The global welding materials market is experiencing consistent growth and is expected to expand significantly in the coming years. Analysts predict that by 2030, the market will grow due to its extensive use in constructing metal structures in various sectors, such as construction, bridge building, pipeline installation, and other engineering projects. The wide application of welding materials in the transportation industry, shipbuilding, and energy sectors will also drive demand.

Innovative technologies, such as laser and robotic welding, are gradually transforming the industry. Automation enhances welding quality and reduces costs. "DNIPROMETYZ TAS" actively adopts these trends, offering products that meet modern standards.

A key growth factor for the market is the demand for environmentally friendly and highly efficient welding materials. This trend creates new opportunities for Ukrainian manufacturers like "DNIPROMETYZ TAS," focusing on sustainable technologies and compliance with international standards.